VAASAN YLIOPISTO

PETRI VÄLISUO

Photonics Simulation and Modelling of Skin for Design of Spectrocutometer

ACTA WASAENSIA NO 242

AUTOMATION TECHNOLOGY 2

UNIVERSITAS WASAENSIS 2011

Reviewers

Professor Juha Röning
University of Oulu
Department of Electrical and Information Engineering
P.O. Box 4500
FI–90014 University of Oulu
Finland

Professsor Paul Geladi
Swedish University of Agricultural Sciences
Linnaeus väg 6
SE–901 83 Umeå
Sweden

Julkaisija	**Julkaisupäivämäärä**	
Vaasan yliopisto	Toukokuu 2011	
Tekijä(t)	**Julkaisun tyyppi**	
Petri Välisuo	Artikkelikokoelma	
	Julkaisusarjan nimi, osan numero	
	Acta Wasaensia, 242	
Yhteystiedot	**ISBN**	
Vaasan yliopisto	978-952-476-347-9 (nid.)	
Teknillinen tiedekunta	978-952-476-348-6 (pdf)	
Sähkö- ja energiatekniikan yksikkö	**ISSN**	
PL 700	0355–2667, 1798–789X	
65101 Vaasa	**Sivumäärä**	**Kieli**
	156	Englanti

Julkaisun nimike
Ihon fotoniikkamallinnus ja simulointi Spektrokutometrin suunnittelussa

Tiivistelmä

Optiset menetelmät sopivat hyvin lääketieteessä tarvittavien mittausten tekemiseen, sillä kosketuksetta toimiva optinen mittaustapa aiheuttaa vain hyvin pientä haittaa tai riskiä potilaalle. Ihon rakenne ja sen väriaineiden absorptiospektrit suosivat mittauksien tekemistä näkyvällä ja lähi-infrapuna-alueen aallonpituuksilla.

Nykyään lääketieteellisten hoitojen tulee olla näyttöperusteisia. Kuitenkin ihomuutosten hoitamisen perusteena oleva tieto on pääsääntöisesti hankittu subjektiivisin menetelmin, jotka ovat hankalasti toistettavia, henkilöstä riippuvaisia ja hankalasti dokumentoitavia.

Väitöskirjassa tutkitaan ihon väriaineiden konsentraation jakautumisen ennustamista diffuusioteoriaan ja muunneltuun differentiaaliseen Beer-Lambertin kaavaan perustuvalla ihomallilla, ja rakentamalla prototyyppi, Spektrokutometri, ihon pinnanalaisen hajaheijastusspektrin kuvantamiseksi vakio-olosuhteissa. Tutkimuksessa kehitettiin nopea kartoitusmenetelmä ihon väriaineiden pitoisuuksien laskemiseen suuren spatiaalisen tarkkuuden monikanavaspektrikuvasta. Kehitettyä mallia testattiin vertaamalla sitä Monte Carlo -simulaatioon ja prototyyppiä testattiin kliinisillä pilottitutkimuksilla. Esimerkiksi mallilla ennustettujen melaniini ja hemoglobiinikonsentraatioiden havaittiin korreloivan subjektiivisten, POSAS ja Vancouverin arpiasteikolla kuvattujen pigmentaation ja vaskularisaatioiden kanssa, mutta Spektrokutometrilla mitatut arvot olivat paremmin toistettavissa kuin subjektiiviset havainnot.

Asiasanat

iho, lähi-infrapunasäteily, absorptio, spektroskopia, Monte Carlo -menetelmät, kuvantaminen, mallintaminen, simulointi

Publisher	**Date of publication**	
Vaasan yliopisto	May 2011	
Author(s) Petri Välisuo	**Type of publication** Selection of Articles	
	Name and number of series Acta Wasaensia, 242	
Contact information University of Vaasa Faculty of Technology Department of Electrical Engineering and Energy Technology P.O. Box 700 FI-65101 Vaasa, Finland	**ISBN** 978-952-476-347-9 (paperback) 978-952-476-348-6 (pdf)	
	ISSN 0355–2667, 1798–789X	
	Number of pages 156	**Language** English

Title of publication
Photonics simulation and modelling of skin for design of Spectrocutometer

Abstract

Optical methods are especially well suited for clinical use, since non-contact optical measurements introduce minimal harm or risks to the patient. The structure of the skin and the absorption spectra of the most important chromophores of skin, melanin and haemoglobin favour measurements in the visual and near infrared wavelengths.

Contemporary medical practices are supposed to be evidence based. However, the treatment of skin disorders is mainly based on information obtained by subjective observations, which are proven to be non-repeatable, prone to interpersonal variation and difficult to document.

In this thesis, skin chromophore mapping problem is studied by constructing a light transport model based on diffusion theory and differential modified Beer-Lambert law, to predict the reflectance of skin in different conditions and by constructing a prototype, a Spectrocutometer, to standardise the conditions of subsurface diffuse reflectance imaging. A fast mapping method was developed to estimate the distribution of the skin chromophores from spatially high resolution multispectral images. The skin model was tested by comparing it with a Monte Carlo -simulation model and the prototype was validated in clinical studies. For example the estimated melanin and haemoglobin concentrations correlates with the subjective estimates of vascularisation and pigmentation in POSAS or Vancouver Scar Scales, but the measured values are more repeatable than the subjective observations.

Keywords

skin, near–infrared, absorption, spectroscopy, Monte Carlo –methods, imaging, modeling, simulation

PREFACE

The research summarised in this thesis has been carried out in the Automation group of the Department of Electrical and Energy Engineering in University of Vaasa, during 2006–2010. The research topic, to apply the NIR-spectroscopy to the analysis of skin disorders in Vaasa Hospital, was originally introduced by Professor Jarmo Alander. Instead of using the NIR spectroscopy, the author decided to use VIS-NIR multispectral imaging since even RGB imaging had been providing promising results in some research articles found by Jarmo. The first pilot was started in Vaasa in summer 2007, partly financed by TEKES and Abilita Oy. The pilot ended in the end of 2008 and its results were published but not included in this thesis. The work continued in 2009 together with MD Ilkka Kaartinen from Tampere University Hospital. Ilkka started to write his own dissertation from the medical aspects of objective skin measurements. Since that Ilkka organised the pilots, recruited the patients, and applied for the permissions needed for the studies and the author concentrated on the technical problems. Since autumn 2008 the work was financed by University of Vaasa, Tampere University Hospital and Finnish Cultural Foundation.

The research is done under the guidance of Professor Jarmo Alander, who was also the supervisor of this thesis, to whome I owe my best thanks. Jarmo has been especially important in creating networks of interdisciplinary researchers and finding piles of relevant prior art of any topic needed and suggesting the initial idea of this thesis.

I am also very grateful to Doctor Vladimir Bochko, the instructor of this thesis. In addition to the valuable scientific advice, Vladimir has helped me to speak English and he has been telling so many interesting Russian tales, introducing me to the Russian culture.

I owe my best thanks to the reviewers of this thesis, Professor Juha Röning from University of Oulu and Professor Paul Geladi from Swedish University of Agricultural Sciences. Both reviewers were extremely efficient and their accurate feedback helped to rise the quality of the final work.

I would like to express my gratitude to MD. Ilkka Kaartinen from the Tampere University Hospital. He has been extremely valuable for the success of this work. He knew what results are clinically relevant and made me believe it too. We made a lot of work

together, and it has been always a pleasure, to share a common interest on a scientific topic.

The early co-operators, specialists, colleagues, and sponsors deserve a special thanks too. Especially Professor Hannu Kuokkanen from Tampere University Hospital, MD Kaj Lahti, MD Markku Sirviö, MSc Paula Sillanpää from the Vaasa City Hospital, CEO Tommy Sjöholm and Johan Rönnqvist from Abilita Oy, Toni Harju, Olli Kanniainen, FIELD NIRCe project, Tekes – the Finnish Funding Agency for Technology and Innovation, The South Ostrobothnia Regional Fund of the Finnish Cultural Foundation.

I would like to express my gratitude for all the others contributing to this work directly or indirectly, which are too many to list here.

Finally, I would like to express my warmest appreciation to my wife Maarit and my two sons, Niklas and Aleksi, who have always somehow managed to understand, why I want to waste so many years, with low salary and uncertain future, pursuing towards further understanding of light propagation in tissue and one more degree. Without that understanding, my work would have been impossible.

Experience is simply the name we give our mistakes.
Oscar Wilde

Having finished this work, I am now apparently much more experienced.

In Vaasa, 2nd of May, 2011

Petri Välisuo

CONTENTS

List of figures

List of symbols

A . . . . . Absorbtion

$A_{\delta Hb}$, $A_{\delta mel}$ . . . . . Absorption change due to haemoglobin or melanin change

a' . . . . . Transport albedo

$\vec{B}$ . . . . . Magnetic field
β . . . . . Regression coefficient
β_{km} . . . . . Kubelka-Munk forward flux variable
c . . . . . Concentration
da . . . . . Differential area element
D . . . . . Diffusivity
δ . . . . . Penetration depth
d . . . . . Thickness of layer
dV . . . . . Differential volume element
$\vec{E}$ . . . . . Electric field
E_k, E_l . . . . . Coefficients for modelling edge losses in integrating sphere
F . . . . . Fluence rate
f_b . . . . . Relative blood fraction
f_m . . . . . Relative melanin fraction
g . . . . . Anisotropy
$\hat{n}$ . . . . . Unit normal vector
I . . . . . Intensity of light
I_0 . . . . . Intensity of incident beam
I_B . . . . . Intensity of the beam of ballistic photons
I_R . . . . . Intensity of reflected light
I_T . . . . . Intensity of transmitted light
I_H, I_V . . . . . Intesity of horizontally and vertically polarised light
I_L, I_R . . . . . Intensity of left and right circularly polarised light
I_{+45}, I_{-45} . . . . . Intensity of light polarised at an angle of $\pm 45^\circ$
K . . . . . Internal reflection coefficient
k . . . . . Kubelka-Munk absorbtion coefficient
K_m . . . . . Kubelka-Munk backward flux variable
λ . . . . . Wavelength
L . . . . . Radiance
μ_a . . . . . Absorbtion coefficient
μ_a' . . . . . Transport albedo
μ_{eff} . . . . . Effective interaction coefficient
μ_s . . . . . Scattering coefficient

μ_s' . . . . . Transport scattering coefficient
μ_t . . . . . Total interaction coefficient
n . . . . . Relative refraction coefficient
ϕ . . . . . Light flux
p . . . . . Pathlength
$p_{\mathrm{mf}},\ z_0$ . . . . . Mean free path length
Q . . . . . Light source in medium
R . . . . . Reflectance
R_d . . . . . Diffuse reflectance
r_d . . . . . Empirical constant for internal reflection
R_F . . . . . Fresnell reflection
R_W . . . . . Reflectance of reference white
ρ_s . . . . . Density of scattering particles
$S_0,\ S_1$ . . . . . Zeroth and first order Legrende polynomials
S_{O2} . . . . . Oxygen saturation
σ_s . . . . . Scattering cross section
s . . . . . Kubelka-Munk scattering coefficient
$S(z)$ . . . . . Source strength along z axis
$S(\lambda)$ . . . . . Sensor response
Θ . . . . . Light beam or photon angle
t_p . . . . . Time of the pulse
t . . . . . Time
T . . . . . Transmittance
U . . . . . $\sqrt{3(1-\mu_a')}$
ε . . . . . Extinction coefficient
$\vec{v}$ . . . . . Speed
ξ . . . . . Uniformly distributed random variable
z_b . . . . . Height of the virtual boundary

List of abbreviations

ADM . . . . . Adding Doubling Method
ARD . . . . . Automatic Relevancy Determination
BLL . . . . . Beer–Lambert law
CCD . . . . . Charge Coupled Device
CIE . . . . . Commission Internationale de L'Eclairage
CMOS . . . . . Complementary Metal Oxide Semiconductor
dmBLL . . . . . Differential Modified Beer Lambert Law
DOP . . . . . Degree Of Polarisation
DOT . . . . . Diffuse Optical Tomography
EI. . . . . Erythema Index
FWHM. . . . . Full Width at Half Maximum
GA . . . . . Genetic Algorithm
ISO . . . . . International Standards Organisation
IPD . . . . . Immediate Pigment Darkening
LCTF . . . . . Liquid Crystal Tunable Filter
LLS. . . . . Linear Least Squares
LMA. . . . . Levenberg-Marquardt
MCML. . . . . Monte Carlo Multi Layer
NIR . . . . . Near Infrared
NIRS . . . . . Near Infrared Spectroscopy
NLS . . . . . Non-linear Least Squares
OCT . . . . . Optical Coherence Tomography
PAT . . . . . Photoacoustic Tomography
PI. . . . . Pigmentation Index
QR. . . . . A matrix decomposition method
RBC . . . . . Red Blood Cell
RMSEP . . . . . Root Mean Square Error Percentage
RMS . . . . . Root Mean Squares
RTE. . . . . Radiative Transport Equation
SCO . . . . . Standard Colorimetric Observer
SVD . . . . . Singular Value Decomposition

TEM . . . . . Transverse Electromagnetic wave
UV . . . . . Ultra violet
VIS . . . . . Visual

List of publications

I Välisuo, P. & Alander, J. (2008). The effect of the shape and location of the light source in diffuse reflectance measurements. In *21st IEEE International Symposium on Computer-Based Medical Systems*, 81–86. 77

II Välisuo, P., Mantere, T. & Alander, J. (2009). Solving optical skin simulation model parameters using genetic algorithm. In *The 2nd International Conference on BioMedical Engineering and Informatics*, 376–380. 87

III Välisuo, P., Kaartinen, I., Kuokkanen, H. & Alander, J. (2010b). The colour of blood in skin: a comparison of Allen's test and photonics simulations. *Skin Research and Technology* 16: 4, 390–396. 95

IV Kaartinen, I. S., Välisuo, P. O., Bochko, V., Alander, J. T. & Kuokkanen, H. O. (2011b). How to Assess Scar Hypertrophy? A Comparison of Subjective Scales and Spectrocutometry – A New Objective Method. *Wound Repair and Regeneration* 19: 2. 105

V Välisuo, P., Harju, T. & Alander, J. (2011a). Reflectance measurement using digital camera and a protecting dome with built in light source. *Biophotonics* 4: 4. 115

VI Välisuo, P., Kaartinen, I., Tuchin, V. & Alander, J. (2011). New closed–form approximation for skin chromophore mapping. *Journal of Biomedical Optics* 16: 4, 046012. 129

1 INTRODUCTION

1.1 Overview and motivation

Vision is probably the most important human sense. The eyes contain lenses for focusing light to detector-elements, which are cones and rods. In bright light, vision is mainly taken care by three kinds of cones, which are all sensitive to different wavelengths of light. This forms the basis of the colour sense abilities of humans. The exact colour sense capabilities may be slightly different for each individual, but the colour sense of an average person is often approximated by standard colorimetric observer (SCO) curves, defined by the Commission Internationale de L'Eclairage (CIE), published in (CIE 1931).

There have been certainly many factors affecting the evolution of the tri-chromatic vision system of primates, including foraging capabilities and intra specific communication. The resulting colour vision system of humans is suprisingly good in observing subtle changes in blood concentration and oxygen saturation of the human skin (Changizi, Zhang & Shimojo 2006). These properties carry a lot of information about the moods, feelings and pathological changes of an individual. This is also shown in supplementary material in the article (Changizi *et al.* 2006), which studies which colours typically signify different moods in cartoons. Usually yellow means happy, blue is sad, red is angry and green is sick. These colour changes in turn are the consequences of changing blood concentration and oxygen saturation levels. The caucasian skin type is yellowish, where there is less blood than normally. Excessive blood makes the skin bluish or purple. High oxygen saturation makes skin redder and low oxygen saturation makes it a greenish colour. Therefore, individuals can partly sense the mood of others with their naked eye. The melanin concentration level is not important for communication, since it usually changes only slowly, although immediate pigment darkening (IPD) can occur within 10 minutes after expososure to ultraviolet radiation (Beitner 1988; Routaboul, Denis & Vinche 1999). Still, it is important to distinguish blood concentration and oxygen saturation behind the absorption of melanin.

In addition to observing the overall changes of the individual, the colour of the skin can also be used in studying local disorders of the skin. For example, the skin reacts to local mechanical irritation by a local regulatory mechanism, increasing blood perfusion and the permeability of blood vessels in the irritated area. The resulting inflammation

can be seen as increased redness of the skin, a condition called erythema. Infections and injuries start similar inflammation reactions and can therefore be observed by the colour change, too. To separate the effect of local changes from global changes, it is important to compare the colour changes between different locations. Common colour is probably due to global conditions and difference in colour due to local changes.

However, the perceptual colour of skin is not only dependent on the properties of skin. The spectrum of the illuminant is as important as the reflectance of the skin. The human colour perception system includes a colour constancy mechanism which partly compensates the effect of the light source spectra from the perception of the colour of the object (Ebner 2007). As a result, the human vision system is good in comparing colours simultaneously, even under differing illumination conditions. However, temporal comparison of the colours is significantly more difficult.

Because the colour perception capability of a human being is good in spectroscopy related to skin diagnostics, the subjective, visual assessment of skin is an important medical practice, as shown by various visual scaling systems in clinical use (Draaijers, Tempelman, Botman, Tuinebreijer, Middelkoop, Kreis & van Zuijlen 2004; Baryza & Baryza 1995). The challenges in subjective evaluations are that different individuals may perceive colours differently, the interior illumination conditions may vary too much between examinations to retain colour constancy, the colour perception may be non-linearly related to the strength of physiological factor causing the colour change, the documentation of colour sensation is difficult, and the comparison of colours seen at different times may be inadequate. Therefore, the measurement of skin reflectance may improve the diagnostics, documentation and follow-up of skin disorders.

1.2 Prerequisites of the thesis

Care personnel are often busy, and the problems related to skin are seldom life threatening, thus skin treatment is often perceived to be of secondary importance. Therefore, the time and resources available for careful examination of skin health is often limited. However, the importance of skin disorders is not negligible either in terms of the resources needed from hospitals or in regard to the perceived decrease in the quality of life for the patients. The diseases related to skin and *subcutis* as a main diagnosis costs more than 36 thousand hospital care days annually in Finland (National Institute for

Health and Welfare 2009). These diseases degrade the life of more than 1500 persons annually.

Automation could be used to reduce the burden of the personnel, and help them in providing even better treatment and follow-up of skin disorders, thus potentially reducing the number of care days required. The automated measurement could also be performed by non-experts, such as outpatients themselves at home, in some cases.

To be helpful, the automated skin disorder measurement system should be able to estimate as many clinically significant parameters as possible. The set of clinically significant parameters depends on the goal of the treatment, the type and severity of the disorder, the general condition of the patient, and many other factors. The assessment of typical skin disorders and scars and the follow-up of the healing of dermal injuries are described next.

The examination of skin disorders such as pressure ulcers, and burn, frost and traumatic injuries is made using subjective observation, palpation, measuring the width, height, area or volume manually, by drawing the shape of the wound in transparent film manually or photographing the wound (Hietanen, Iivanainen, Seppänen & Juutilainen 2002). In addition to these direct measures, laboratory examinations may also be needed to find out if the injury is infected by bacteria. The same methods can be used in analysing the injuries due to surgical incisions.

When the dermal injury is healing, it forms a scar. The assessment of skin scars is an important part of post-treatment and retrospective analysis of wound treatment. The scarring may cause cosmetic disadvantages, limit the mobility of body parts and cause pain, itch and altered sensation. The assessment of scars is often made using similar methods as the assessment of skin disorders. (Perry, McGrouther & Bayat 2010)

The healing of a dermal injury involves many physiological processes, among which inflammation is one of the most important. Inflammation causes vascularity and erythema of the disorder area by increasing the blood supply, often also leading to the higher oxygen saturation. The wound healing process often causes pigmentation, due to increased production of melanin. Sometimes the injury may cause vessel ruptures, causing blood to escape to extracellular space. The deposits of degradation products of the haemoglobin of escaped blood, such as haemosiderin, methaemoglobin, and

bilirubin may cause additional discolourisation of the skin. (Hughes, Ellis, Burt & Langlois 2004) The increased blood supply, oxygen saturation level, pigmentation and the deposits of blood degradation products may be observed as a change of skin colour. However, if the cause for discolourisation is deep in the skin, it can only be seen weakly or not at all by the naked eye.

An ultimate skin measurement system would measure as many of the listed properties of skin as possible. Many of these parameters may be measured using optical methods. The vascularisation and oxygen saturation are measured with VIS-NIR spectroscopy as shown in many research articles, some of which are are listed in the following reviews: (Wright, Kroner & Draijer R. 2006; Baranoski & Krishnaswamy 2008). The shape and dimensions of skin disorders can be obtained using optical planimetry, based on skin images (Bochko, Välisuo, Harju & Alander 2010; Kaartinen, Välisuo, Alander & Kuokkanen 2011a). The pliability and height of the scar are important factors in scar assessment (Publication IV). Potentially, these properties can also be measured with an optical device, using stereoimaging and an indentation mechanism for skin stretching.

The method capable of analysing vascularisation and oxygen saturation could also be used to measure the condition of the blood microcirculation and its control. This could be beneficial in examining the microcirculatory changes caused by diabetes or other diseases (Wright *et al.* 2006). The regulatory properties of microcirculation can be tested by measuring the vascularity while the blood circulation is disturbed (Clancy, Nilsson, Anderson & Leahy 2010).

Since this kind of optical skin measurement system would need spectroscopic methods to analyse the skin, it is called here Spectrocutometer, according to (Publication IV). Potentially, the Spectrocutometer could automate the measurement of the most important skin properties to an ubiquitous standard procedure, extending knowledge of the state of the wounds and providing a lot of objective information for making retrospective studies on wound healing.

1.3 Technologies

The visual and near infrared (NIR) wavelengths from 650 nm to 950 nm belong in the so called diagnostic-therapeutic-window, explained more carefully in Subsection (3.5).

The penetration depth of the wavelengths within this window is the highest. The melanin and haemoglobin will absorb the shorter wavelengths and water the higher wavelengths. Outside of the window, the measurements or phototherapy can not easily cover the whole skin depth. The wavelengths within the diagnostic-therapeutic window carry information deeper from the tissue than the other wavelengths. The Spectrocutometer should therefore work in the same range as the human eye, extended towards red, beyond the limits of the eye.

The Spectrocutometer should measure the reflectance, not the colour of the skin, since the reflectance is the property of the skin only, and it can be related to the optical absorbtion and scattering of the skin. The problem of colour constancy is then already handled as well. A light source which provides uniform light field and repeatable illumination is needed for reflectance imaging. Even though the wavelengths used by the human eye may be good for measuring the concentrations of the skin chromophores, the computer vision system needs not to be restricted by the capabilities of the eye. The spectral bands of the Spectrocutometer are optimised, in terms of prediction of the chromophore concentrations and convenience in producing those wavelengths. The reflectance of skin depends non-linearly on the concentrations of the chromophores and the scattering coefficient. Suitable models for simulation and prediction of the reflectance are needed in solving the clinical parameters from the observed reflectance.

1.4 Objectives

The topic of this thesis is to replicate the capabilities of the human colour vision system with computer vision, overcoming the limitations of subjective analysis. For this purpose, the following requirements need to be satisfied:

1. Accurate skin reflectance measurement. The colour depends both on the skin and the spectrum of the illuminant, the reflectance depends only on the skin. Colour constancy is achieved at the same time.
2. Measuring a reflectance image, instead of point wise measurement. The image makes it easier to separate local skin disorders from global changes. The spatial dimensions make the statistical evaluation of a skin disorder more reliable.
3. Closed form algorithm for calculating the chromophore concentrations of skin

fast enough to be applicable to the reflectance image.

4. Testing of the algorithm against versatile and realistic simulation.
5. Testing of the system against experimental measurement data.

1.5 Summaries of the publications and author's contribution

Publication I The article includes the study of the effect of the geometry of optical probe and the corresponding light source on the information depth. The author planned and carried out the measurements, made the simulations and wrote the entire manuscript, after which Prof. Jarmo Alander commented and proofread it.

Publication II The research included optimisation of the MCML simulation model using Genetic Algorithm (GA). The effects of noise generated by stochastic simulation and the choice of a fitness function, which would optimise the accuracy of the simulation were studied. The accuracy and uniqueness of the found optical parameters were tested. The author planned and carried out the simulations and programmed the GA implementation. Dr Timo Mantere gave advice in designing GA parameters and fitness functions and commented on the whole work. Prof. Jarmo Alander proofread and commented on the article.

Publication III The purpose of the research was to study quantitatively, how the change in blood concentration is seen as the change of reflectance or absorption of skin, in spectra and in tri-stimulus colour coordinates. The analysis was made by continuously measuring a reflectance spectra from the palm of the hand while performing the Allen's test, repeated with 20 test subjects. The blood concentrations during the Allen's test were solved by inverse MCML modelling technique. The measurements were planned and performed by the author and MD Ilkka Kaartinen together. The simulations were executed by the author. The article was written by the author and Ilkka Kaartinen, who specifically wrote the subsection considering the Allen's test, but also influenced the content in other sections. Prof. Hannu Kuokkanen and Prof. Jarmo Alander proofread and commented on the article.

Publication IV A multispectral imaging system, the Spectrocutometer, was implemented, and 37 scars were analysed with it and with three independent observers.

The chromophore maps of the scars were analysed using inverted skin model. The obtained chromophore concentrations were compared with the parameters of subjective scales, which are frequently used in clinical scar assessment. The statistical dependency model was built to find out the relations between the subjective and measured parameters as well as the symptoms. The study was planned and organised by MD Ilkka Kaartinen. The measurements were carried out by the author and Ilkka Kaartinen together. The article is mainly written by Ilkka Kaartinen. The author participated in writing subsections describing image acquisition and spectral modelling, and by performing the chromophore concentration estimates of the images. The Bayesian network was also constructed by the author. Dr Vladimir Bochko performed the automatic relevancy determination (ARD) calculations. Prof. Hannu Kuokkanen and Prof. Jarmo Alander proofread and commented on the article.

Publication V The purpose was to find out the accuracy of the Spectrocutometer in reflectance measurement. The accuracy was estimated by comparing the Spectrocutometer reflectance values with known values and with the values acquired by a spectrometer with an integrating sphere as a probe. A formula for compensating interreflectance was proposed for both integrating sphere and Spectrocutometer. The measurements were designed and implemented by the author. MSc Toni Harju designed and built the illumination and light control unit of the Spectrocutometer. The author wrote the manuscript and Prof. Jarmo Alander proofread and commented on it.

Publication VI In this publication the chromophore estimation algorithms were improved. A hybrid skin model, based on the diffusion model of dermis and the Beer-Lambert model of epidermis was constructed. A new fast chromophore concentration estimation method was designed by using differential modified Beer-Lambert law (dmBLL). The validity of the model was tested by comparing it with a MCML model. The analytical differentials needed for the dmBLL were obtained by differentiating the hybrid model. The edge losses of the integrating sphere were also simulated, and a compensation method proposed. The author planned the research, designed and implemented the models, carried out the simulations and wrote the manuscript. Prof. Valery Tuchin and Prof. Jarmo Alander proofread the manuscript and gave many valuable comments.

1.6 Contributions of the dissertation

The main contribution of the dissertation is a new approach to measuring skin chromophore concentrations from multispectral image. A more specific list of contributions is as follows:

- Optical probes
  - analysis of the information depth of optical probes and the analysis of the effect of the geometry on the information depth, and simulation of the superiority of ring shaped probe (Publication I)
  - analysis and compensation of non-linearity due to interreflectance in highly reflected dome-shaped probes, such as integrating spheres (Publication V)
  - analysis and compensation of edge losses in an integrating sphere (Publication VI)
  - estimation of the accuracy of multispectral imaging with calibrated digital camera and a dome-shaped probe with built-in illumination system (Publication V)
- Skin reflectance modelling
  - *in vivo* measurements of the reflectance of skin, both in spectra and in tristimulus coordinates, when the blood concentration is modulated, to help in finding a suitable method in predicting the blood concentration (Publication III)
  - design of a new hybrid skin model, based on a combination of diffusion theory and Beer-Lambert law (Publication VI) and comparison with Monte Carlo Multi Layer (MCML) model
- Inverse solution of optical parameters of skin
  - analysis of the uniqueness, accuracy and spectral resolution needed for solving the skin chromophore concentrations using inverse MCML simulation model (Publication II)
  - design of a novel, fast method for approximating the skin chromophore concentrations using differential modified Beer-Lambert law, and analytical derivatives of diffusion theory based skin model (Publications III, IV and VI)

- Application of chromophore mapping in scar analysis
  - applying the chromophore concentration estimation method to a set of multispectral images of matured scars, and the estimation of chromophore concentrations in studying the hypertrophy and activity of scars (Publication IV)
  - statistical analysis of the clinical properties of scars (Publication IV)

1.7 Outline of the dissertation

The dissertation is divided into six sections. After the introduction, the second section discusses the modelling of the light interactions in a complex medium, such as human skin. It consists of a description of the terminology, different optical phenomena and models most often used for describing light transport. Section three describes the structure of the skin with relation to its optical properties. The sources of absorption and scattering are explained. The devices, techniques, and existing equipment for measuring skin reflectance are outlined in Section four. Both direct and model–based methods are covered, including algorithms for solving the corresponding inverse problem. The most common light interaction models are introduced, including Kubelka-Munk theory, diffusion theory and Monte Carlo simulation. Existing commercial equipment and research prototypes for optical skin measurement are briefly reviewed. The prototypes of the Spectrocutometer are presented in Section five, where its main parts, principles and related methods are discussed. Chromophore mapping, as implemented in the pilot studies, is explained. A new approximative closed form algorithm for chromophore mapping is shown. Finally, a pilot study of linear scar assessment is presented. Section six states the conclusions of the work.

2 MODELLING OF RADIATIVE TRANSPORT

The main purpose of the optical measurements in this thesis, is to obtain quantitative information about the internal structure and content of a medium by examining how it absorbs light at different wavelengths. Unfortunately, the relationship between the light absorbtion and content is not straightforward. Therefore, modelling of light interaction with the medium is needed in order to connect the absorbtion and properties of the medium together. This section explains the theories and models most often used for explaining the interaction of light with a medium.

2.1 Optical phenomena

The basic modes for light to interact with matter are refraction, reflection, scattering, absorbtion, emission, and change of polarisation. These phenomena are discussed in detail in this subsection.

2.1.1 Reflection

When the light beam crosses a boundary with differing refractive indices, the light is partly reflected back from the surface. This reflection is called specular, interface or Fresnel reflection. Part of the light may cross the boundary, and change is speed, due to the difference in the refraction coefficients. The difference in speeds causes refraction, a change of direction of the transmitted light, according to Snell's law.

The strength of the Fresnel reflection of a collimated beam, the incident angle of which is normal to the skin surface was derived already at the beginning of 19th century by Augustin Fresnel. The derivation of the formula, known as the Fresnel equation is shown in (Hecht & Zajac 1974). In case the collimated beam of light is incident orthogonally to the air-dielectric surface, the specular reflectance, R_F, is:

$$R_F = \left(\frac{1-n}{1+n}\right)^2 [\text{unitless}], \tag{1}$$

where n is the relative index of refraction of the dielectric. For example, for skin $n = 1.37$, $R_F = 0.024$.

2.1.2 Absortion

The part of electromagnetic radiation which can be detected by human eye is called visible light. Visible light includes wavelengths from approximately 400 nm to 800 nm. The range of visible light (VIS) resides between ultra violet (UV) and near infrared (NIR). The UV range includes wavelengths from 20 nm to 400 nm, and the NIR range from 800 nm to 2400 nm. The mechanisms for electromagnetic radiation interaction with matter depend on the energy of the photons, which is inversely proportional to the wavelength of the radiation.

Absorption in the visual (VIS) range occurs when the energy of the photon matches the energy difference between the valence electron states of the atoms. In this case, the photon may be absorbed, and the electron is transferred to the next energy level. Eventually the energy level of the atom will return to the lower energy state, releasing the absorbed energy. Part of the released energy may be emitted as a photon. These emitted photons are detected as fluorescent light. If the fluorescence happens in the intrinsic atoms or molecules of the material, the phenomenon is called autofluorescence. In some cases, external fluorophore may be placed in the material to make fluorescent analysis. The excitation energy is more often released as thermal energy, and no fluorescence happens. In the ultra violet (UV) range, the absorption is similar to that in the VIS range, but the energy of the photons is high enough to sometimes totally release the electrons, thus ionisating the atom. The photons in the NIR range have such low energy that they cannot excite the electrons. Instead, they may change the energy levels of the molecules by transforming them, or part of them from one vibrational state to another. For this reason, NIR spectroscopy is well suited for chemical analysis, since the absorption wavelengths reveal the existence of certain chemical bonds.

2.1.3 Scattering

Scattering occurs when a photon interacts with a particle in the medium where molecules are unordered, changing its direction, but not losing its energy. If the dipoles caused by the molecules of the substance are equally distributed and oriented, the substance does not scatter, but refract light, since the forces in the matter cancel each other out. For example, light is not significantly scattered in water or in glass. On the other hand, light is strongly scattered in snow, since the volumes of frozen water and air alternate in snow, causing many irregular borderlines where the refraction coefficient changes. In

most of the scattering events the energy is conserved. This kind of scattering is called elastic scattering. An example of inelastic scattering is Raman scattering, which can be studied using a specific Raman spectrometer. The change of direction of a photon in each scattering event is described by means of a phase function, $p(\vec{s},\vec{s}')$. The phase functions gives the probability of the photon being scattered in the direction of $\vec{s}'$ when it was propagating to direction $\vec{s}$ before the scattering event. If the phase function is forward peaked, the media is said to be forward scattering. On the other hand, in backward scattering material, the phase function is backward peaked. If all directions are equally probable after scattering, the medium is said to be isotropic. Due to the scattering, some photons which have already entered into the media, may reverse their direction due to scattering, and they exit the media from the side of the illumination. This reflection of photons inside of the medium is called backscattering, subsurface reflectance, body reflectance, or diffuse reflectance. In this text, this kind of reflectance is called diffuse reflectance.

When the photons scatter from particles smaller than the wavelength of light, Rayleigh scattering dominates, whereas the scattering from particles larger than the wavelength of light is modelled as Mie scattering. Mie scattering is derived by solving Maxwell equations in the case of spherical scattering objects. Blue sky is caused by Rayleigh scattering of light from atoms and molecules in the atmosphere. Rayleigh scattering depends on the wavelength in the form $k \cdot \lambda^{-4}$, where k is constant. The scattering of short wavelengths, like blue, is much stronger than the scattering of long wavelengths, like red. A rainbow is caused by Mie scattering of light in water drops. Mie scattering is much less wavelength dependent, $k \cdot \lambda^{-1.5}$.

2.1.4 Turbidity

A substance having both significant scattering and absorption is called turbid, because it is difficult to see through. The absorption in the turbid media reduces the light which can be used for measurements. The scattering distorts the directional information of the photons, making the images blurred. Mathematical modelling of turbid media is also more difficult than the modelling of purely reflecting or purely scattering media.

2.1.5 Polarisation

Electromagnetic radiation, such as light, propagates in air and other dielectrics as a transverse electromagnetic wave, TEM. In a TEM-wave the electric $\vec{E}$ and magnetic fields $\vec{B}$ are perpendicular against each other and the direction of propagation. If the orientation of the polarisation plane spanned by the direction of propagation $\vec{v}$, and $\vec{E}$ is constant, the electromagnetic field is said to be linearly polarised. The amount of horizontal and vertical polarisation of TEM propagating the direction of the z-axis is obtained by projecting a unit vector, parallel to $\vec{E}$, to the x- and y-axes. IF the $\vec{E}$ is oriented along the x- or y-axis, TEM is said to be horizontally, I_H, or vertically, I_V, polarised. If the $\vec{E}$ is rotating around z-axis, the light is said to be circularly polarised. Circular polarisation can be oriented to the left, I_L, or right, I_R. Mathematically, the state of the polarisation of TEM can be expressed by using a Stokes vector, introduced by G. G. Stokes in the middle of the 19th century. The Stokes vector is described in (Hecht & Zajac 1974), as follows:

$$\mathbf{S} = \begin{pmatrix} I \\ Q \\ U \\ V \end{pmatrix} = \begin{pmatrix} I_H + I_V \\ I_H - I_V \\ I_{+45^\circ} - I_{-45^\circ} \\ I_R - I_L \end{pmatrix}, \tag{2}$$

where I_{+45° and I_{-45° represent the polarisation at 45° degree with the x-axis. Note that without I_{+45° and I_{-45° the 45° polarisation angle would be mixed with zero polarisation. In (Hecht & Zajac 1974) the components of the Stokes vector were $[S_0, S_1, S_2, S_3]^T$, but here the components are named $[I, Q, U, V]^T$ according to (Ramella-Roman, Prahl & Jacques 2005; Tuchin 2007).

A polariser is a filter which only lets through a light which is polarised in a specific way, and filters away other components. For example, a vertically oriented linear polariser, P_l, will only pass through the I_V component. By changing the orientation of the linear polariser, the I_H, I_{+45°, and I_{-45° components can be selected as well. Similarly, a left and right circular polariser can be used to select either I_R or I_L.

The degree of polarisation can be defined by utilising the components of the Stokes vector, degree of polarisation (DOP) (Hecht & Zajac 1974):

$$\mathrm{DOP} = \frac{\sqrt{Q^2 + U^2 + V^2}}{I} \tag{3}$$

Initially polarised light gradually looses its polarisation in elastic scattering events. Therefore, the Fresnell reflection and single scattered light retains its polarisation, whereas the polarisation of multiple scattered light is mixed. The Fresnell reflection and single scattered light can be attenuated by covering the light source with a linear polarisation filter to polarise the incident light. Another linear polarisation filter is placed between the sensor and the object, oriented orthogonally against the polariser on top of the light source. (Tuchin 2007). Approximately half of the multiple scattered light penetrates through the second polarising filter. This cross-polarisation configuration enhances the contrast of the details beneath the surface, while attenuating the features close to the surface.

2.1.6 Time domain analysis

When a very short light pulse, $t_p \ll 1$ ns, is transmitted through turbid media, the light pulse spreads in time. Those photons, which avoid scattering, travel directly through the media, and come out first. Those ballistic photons are only affected by refraction at the boundaries and absorption in the medium. The time taken for the ballistic photons of the orthogonal collimated beam to travel through a layer of thickness d is $t = d/v$, where v is the speed of light in the medium. The energy conveyed by the ballistic photons is the energy of incident light subtracted by the absorbed energy during distance d. The intensity of ballistic photons, I_B, can be used in studying the absorption of the medium, since energy is absorbed at constant rate, determined by the absorption coefficient.

The scattered photons need to travel longer, and therefore they will reach the other side of the medium later. The travelling time is usually longer, the more scattering incidents the photon confronts. Those photons, which are only a little affected by scattering, are called snake photons. The rest of the photons are multiple scattered photons, which have lost direction information and are therefore diffuse. Because the directional information is lost, the imaging techniques using multiple scattered photons yield blurred images. Several techniques are available for gating multiple scattered photons out of the received signal. Some of them work in the spatial domain, like confocal microscopy, and some work in the frequency domain, like optical coherence tomography (OCT). The disadvantage of methods using only ballistic and snake photons is that a great deal of light is lost, and the losses increase exponentially when the transmission thickness increases. The same kind of spreading can be observed in reflected light, too. The

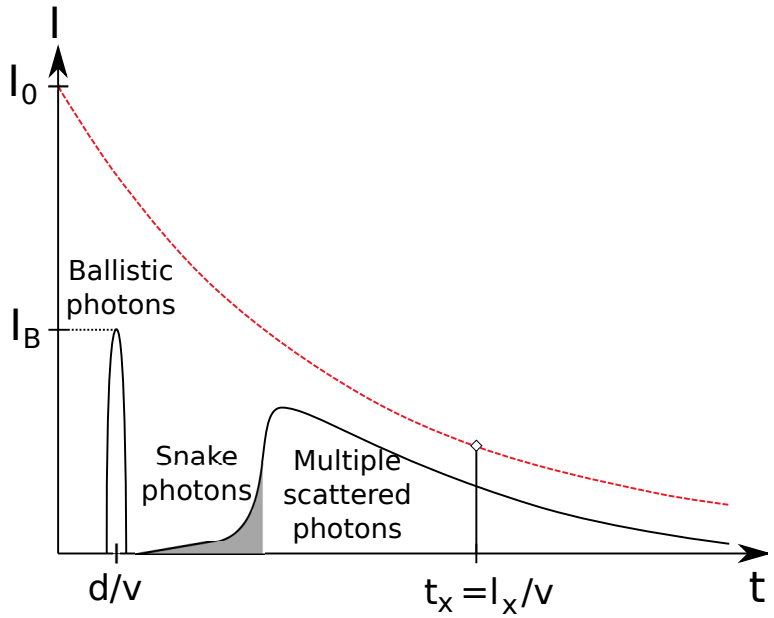

Figure 1. Spreading of a very short time light pulse in turbid media. When the light pulse, I_0, is launched in turbid media, at time $t = 0$, the first photons transmitted through are the ballistic photons at time $t = d/v$. The snake photons and multiple scattered photons will follow soon after. The maximum intensity of light transmitted at any moment is limited by the exponential absorption curve plotted as dashed line. If every photon followed the same path, the length of which is l_x, only one intensity peak at time instant t_x would be observed, and its intensity would be exactly at the dashed line. If the medium is purely absorbing, only a ballistic component is observed, and its intesity, I_B, can be used in determining the absorption of the medium.

reflectance signal contains Fresnel reflection, single scattered photons, and multiple scattered photons, but no ballistic photons.

2.1.7 Summary of light interaction with a turbid medium

Figure 2 summarises light interaction with turbid media. The first part of the incident light is scattered. The proportion of reflected light can be calculated from Fresnel law, and the angle of refraction from Snell's law. The reflected light is partly polarised, and so is part of the light which enters into the medium. In a turbid medium, the photon can be absorbed or scattered with certain probabilities determined by the scattering cross section and density of the scattering particles and the concentration and absorption strength of the absorbing particles. Part of the photons are transmitted through the media without any scattering, or only slightly deviating from the original course.

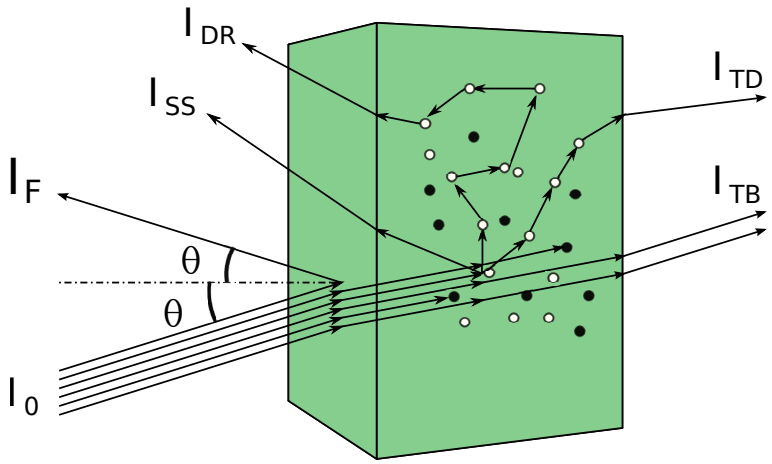

Figure 2. Light interaction with turbid media, when illuminated by a collimated light beam I_0. I_F depicts the intensity of Fresnel reflection from the boundary of the media, I_{SS} represents single scattered light beam, I_{DR} is the diffuse reflected and multiple scattered light beam. I_{TB} and I_{TD} shows transmission, either ballistic or diffuse intensity. The light, which is not reflected nor transmitted, is absorbed.

Although, the reflectance and transmission in turbid media can be easily measured, the determination of the intrinsic optical properties, absorption and scattering, is still hard in general cases, since scattering and absorption are intermixed in a complicated way. Usually some kind of model is used in solving the optical properties of the medium based on reflectance and transmission measurements.

2.2 Optical modelling of turbid media

The absorption of a substance is usually expressed as an absorption coefficient, μ_a, which is the molar absorptivity, or extinction coefficient of the chromophore, ε [1/cm/-mol], multiplied by the concentration of the chromophore, c [mol]. The molar extinction coefficient of a substance usually depends on the wavelength, λ. Therefore the absorption coefficient is (Ishimaru 1977; van Gemert, Jacques, Sterenborg & Star 1989):

$$\mu_a(\lambda) = c\,\varepsilon(\lambda) \qquad [1/\mathrm{cm}] \tag{4}$$

The inverse of the absorption coefficient is the mean free pathlength, $p_{\mathrm{mf,a}}$, of a photon between absorption events.

The scattering of light in a substance is often described using a scattering coefficient, $\mu_s(\lambda)$. The scattering coefficient depends on the density of the scattering particles, ρ_s [1/cm^3], and the scattering cross section of the particles, σ_s [cm^2]. Therefore, according to (Ishimaru 1977; van Gemert *et al.* 1989):

$$\mu_s(\lambda) = \rho_s \, \sigma_s(\lambda) \qquad [1/\mathrm{cm}] \tag{5}$$

The scattering coefficient is the inverse of the mean free pathlength, $p_{\mathrm{mf,s}}$, between the scattering events.

Scattering in tissue can be modelled using the Mie and Rayleigh scattering modes (Saidi, Jacques & Tittel 1995). Mie scattering occurs from large tissue structures, such as collagen fibers. Mie scattering in tissue is anisotropic, biased towards forward scattering. The scattering events from particles smaller than wavelengths, such as from various small skin organelles, can be modelled as Rayleigh scattering, which leads to scattering oriented almost equally to all directions (Saidi *et al.* 1995). This kind of scattering is called isotropic. The scattering angle is stochastic, but the tendency for forward or backward scattering is an expectation value of the cosine of the phase function, normalized (Jacques, Alter & Prahl 1987; Gandjbakhche 2001):

$$g = \langle \cos\theta \rangle = 2\pi \int_0^{\pi} p(\theta) \cos(\theta) \sin(\theta) \mathrm{d}\theta \tag{6}$$

Many estimates of the tissue phase function are used. The most common phase functions are probably the delta–Eddington (Joseph, Wiscombe & Weinman 1976) and Henyey–Greenstein phase functions (Jacques *et al.* 1987; Gandjbakhche 2001). The Henyey–Greenstein phase function was first used in modelling interstellar scattering, but it is shown to be suitable also in describing scattering in skin and other biological tissues. The Henyey–Greenstein phase function is the following:

$$p(\theta) = \frac{1}{4\pi} \frac{1 - g^2}{(1 + g^2 - 2\, g\, \cos\theta)^{3/2}} \tag{7}$$

The scattering of a photon is depicted in Figure 3. The Henyey–Greenstein phase function and the scattering angle are also shown.

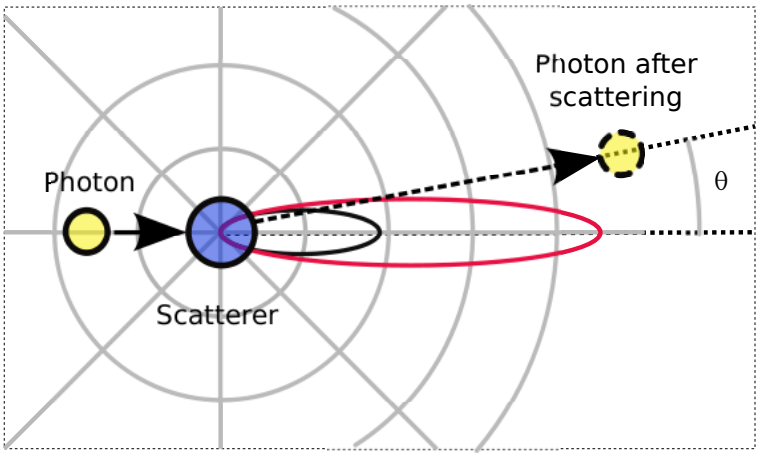

Figure 3. The scattering of the photon from the scatterer. The scattering angle, θ is the angle between the original direction of the photon and the direction after the scattering event. The larger ellipse depicts the probability density of the scattering angle, calculated using the Henyey–Greenstein phase function, when the anisotropy, $g = 0.8$, and the smaller ellipse, when $g = 0.7$.

If the anisotropy factor $g = 0$, the scattering is fully isotropic. In pure forward scattering media, $g = 1$ and $g = -1$ in the case of pure backward scatter. The average anisotropy of the skin is often: $g \in [0.7, 0.95]$ (Tuchin 2007; Gandjbakhche 2001).

When a collimated beam of light enters into a strongly scattering substance, it will become isotropic when undergoing enough scattering events, even if the substance is heavily forward scattering. Therefore, it is common to replace the scattering coefficient and the anisotropy with reduced scattering coefficient:

$$\mu_s' = \mu_s(1-g) \qquad [1/\text{cm}] \tag{8}$$

The reduced scattering coefficient describes the medium in which the scattering is purely isotropic, but weaker than in the original medium. If the path of the light beam in the medium is long enough to make the light isotropic, the net result of medium having scattering μ_s and anisotropy g is approximately the same as the medium with μ_s' and $g = 0$. Therefore, μ_s' is usually used instead of and μ_s and g.

By combining the effects of scattering and absorption, a total interaction coefficient, μ_t, is obtained.

$$\mu_t = \mu_a + \mu_s \qquad [1/\text{cm}] \tag{9}$$

2.2.1 Radiative transport equation

The propagation of electromagnetic radiation is often described by Maxwell equations. However, the skin may be too complicated a medium for Maxwell equations, due to the inhomogeneity and complex micro structures. For more than twenty years, the light transport equation (RTE) has been more popular in tissue optics than the Maxwell equations. The RTE model assumes that the light follows purely the particle model, there is no interaction between photons, nor interference. The motivation in RTE modelling is to predict the energy transport in turbid media. For this purpose, the RTE models the time and space change of radiance, the flux density, in the tissue. Radiance, L [W/m^2/sr], is a radiometric measure which indicates how much radiation originating from a particular area is transmitted to the given solid angle. The light transport in tissue can be modelled by examining how the radiance changes when it passes through an infinitely small volume. The RTE is shown in Equation (10) (Chandrasekhar 1960; Ostermeyer 1999; Thompson 2004):

$$\frac{1}{v}\frac{\partial}{\partial t}L(\vec{r},\vec{s},t) = -\underbrace{\vec{s}\cdot\nabla L(\vec{r},\vec{s},t)}_{\text{net flow}} - \underbrace{\mu_t L(\vec{r},\vec{s},t)}_{\text{losses}} + \underbrace{\mu_s \int_{4\pi} L(\vec{r},\vec{s},t)\,p(\vec{s},\vec{s}')\,\mathrm{d}\omega'}_{\text{scattering gain}} + \underbrace{Q(\vec{r},\vec{s},t)}_{\textit{sources}}, \tag{10}$$

where L is the radiance of light at location $\vec{r}$ moving towards $\vec{s}$. In volume element in location, $\vec{r}$, the radiation is scattered to a new direction, $\vec{s}'$. The scattering angle is determined by the scattering phase function, $p(\vec{s},\vec{s}')$.

The left hand side of RTE is the time derivative of radiance L, divided by the speed of light in the medium, v, to represent the change of radiance per distance travelled. This change is caused by the four additive terms on the right hand side. The first of these terms is the net flow through the volume element. If the spatial derivative of radiance parallel to $\vec{s}$ is nonzero, the net flow through the volume element equals the negative derivative along $\vec{s}$. The second term accounts for scattering and absorption losses within the volume. All absorption and scattering is counted. The third term describes the increase of radiance, due to the scattering into the direction of $\vec{s}$. The last term represents the net source within the volume element, dV.

In steady state condition, without sources, the RTE can be written as (Cheong, Prahl & Welch 1990; Ostermeyer 1999):

$$\vec{s} \cdot \nabla L(\vec{r},\vec{s}) = -\mu_t L(\vec{r},\vec{s}) + \mu_s \int_{4\pi} L(\vec{r},\vec{s}\,')\, p(\vec{s},\vec{s}\,')\, \mathrm{d}\omega', \tag{11}$$

Even Equation (11) is too complicated to be used in the practical modelling of light transport in skin. Therefore, the RTE is usually approximated in order to obtain a more tangible model. The most common analytical approximations of RTE include Beer–Lambert–Bouguer law, Adding-Doubling method (Prahl, Van Gemert & Welch 1993), Kubelka-Munk theory (Kubelka & Munk 1931), and diffusion approximation (Ishimaru 1977). In addition to analytical approximations, the numerical approximation by stochastic Monte Carlo simulation (Prahl, Keijzer, Jacques & Welch 1989) is also common.

2.3 Beer–Lambert–Bouguer law

If, the scattering is negligible, the RTE can be further simplified from Equation (11). Assuming a collimated beam is directed orthogonally to a slab of purely absorbing material, residing in the x-y-plane of the coordinate system. The beam is focused on an infinitesimal area, da. The radiance along the z-axis is only a function of z. The first term of Equation (11) thus becomes $d/dz\, L(z)$. The interaction coefficient reduces to plain absorption coefficient. The third term totally disappears, when μ_s is zero. The light intensity due to the radiance is $I(z) = L(z)\mathrm{d}a$. Therefore:

$$\frac{\mathrm{d}}{\mathrm{d}z} I(z) = -\mu_a I(z) \tag{12}$$

This differential equation can be solved by first rearranging the terms:

$$\frac{1}{I(z)} \mathrm{d}I(z) = -\mu_a \mathrm{d}z \tag{13}$$

and by integrating both sides:

$$\ln(I(z)) = -\mu_a z + C \tag{14}$$

The decrease of intensity I_0 through a slab of thickness d is:

$$\ln(I_0) - \ln(I) = \mu_a d \tag{15}$$

This can be exponentiated and rearranged to show the proportion of light transmitted through the slab:

$$T = \frac{I}{I_0} = e^{-\mu_a d}, \tag{16}$$

which is the Beer–Lambert–Bouguer law.

Originally, the Beer–Lambert–Bouguer law was derived much before radiative transport theory was established, based on experimental data. In the 18th century, Pierre Bouguer studied the absorbtion of light in a smoked glass. He noticed that when the light was transmitted through several layers of semi-transparent objects, each of them attenuate not an equal amount of light but an equal fraction of remaining light. He also noted that the attenuation was directly related to the thickness of the object. This result was later cited by Johan Lambert and he derived a formula based on Bouguer's observations. Beer finalised the formula, which defines the relationship between the concentration of light absorbing chemical and the attenuation of light in the following form:

$$I_T = I_0 e^{-\mu_a d}, \tag{17}$$

where I_T is the amount of light transmitted through the object, I_0 is the intensity of the incident light, μ_a is absorbtion coefficient of the material and d is the thickness. A typical measurement setup for transmission spectroscopy is shown in Figure 4(a). Equation (17) is often used in determining the concentration of a certain chemical. In this case, the unknown mixture of chemicals is poured into a cuvette, of known thickness, d. Then the cuvette is illuminated from the other side with a light source, the spectrum of which, $I_0(\lambda)$, is known. Then the transmittance spectrum $I_T(\lambda)$ is measured. The transmittance spectrum can be used qualitatively in determining the chemicals contained by the sample, and quantitatively in determining the concentration of the chemicals. For determining the concentration, the absorbtion efficiency of the chemical per concentration unit needs to be known. This absorbtion efficiency, $\varepsilon(\lambda)$, is known as the molar absorbtion coefficient or extinction coefficient of the chemical. The relationship between the absorption coefficient, concentration, c, and the extinction coefficient is the following:

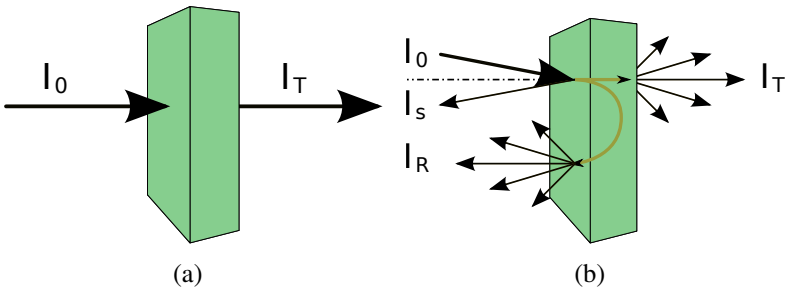

Figure 4. Typical setups for (a) transmission and (b) reflectance spectroscopy. The light rays depicted are the incident light, I_0, transmitted light, I_T, diffuse reflected light, I_R, and specularly reflected light I_F.

(18) $$\mu_a(\lambda) = c \cdot \varepsilon(\lambda)$$

By substituting Equation (18) for Equation (17), the relationship between concentration and the transmittance spectrum is obtained:

(19) $$I_T(\lambda) = I_0(\lambda) e^{-c\varepsilon(\lambda)d}.$$

The ratio of the spectra with sample, I_T and without, I_0 depends on the concentration in an exponential manner. By defining that the absorbtion of the substance, $A(\lambda)$, is the negative logarithm of the ratio of the transmitted and the incident light, $A(\lambda) = -\ln(I_T/I_0)$, Equation (19) can be written as follows:

(20) $$A(\lambda) = c\varepsilon(\lambda)d.$$

Equation (20) is known as Beer-Lambert-Bouguer law, often abbreviated to Beer-Lambert law (BLL).

BLL in simple form works only for transmission spectroscopy, when the scattering of the radiation is negligible in the measured substance. In scattering material, some of the photons will change directions in the substance. In this case, they may penetrate through the sample, but still be missed by the detector. If the scattering is strong, it is probable that a significant part of the incident beam will be diffuse reflected back to the incident side of the sample. Both diffuse reflected light and transmitted light conveys information about the internals of the substance. Therefore, they can both be used in absorption spectroscopy. A setup for reflection spectroscopy is shown in Figure 4(b). The specularly reflected signal is not only dependent on the spectra of the illuminant, the incident angle and the refraction index mismatch in the boundary of the object. It is therefore usually an unwanted signal, which is best avoided. The specular reflectance

can sometimes be avoided by designing the measurement setup so that the angle of the received signal is different from the angle of incident light. However, this cannot be applied in all situations. Another common method is to utilise cross-polarisers, as explained in Section (2.1.5).

2.4 Diffusion theory

The Beer–Lambert law does not hold when scattering is not negligible. Diffusion theory works for almost the opposite case, when scattering is strong and absorption is weaker.

In a medium where scattering is much stronger than absorption, $\mu_a \ll \mu_s'$, the RTE can be simplified using diffusion approximation. According to diffusion approximation, in areas far away from light sources and tissue boundaries, the light flux attenuates exponentially:

$$\phi(\vec{r}) \approx k e^{-\mu_{\text{eff}} r}, \tag{21}$$

where k is constant and μ_{eff} is an effective attenuation coefficient:

$$\mu_{\text{eff}} = \sqrt{3 \cdot \mu_a \left(\mu_a + \mu_s'\right)} \qquad [1/\text{cm}] \tag{22}$$

In strongly scattering media, light propagation becomes almost isotropic. Then radiance at point $\vec{r}$, $L(\vec{r},\vec{s},t)$ can be replaced with fluence rate $F(\vec{r},t)$, which is defined as the net radiance flowing out from the infinitesimal volume at point $\vec{r}$. It can be obtained by integrating the radiance over the closed surface, an infinitesimal sphere surrounding the volume element:

$$F(\vec{r},t) = \oint_{4\pi} L(\vec{r},\vec{s},t)\mathrm{d}\omega \qquad [\text{W}/\text{m}^2] \tag{23}$$

If the radiance is spherically symmetric, it can be represented as an infinite sum of Legendre polynomials. If the two first terms of the corresponding Legendre polynomials are used, and the rest are ignored, the resulting approximation of RTE can be solved in many practical cases. The resulting diffusion equation is (Ishimaru 1977; Cheong *et al.* 1990; Farrell, Patterson & Wilson 1992):

$$\nabla^2 F(\vec{r}) - \frac{\mu_a}{D} F(\vec{r}) = \frac{S_0(\vec{r})}{D} + 3\nabla \cdot S_1(\vec{r}) \tag{24}$$

where S_0 and S_1 are the zeroth and first order Legrende polynomials and the diffusion constant:

$$D = \frac{1}{3(\mu_a + \mu_s')} \qquad [cm]. \tag{25}$$

Since Equation 24 is inhomogeneous, it is often solved using Green's function. Green's function for isotropic point source, in an infinite medium is (Farrell *et al.* 1992):

$$F(r,z) = \frac{1}{4\pi D} \frac{e^{-\mu_{\text{eff}} r_1}}{r_1}, \tag{26}$$

where r and z are the distances in radial and depth directions from the light source, and r_1 is the diagonal distance:

$$r_1 = \sqrt{r^2 + (z - z_0)^2} \tag{27}$$

The fluence rate in a mismatched tissue-air boundary must fulfill a boundary condition (Farrell *et al.* 1992):

$$F(\vec{r}) - 2KD\hat{n} \cdot \nabla F(\vec{r}) = 0, \tag{28}$$

where $\hat{n}$ is a unit normal vector of the boundary, directed into the tissue, and K is the internal reflection constant, which can be calculated using either Fresnel reflection coefficients or using empirical variable r_d and relative reflection coefficient of the tissue air interface $n_{\text{rel}} = n_{\text{tissue}}/n_{\text{air}}$ (Farrell *et al.* 1992):

$$r_d = -1.440 n_{\text{rel}}^{-2} + 0.710 n_{\text{rel}}^{-1} + 0.668 + 0.0636 n_{\text{rel}} \tag{29}$$

Then K can be obtained as follows:

$$K = \frac{1 + r_d}{1 - r_d} \tag{30}$$

As described in (Farrell *et al.* 1992), a semi-infinite medium, illuminated by a collimated laser source can be roughly estimated by an isotropic point source placed one mean free pathlength, $z_0 = p_{\text{mf}} = 1/(\mu_s' + \mu_a)$, beneath the surface. The boundary conditions in a semi-infinite medium can be satisfied by placing an equal isotropic point

source at the distance of $2z_b + z_0$ above the skin surface. The virtual skin boundary is formed at the distance of z_b above the real surface, where:

(31) $$z_b = 2KD \qquad [cm]$$

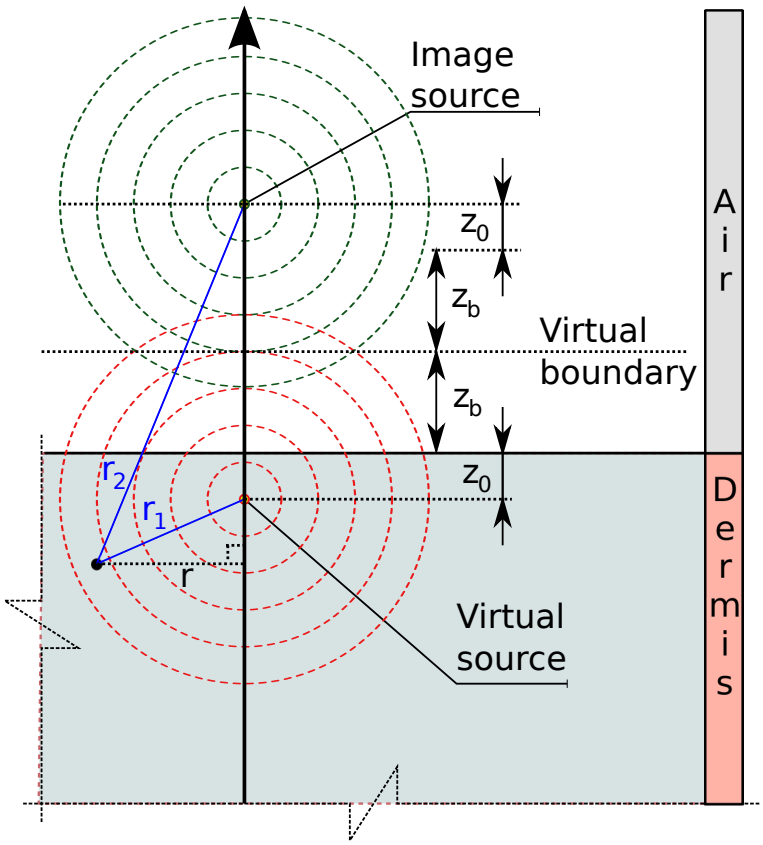

Figure 5. Diffusion model of dermis. The collimated light beam is modelled as an isotropic point source at the depth of mean free path length, z_0 under the skin. The boundary conditions are satisfied by introducing an additional isotropic image source in a symmetric position regarding the virtual skin boundary.

The fluence rate in the semi-infinite medium, shown in Figure 5 is (Farrell *et al.* 1992):

(32) $$F(r,z) = \frac{1}{4\pi D}\left(\frac{e^{-\mu_{\text{eff}} r_1}}{r_1} - \frac{e^{-\mu_{\text{eff}} r_2}}{r_2}\right),$$

where r_2 is the diagonal distance to the image source:

(33) $$r_2 = \sqrt{r^2 + (z + 2z_b + z_0)^2}$$

Reflectance at the skin boundary can be obtained using the derivative of the fluence at the boundary. The equation for the reflectance in radial distance r is given by (Farrell *et al.* 1992):

$$R(r) = \frac{a'}{4\pi}\left[\frac{1}{\mu_t'}\left(\mu_{\text{eff}} + \frac{1}{r_1}\right)\frac{e^{-\mu_{\text{eff}} r_1}}{r_1^2} + \left(\frac{1}{\mu_t'} + 2z_b\right)\left(\mu_{\text{eff}} + \frac{1}{r_2}\right)\frac{e^{-\mu_{\text{eff}} r_2}}{r_2^2}\right], \tag{34}$$

where $a' = \mu_s'/(\mu_a + \mu_s')$ is the transport albedo and $\mu_t' = \mu_a + \mu_s'$ is the total interaction coefficient.

Total reflectance can be obtained by integrating $R(r)$ over the whole surface (Farrell *et al.* 1992):

$$R_d = \frac{1}{2}\left(e^{-\mu_{\text{eff}} z_0} + e^{-\mu_{\text{eff}}(z_0 + 2z_b)}\right) \tag{35}$$

Instead of replacing the collimated laser source by an isotropic point source, it can be more accurately described as follows. The intensity of the beam is attenuated due to absorption and scattering, according to the total interaction coefficient, $I(z) = I_0 e^{-\mu_t z}$. Each scattering event can be interpreted as an origin of a new isotropic point source. The number of scattering events, generated by the interaction of the source beam with the medium, is the reduced scattering coefficient multiplied by the beam intensity:

$$S(z) = I_0 \mu_s' e^{-\mu_t z} \tag{36}$$

By integrating Equation (35) over isotropic light sources, $S(z)$ along z–axis, the total reflectance of the extended light source is obtained (Farrell *et al.* 1992):

$$R_d = \frac{\mu_a'}{2} \cdot \frac{1 + e^{-4/3K \cdot U}}{1 + U} \tag{37}$$

where

$$U = \sqrt{3(1 - \mu_a')} \tag{38}$$

Equations (34) and (37) can be used in estimating the radial or total reflectance of light from a turbid medium, when the optical properties are known. The form of the formulae derived from diffusion theory are intelligible, and the calculation is efficient. However, the assumptions of diffusion approximation may limit the applicability of the results.

2.5 Adding-Doubling method

The adding–doubling method (ADM) was developed by van de Hulst. The method can be used in solving the RTE numerically in arbitrarily thick layered structures, consisting of infinite homogeneous slabs. The method is capable of estimating internal fluence rate, F, reflectance, R, and transmittance, T of a turbid medium. Anisotropic scattering can be included in the form of a phase function as well as boundary conditions for mismatched boundaries, including internal reflections. The method works with any absorption, μ_a, and scattering, μ_s, values and it is said to be relatively fast (Prahl *et al.* 1993). The doubling strategy works iteratively as follows (van de Hulst 1980; Prahl *et al.* 1993):

1. It is first assumed that the slab is homogeneous and very thin, dx, and its optical properties, μ_a, μ_s, and g are known. The reflectance, R, and transmittance, T, can be easily estimated for this very thin slab.
2. Then another identical slab is attached side by side with the first one, essentially forming a slab twice as thick. The combination of the two slabs can be easily solved based on the results of the previous stage.
3. Repeat the two previous steps, until the required thickness is reached.

The adding strategy means that instead of always doubling the existing layer, a layer with different optical properties can be added. Therefore, the adding–doubling also allows the solving of a complex medium consisting of several layers.

2.6 Kubelka-Munk model

Kubelka-Munk theory was originally developed for modelling paint layers (Kubelka & Munk 1931). The theory was later used for modelling skin optics, too (Dawson, Barker, Ellis, Grassam, Cotterill, Fisher & Feather 1980; Claridge, Cotton, Hall & Moncrieff 2002).

A two-flux model describing light transportation in highly scattering media is presented in Figure 6. In the Kubelka-Munk model, the light flux is divided into two parts. Part

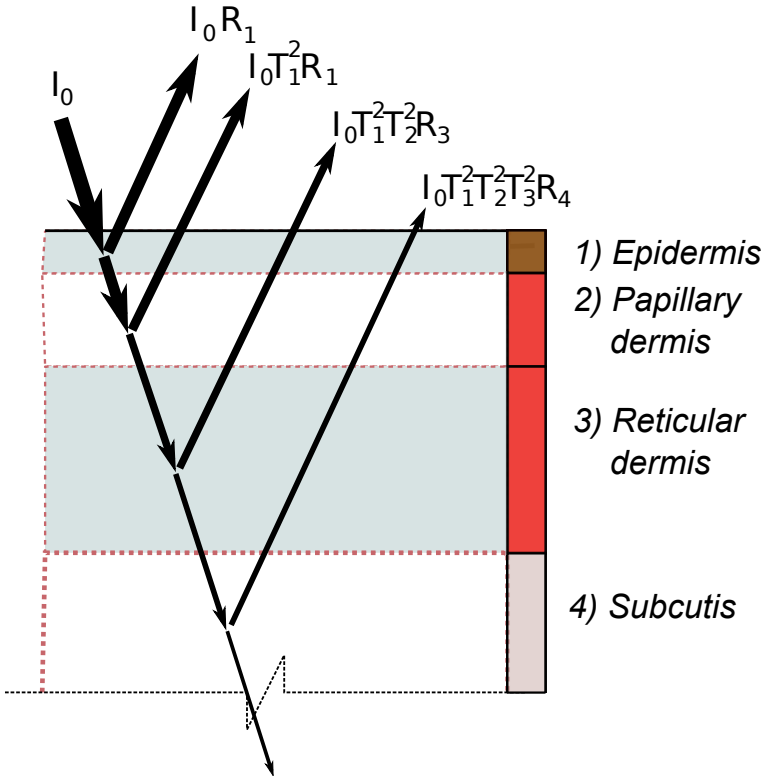

Figure 6. The Kubelka-Munk model of skin.

of the flux is reflected and part of it is transmitted. The reflectance of the incident light, I_0, from the first layer is $I_0 R_1$ and transmittance $I_0 T_1$. The flux transmitted to the second layer is again partly reflected $I_0 T_1 R1$ and partly transmitted to the third layer, $I_0 T_1 T_2$. The reflectance from the second layer needs to be transmitted once again through the first layer. Therefore, the reflectance from the second layer is $I_0 T_1^2 R_1$. The total reflectance from the model is:

$$R_{\text{tot}} = R_1 + T_1^2 R_2 + T_1^2 T_2^2 R_3 + T_1^2 T_2^2 T_3^2 R_4 \tag{39}$$

The two-flux model used in (Claridge *et al.* 2002) is as follows. The reflectance of layer i is:

$$R_i = \frac{(1-\beta^2)(e^{K_m d} - e^{-K_m d})}{(1+\beta)^2 e^{K_m d} - (1-\beta)^2 e^{-K_m d'}} \tag{40}$$

and transmittance:

$$T_i = \frac{4\beta}{(1+\beta)^2 e^{K_m d} - (1-\beta)^2 e^{-K_m d'}} \tag{41}$$

where

(42) $$K_m = \sqrt{k(k+2s)}$$

and

(43) $$\beta = \sqrt{\frac{k}{k+2s}}$$

The thickness of the layer is d, $k \propto \mu_a$ and $s \propto \mu_s$. The model assumes that the incident light is diffuse and the scattering is isotropic. The model can be calculated very fast, but it does not describe the tissue as thoroughly as many other available methods (Tuchin 2007).

The traditional two-flux KM-model was later extended to include phase function and four fluxes (Tuchin, Utz & Yaroslavsky 1994). Even a seven flux model has been used (Yoon, Welch, Motamedi & Gemert 1987).

2.7 Monte Carlo simulation

The principle behind The Monte Carlo method is to estimate a stochastic system by averaging the outputs of the system when a large number of input vectors are randomly sampled from the input space and fed into the system. The result is a probability density function of the system in the range of the selected input variables. The input vectors can be selected uniformly from the whole input space, or the input selection can be weighted. The Monte Carlo method permits the usage of complex and detailed models, while retaining simple implementation. The disadvantages of the Monte Carlo method are noise introduced by the stochasticity and long simulation time when high accuracy is needed.

2.7.1 Monte Carlo Multi Layer

The Monte Carlo Multi Layer (MCML) program was created by Prahl and Jacques and further developed by Wang (Prahl *et al.* 1989; Wang, Jacques & Zheng 1995; Wang & Jacques 1992). The purpose of MCML is to provide a numerical solution to the radiative transfer equation (RTE). Therefore, the MCML simulation does not take into account the interference or other phenomena related to the wave nature of light, any more than the RTE. The MCML program is implemented using ISO C programming language and is available as a public domain.

The MCML program simulates the probability density function of light distribution in skin model consisting of one or more homogeneous layers. Each layer has a definite thickness, but is infinite in other dimensions. The optical properties of the simulated media are assigned for each layer separately. The following properties can be set: relative refraction coefficient, n, absorption coefficient, μ_a, scattering coefficient, μ_s, anisotropy, g, and the thickness of the layer, d.

The light source used in the simulations is an infinitely narrow collimated beam, impinging orthogonally at the air–skin surface. Other light source shapes can be used by convolving the narrow beam over a larger area. A separate program, called CONV, for convolving the result of the MCML simulation over finite light source shapes is also available in the public domain (Wang, Jacques & Zheng 1997).

The program tracks the paths of the photons, using small steps, in a skin model. The skin model in MCML simulation, consists of one or more layers of infinitely wide parallel slabs. The thickness of the i:th layer is d_i, and the layers are assumed to have homogeneous optical properties. To find an optimal step size, enough for precision and long enough for fast simulation, the step size comparable to the mean free path length is selected. The pathlength is obtained using a random variable, ξ, which is uniformly distributed in the range of $\xi \in (0,1)$, as follows (Wang *et al.* 1997):

$$\mathrm{d}l = \frac{-\ln(\xi)}{\mu_t} \tag{44}$$

The range for the step length $\mathrm{d}l \in (0, \mathrm{inf})$, and the mean value of $\mathrm{d}l$ is 1. If $\mathrm{d}l$ is very large, the photon travels through the object without scattering events, representing ballistic photons, but that happens rarely. The average step length coincides with the average mean pathlength, $p_{\mathrm{mf}} = 1/\mu_t$.

To reduce the noise inherent in stochastic simulation, the MCML program follows a path of a package of photons instead of individual photons. The photon package starts moving at speed $\vec{v} = [v_x, v_y, v_z]^T$. The new location $\vec{r}\,'$ of the photon package, located in position $\vec{r}$, after step, $\mathrm{d}l$, is $\vec{r}\,' = \vec{r} + \vec{v}\mathrm{d}l$.

After each step, part of the energy included in the photon package is absorbed and deposited in the current location of the package into the skin model. The amount of absorbed energy is:

$$\Delta E = E\mu_a \mathrm{d}l \tag{45}$$

When the absorption has been counted, the photon package is scattered. The scattering happens to a randomly selected deflection angle, sampled from the probability density function defined by a phase function. The Henyey-Greenstein phase function, shown in Equation (7), is used in the MCML program. The azimuth angle of deflection is sampled from random uniform distribution, between $[0, 2\pi)$.

Should the photon escape from the medium before the step is finished, the step size is temporarily shortened, to stop the photon exactly at the border. Then it is selected, whether the package will be transmitted out of the medium or internally reflected back. The probability of reflection and transmission are obtained from Fresnel's rule, shown in Equation (1). The reflections in the internal boundaries, between the layers with different refraction coefficients, are handled in the same way.

The tracking of each photon package eventually stops when the package is transmitted out of the medium or when the energy of the package is decreased below a threshold, E_{th}, due to absorption. The default threshold value is $E_{\mathrm{th}} = 10^{-4} E_0$.

The main results of the MCML simulation are the reflectance and the transmittance as a function of radial distance from the incident light beam, and the absorption of energy as a function of depth and radial distance.

2.8 Diffusion limit

The ballistic and single scattered photons can be used to acquire spatially localised information from the turbid medium. The multiple scattered or diffused photons have lost directional information, and they cannot be used in localisation of the structure of the medium. Ballistic and single scattered photons can be gated to obtain localised information, but only from the surface in the reflectance setup or from a thin layer in the transmission setup. If the measurement depth or layer thickness is larger than the mean free path length of photons in the medium, the number of single scattered or ballistic photons drop too low to convey enough information any more. Therefore, the depth of the p_{mf} is called diffusion limit. If the medium needs to be probed deeper than the diffusion limit, the diffuse photons are also needed and localisation is poor.

Some methods exist to cope with optical signals deeper than the diffusion limit. One method is optical clearing, in which an optical clearing agent is used to change the optical properties of the medium, to enlarge the p_{mf} of the medium. The optical clearing method does not require any special measurement device. The disadvantage is that optical clearing is not always possible. The clearing agent can only be injected into some media and many clearing agents are toxic, making it difficult to apply in *in vivo* tissue measurements.

Another method is photo-acoustic tomography (PAT). It is based on the photo-acoustic effect, where the light absorbed by the medium results in thermal expansion of the medium. The expansion causes a pressure wave, which can be observed as sound. The origin of the sound source can be located by triangulating with several microphones. The maximum depth and the spatial resolution of PAT can be adjusted, extending the possible application areas. The disadvantages are that PAT technology needs rather complicated measurement devices, and the microphones need to have good acoustic contact with the medium, which may be difficult to arrange in some cases.

If accurate localisation is not needed, diffuse photons can be used, and the target medium can be probed much deeply than p_{mf}. The diffuse spectroscopy and diffuse optical imaging are simple applications of diffuse photons. If time or frequency domain measurement is also included, the diffuse methods can be sensitive to the depth of information, too. Diffuse optical tomography (DOT) is one of those kind of methods. DOT can be used to obtain 3D information about a turbid medium, much deeper than the diffuse limit. However, the localisation is not very accurate in any of the three dimensions.

3 OPTICAL PROPERTIES OF SKIN

The previous section discussed the optical phenomena in turbid media, and methods for modelling them. Light propagation was modelled using general radiative transport theory, which was in turn used in deriving simpler methods for more specific cases. This section introduces how these optical properties affect light propagation and appearance of skin. The reflection spectra of skin chromophores and scattering spectra of skin are presented, at the end of the section.

Skin is the largest human organ; it is easily accessible, and its thickness is suitable for optical examination. Skin disorders, such as skin diseases, injuries, and cutaneous blood circulation regulation change the physical or chemical structure of the skin, changing the scattering or absorption properties, which in turn cause visible changes in the skin color. Many metabolic disorders, bilirubinea for example, can be observed as a skin colour change as well. Optical methods are effective for analysing many skin disorders and other abnormalities.

3.1 Skin structure

Human skin consists of two main layers, *epidermis* and *dermis*. The *epidermis* is the topmost layer of the skin. Its purpose is to protect the skin from various physical and chemical risks, such as mechanical stress and dehydration. The *epidermis* can be further subdivided. The topmost layer of the *epidermis* is the *stratum corneum*, which consists mostly of dead cells, ceratinocytes. The thickness of the *epidermis* varies between 50 μm to several hundreds of micrometers, and typical thickness is somewhere between 100-200 μm (Igarashi, Nishino & Nayar 2007). Optically important characteristics of the *epidermis* are the strong scattering in the air–cell boundaries of the *stratum corneum* and the strong absorption of light of the melanin chromophore contained by the melanocytes. A collimated light beam may become nearly diffuse after transmitted through the *stratum corneum*. The melanin absorbs light strongly, especially UV, blue and green colours. The melanin is the most important chromophore for skin colour. A schematic diagram of the structure of the skin is shown in Figure 7.

The *dermis* is situated immediately underneath the *epidermis*. It is much thicker than the *epidermis*, usually from 1 to 4 mm (Igarashi *et al.* 2007). The main constituents of

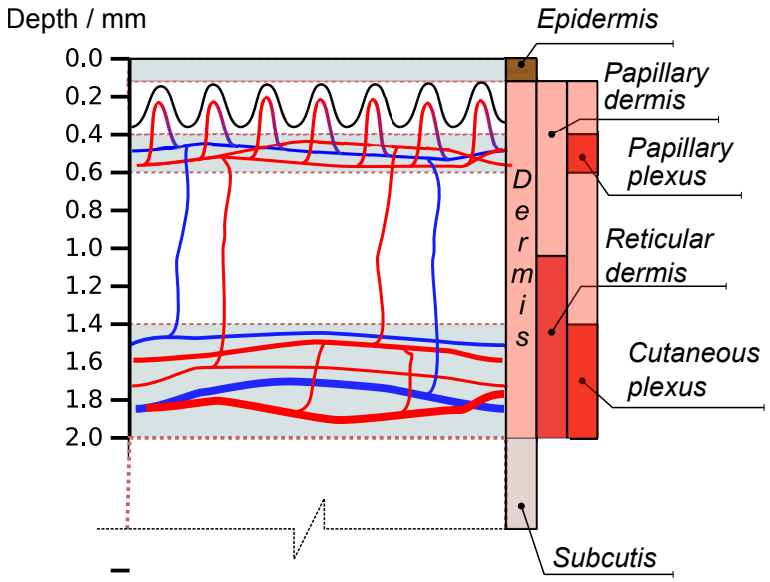

Figure 7. Schematic diagram of skin structure. The layers of the skin are depicted on the right hand side, and the depth is shown on the left.

the *dermis* are collagen and elastin fibers. The dermis contains a lot of arteries and veins as well as capillaries for blood circulation. The microvasculature are concentrated on the top layer of the *dermis*, called *papillary plexus* and the larger vessels are situated in a lower layer, called cutaneous plexus, see Figure 7 (Tuchin *et al.* 1994; Reuss 2005; Igarashi *et al.* 2007). The layer between the *papillary plexus* and *cutaneous plexus* may contain fewer blood vessels. Often the *dermis* is optically modelled only by two layers, the upper part, *papillary dermis* and the lower part *reticular dermis*. The main absorber in the *dermis* is haemoglobin.

The layer beneath the *dermis* is called *subcutis*. It is not counted as part of the skin any more. The structure and thickness of the *subcutis* varies in different body locations and between persons, but often it contains a lot of fat cells to absorb shocks, and its thickness is 4 to 9 mm. The fat cells scatter light strongly and the haemoglobin in the *subcutis* is the most significant absorber.

3.2 Fresnell reflection from skin surface

To protect excessive evaporation of water from the skin, the skin surface contains a thin lipid film. The relative refraction index of this lipid layer is significantly different from that of air. Therefore, incident light is reflected at the air-lipid boundary, making the

skin appear shinier. This specular reflection is only weakly dependent on wavelength. Due to wrinkles and pores, the skin surface is not smooth, and therefore the specular reflection is dispersed and the shine looks unevenly distributed.

3.3 Absorption of skin

The sources of absorption in skin are mainly chromophores dissolved in blood or deposited in tissue, most importantly haemoglobin and melanin. Melanin is the most important factor behind the colour of the skin. It is a deposited in the otherwise weakly absorbing *epidermis*. The absorption spectrum of melanin is measured and a formula for modelling the absorption spectrum is proposed in (Jacques & McAuliffe 1991):

$$\mu_{a,m} = f_m \cdot 1.7 \cdot 10^{12} \cdot \lambda^{-3.48} \quad [1/\mathrm{cm}], \tag{46}$$

where f_m is the relative amount of melanin, the melanin fraction, and, λ, is the wavelength in nanometers. The concentration of melanosomes does not have a direct relationship with absorption, since the size, structure and molar absorption efficiency of melanin may vary. Therefore the melanin fraction is often used instead of the melanin concentration. The absorbtion of melanin, estimated by Equation (46), is shown in Figure 8.

Like the *epidermis*, the *dermis* itself does not absorb much light either, but it contains blood, and the haemoglobin contained in the red blood cells is a strong absorber. It is the iron complex of the haemoglobin molecule, which causes the red colour of blood, by strongly absorbing blue and green. The specific property of haemoglobin is that it can carry oxygen atoms with it. When oxygen atoms are bound with the iron complex of haemoglobin, its absorption spectrum changes. The absorption spectrum of oxyhaemoglobin and deoxyhaemoglobin is determined, for example, in (Horecker 1942) and tabulated by (Prahl 1999). They are shown in Figure 8.

The nominal amount of heamoglobin in blood, hematocrit, is 150 grams/liter. The concentration of haemoglobin in blood, is obtained by dividing the hematocrit with the molar mass of hemoglobin as follows:

$$c_{\mathrm{Hb,blood}} = \frac{150\ \mathrm{g/l}}{64500\ \mathrm{g/mol}} = 2.326\ \mathrm{mol/l} \tag{47}$$

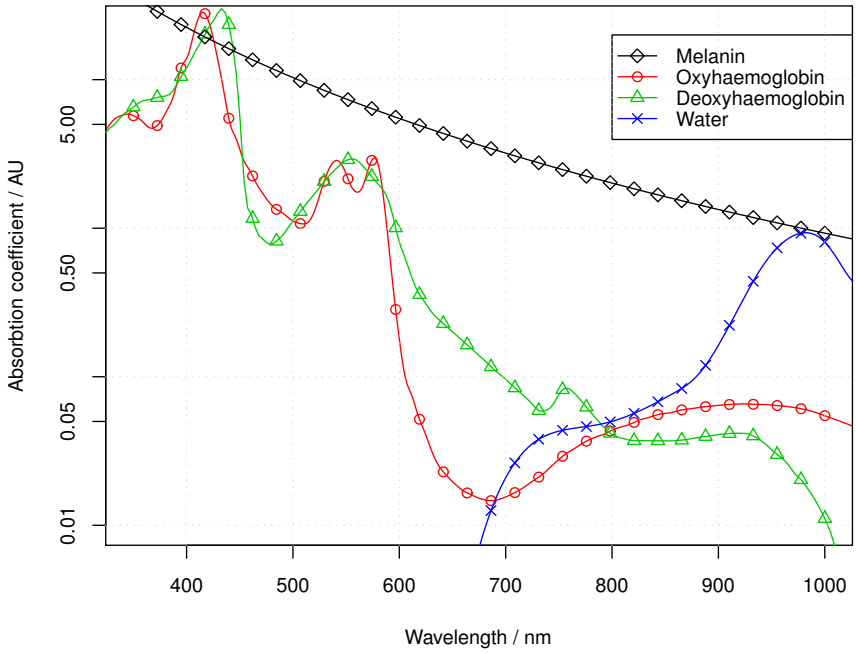

Figure 8. The absorption spectra of the most important skin chromophores: melanin, $\mu_{\mathrm{mel}}(\lambda)$, oxyhaemoglobin, $\mu_{\mathrm{Hbo}}(\lambda)$, deoxyhaemoglobin, $\mu_{\mathrm{Hbd}}(\lambda)$, and water, $\mu_{\mathrm{w}}(\lambda)$. Notice the logarithmic y–axis. (Jacques & McAuliffe 1991; Horecker 1942; Prahl 1999)

The *dermis* contains blood in arteries, veins and capillaries, but not normally outside the blood vessels. Therefore, the blood is not evenly distributed over the whole *dermis*. However, the microcirculation network formed by capillaries is dense, and the reflectance, even from the *papillary plexus*, is an average over a skin area, because it is based on the light beam, which is made diffuse by the strong scattering in the *stratum corneum*. The blood vessel network in the *cutaneous plexus* is coarser, but the reflectance is even more averaged due to additional scattering in the *dermis*. Due to averaging, the blood is often assumed to be evenly distributed inside the whole layer. The average concentration of haemoglobin in skin is the haemoglobin concentration in blood multiplied by the amount of blood in skin, the blood fraction, f_b:

$$c_{\mathrm{Hb,skin}} = f_b \, c_{\mathrm{Hb,blood}} \tag{48}$$

The typical value for f_b in normal skin was 0.05 in (Reuss 2005). We have found lower f_b values in our studies, for example in (Publication III), where $f_b \in [0.0016, 0.0045]$.

The oxygen saturation level of blood, S_{O2}, is defined as the percentage of the oxygenated blood of the total blood concentration:

$$S_{O2} = \frac{c_{\text{Hbo}}}{c_{\text{Hbo}} + c_{\text{Hbd}}} \tag{49}$$

Typical values of oxygen saturation in arteries, $S_{\text{a,O2}} \in [90\%, 99\%]$ and in veins, $S_{\text{v,O2}} > 60\%$.

The absorption spectrum of water is available, for example, in the MiePlot program, measured by Segelstein (Segelstein 1981). The absorption spectrum of water is also shown in Figure 8.

The absorbtion of the skin without blood, the skin baseline, can be simulated, using the following formula (Saidi 1992):

$$\mu_{a,d}(\lambda) = 7.84 \cdot 10^8 \cdot \lambda^{-3.255} \tag{50}$$

The absorption coefficient representing the different layers of skin can be calculated using the known molar extinction coefficients, $\varepsilon(\lambda)$ and the concentrations, as follows:

$$\mu_i(\lambda) = \sum_{j=1}^{N} \varepsilon_{i,j}(\lambda) c_{i,j}, \tag{51}$$

where $\mu_i(\lambda)$ is the absorption coefficient of layer i, $\varepsilon_{i,j}(\lambda)$ is the molar extinction coefficient of chromophore j in layer i, and $c_{i,j}$ is the concentration of the chromophore j in layer i.

For example, the absorption coefficient of the *papillary plexus* can be estimated using following equation:

$$\mu_{a,p}(\lambda) = \mu_{a,d}(\lambda) + \varepsilon_{\text{Hbo}}(\lambda) c_{\text{Hb}} f_{b,p} S_{O2} + \varepsilon_{\text{Hbd}}(\lambda) c_{\text{Hb}} f_{b,p} (1 - S_{O2}) + \varepsilon_{\text{w}}(\lambda) c_{\text{w,p}}, \tag{52}$$

where $\mu_{a,p}(\lambda)$ is the total absorption coefficient of the *papillary plexus*, c_{Hb} is the total concentration of heamoglobin in blood, $f_{b,p}$ is the blood fraction, and $c_{\text{w,p}}$ is the water concentration in the *papillary plexus*.

3.4 Scattering

The human skin is a strong scatterer. The *stratum corneum* in the *epidermis* already makes the light beam diffuse, the collagen and the elastine fibres in the *dermis* scatter light and so do the cytoplasm membranes.

The size of the cells, mitochondrias and collagen fibers are usually larger than 1000 nm, and therefore larger than the wavelength in the diagnostic–therapeutic window. When the scattering particle is close to the wavelength of light, the scattering can be modelled best with Mie scattering (Mie 1908; Tuchin 2007; Igarashi *et al.* 2007; Jacques 1996). The strength of the Mie scattering is roughly proportional to $\lambda^{-1.5}$, where λ is the wavelength of radiation.

The cell nucleus and membranes also scatter light, but they are much smaller than the wavelength. The scattering introduced by these small particles is often described using the Rayleigh scattering formula, which is more strongly wavelength dependent, being proportional to λ^{-4}.

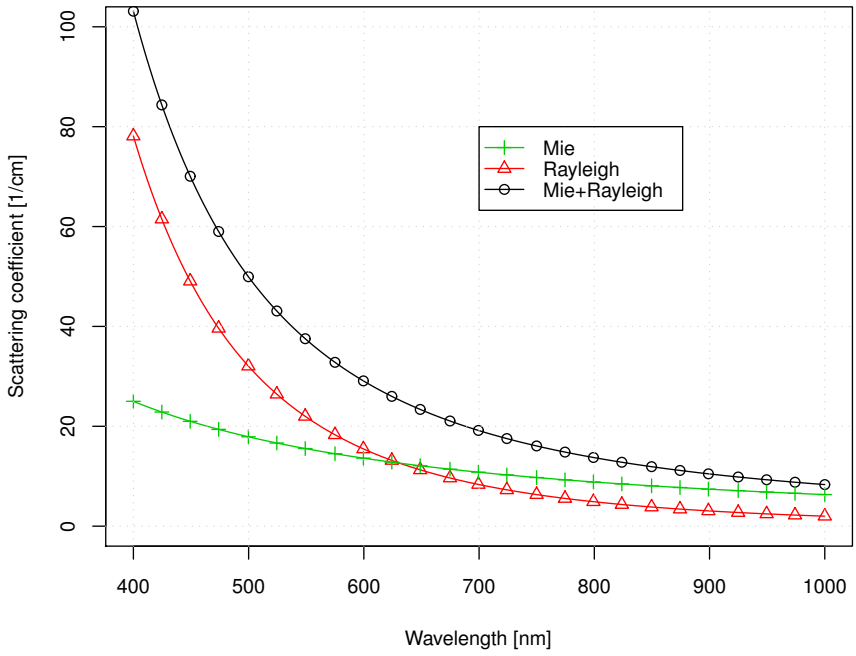

Figure 9. The dependency of scattering on the wavelength: Mie, Rayleigh and both combined, according to Equation (53).

The optical models of skin do not usually work at the individual cell level, because it would be much too complicated to model mathematically and slow to simulate. Instead, the skin layers are assumed to be homogeneous, and the scattering sources are distributed evenly in each layer. The scattering of human skin is often modelled as a combination of Mie and Rayleigh scattering, as follows: (Jacques 1996)

$$\mu_s(\lambda) = \mu_{s,\text{Mie}}(\lambda) + \mu_{s,\text{Rayleigh}}(\lambda) = 2 \cdot 10^5 \cdot \lambda^{-1.5} + 2 \cdot 10^{12} \cdot \lambda^{-4.0}, \tag{53}$$

where the wavelength, λ, is in nanometers.

The Mie and Rayleigh scattering, as well as the combined scattering, are plotted in Figure 9.

3.5 Diagnostic–therapeutic window

In short wavelengths, melanin and haemoglobin absorb light strongly, but their absorption decreases rapidly for red and NIR wavelengths. Conversely, water is transparent at short wavelengths in the UV-VIS range, but absorbs strongly in the NIR range, starting from 950 nm and getting stronger in longer wavelengths. Therefore, the absorption of skin is especially low in red and short wave NIR range. The range where the absorption of both, water and skin chromophores is low is called the diagnostic–therapeutic window. The width and location of the window is not exactly defined. Different research uses different definitions, according to its needs. Usually, the diagnostic–therapeutic window is said to start somewhere from 500 nm to 600 nm and to end somewhere between 950 nm and 1300 nm (Tuchin 2007; Gandjbakhche 2001).

3.6 Other skin chromophores

Melanin, oxyhaemoglobin, and deoxyhaemoglobin are the most important chromophores in skin below 900 nm, while water is the most important above 900 nm. There are still many more chromophores which are also sometimes important.

In addition to oxygen, O_2, carbon dioxide, CO_2, and carbon monoxide, CO, can also bind to haemoglobin, forming carbaminohaemoglobin or carboxyhaemoglobin, HbCO. The absorption spectra of carbaminohaemoglobin or carboxyhaemoglobin is only slightly different from oxyhaemoglobin (Zijlstra, Buursma & van der Meeuwsen 1991; Horecker 1942). Therefore, higher spectral resolution is needed to distinguish whether it is O_2, CO_2 or CO which is bound to haemoglobin. However, this difference may have high clinical significance. The pulse oximeter can reliably measure the oxygen saturation of arteries in normal case, using only two wavelengths. But it may show normal oxygen saturation levels for a patient suffering from carbon monoxide poisoning, because the pulse oximeter may not have enough spectral resolution to distinguish carboxyhaemoglobin from oxyhaemoglobin. Some pulse oximeters use more wavelengths to prevent this kind of error in diagnosis.

Other forms of haemoglobin are methaemoglobin, and haemosiderin. Methaemoglobin is a form of haemoglobin, where the iron in the heme group is in the ferric state Fe^{3+} instead of ferrous state Fe^{2+}. Normally, human blood contains only a small concentration of methaemoglobin. Methaemoglobin cannot transfer oxygen, and it is therefore converted back to haemoglobin using enzymes. The haemosiderin is a degradation product of haemoglobin. The haemosiderin is not usually dissolved in blood, but deposited in tissue, perhaps after hemorrhage, when blood has leaked from the blood vessels to extracellular space. Deposits of methaemoglobin and haemosiderin often exists in bruises (Hughes *et al.* 2004).

Other chromophores of skin, which are sometimes important, are bilirubin (Saidi 1992) and β-carotene. The spectra of bilirubin and β-carotene are available in publicly available PhotochemCAD software (Du, Fuh, Li, Corkan & Lindsey 1998). The absorption peak of bilirubin is around 450 nm, and the full width half maximum (FWHM) bandwidth is about 80 nm. The absorption spectrum of *beta*-carotene is similar to that of bilirubin. Normal bilirubin concentration is about 10 μmol/l (Schwertner, Jackson & Tolan 1994) and β-carotene concentration around $30-50\,\mu$g/l (Wald, Boreham, Hayward & Bulbrook 1984).

4 MEASUREMENT OF SKIN REFLECTANCE

In this section, the existing equipment and theories for measuring the properties of skin are discussed. The principles for measuring the reflectance spectrum of skin are explained first, then methods for solving the optical properties of skin from the measurement data are introduced, and finally, lists of existing technologies and equipment are presented.

4.1 Absorption spectroscopy

When a beam of light is incident into a medium, part of the photons may be absorbed, if their energy is equal to the energy needed to rise the valence electrons or molecules to the higher energy level. This absorption can be seen as an absorption peak in the corresponding absorption spectrum. The absorption peaks in the absorption spectrum can be used in identifying the chemicals or atoms in the substance. NIR spectroscopy is popular in chemistry, since it can be used in identifying certain molecules from the substance. In the VIS-NIR range, the absorption peaks are rather wide and the interpretation of the spectrum easily becomes difficult. Multivariate calibration methods, such as partial least squares regression (PLS) (Geladi & Kowalski 1986) or independent component analysis (ICA) (Tsumura, Ojima, Sato, Shiraishi, Shimizu, Nabeshima, Akazaki, Hori & Miyake 2003) are often used when the concentration of the chemicals needs to be predicted from the spectra. But because the ground truth of concentrations and scattering properties of skin are usually uncertain, multivariate calibration methods may be ineffective. On the other hand, there is a lot of *a-priori* knowledge of the absorption spectra of skin chromophores and the scattering properties of skin itself. Therefore, skin models derived from the radiative transport equation are used more often in solving skin parameters than multivariate calibration methods.

4.1.1 Spectrometer

The absorbtion spectrum is usually studied using a spectrometer, which is also known as a spectroscope, shown in Figure 10. The radiation to be studied is guided into the spectrometer, using, for example, optical fibers. The spectrometer disperses the radiation into a spectrum, using a monochromator, which is often a mirror with diffraction

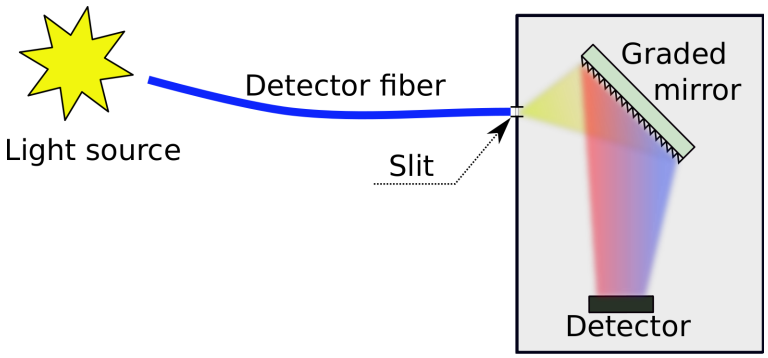

Figure 10. Schematic diagram of spectrometer. The light is guided from the sample or from the light source to the spectrometer using a detector fiber. The light enters into the spectrometer through a narrow slit and is reflected to the detector via a graded mirror, which disperses the light into a spectrum, which is recorded by the detector array.

grating. The diffracted spectrum is led to the detector array, which measures the intensity of the radiation at different wavelengths and transforms it into digital form.

4.2 Spectral imaging

The absorption spectra can also be recorded with an imaging sensor. One grayscale sensor can record the intensity of light, I, in one spectral band, defined by the bandwidths of the light source, $I_0(\lambda)$, and the sensor, $S(\lambda)$. The reflectance of the sample can be obtained by comparing the light intensity reflected from the sample with a light intensity from the white reference. The white reference is usually a special target, the reflectance of which is known, R_w. The reflectance of the sample, R, can be obtained as follows:

$$R = \frac{I_{\text{sample}}}{I_{\text{white}}} R_w = \frac{\int_\lambda I_0(\lambda) S(\lambda) R(\lambda) \mathrm{d}\lambda}{\int_\lambda I_0(\lambda) S(\lambda) R_w \mathrm{d}\lambda} R_w \tag{54}$$

The characteristics of the sensor $S(\lambda)$, and light source, $I_0(\lambda)$ define the bandwidth of the image. One of the following well known methods is usually used in acquiring a spectral image. The first one is to equip the camera with a separate sensor for each channel and to select a different band for each sensor by filters. The second method is to change the band of the light source or the sensors in time, and to acquire several sequential images, one for each band. The third method, called line imagery method, spreads a line of the image into a two dimensional spectrum, and acquires the spectral image line by line.

The most common type of camera able to measure light intensity in multiple bands is the normal tri-stimulus camera, mimicking human colour vision. Tri-stimulus cameras are equipped with separate sensors for each channels. Therefore they can record all channels at once, which makes these cameras fast. The spatial resolution may be high but the spectral resolution is based only on three rather wide bands. Although, the spectral resolution is poor, many kinds of spectral analysis can still be made, as shown in (Publication III) and (Bon, Briand, Guichard, Couturaud, Revol, Servant & Dubertret 2000; Claridge & Preece 2003; Kaartinen *et al.* 2011a; Zhai, Chan, Farahmand, Nilsson & Maibach 2009). Many single point measurement systems also utilise tri-stimulus values for calculating skin erythema and pigmentation (Stamatas, Zmudzka, Kollias & Beer 2004).

Grayscale or tri-stimulus cameras can be extended to a multispectral imaging system by using several narrow-band filters or light sources. The bands are imaged sequentially, one by one. The bands can be narrow, and the central wavelengths can be optimally selected for the application at hand, also outside of the range visible to the human eye. For multispectral skin imaging wavelengths from 400 nm to 1000 nm are the most popular, because they penetrate deep into the skin and can still be detected using normal optics and charge coupled devices (CCD) or complementary metal oxide semiconductor (CMOS) sensors, i.e. silica light sensors. Examples of multispectral skin imagery are depicted in (Publication VI) and (Preece & Claridge 2004). The number of channels can be, for example, between four to ten. A frequently used method is to sample several spectral bands by constructing the light source from light emitting diodes (LED) so that different colour LEDs can be switched on and off separately. Since the bandwidth of the LED is quite narrow, the system can sample several narrow spectral bands.

Advances in sensor technology, computers, and multivariate calibration methods have increased the popularity of hyperspectral imaging. In hyperspectral imagery, the number of spectral bands is large, and they are evenly distributed over the whole operating range of the camera (Randall 2006). The operation of a hyperspectral camera is usually based on either line scanning mode or acquiring each spectral band sequentially, by changing filter characteristics between acquiring the images. In the line imagery mode, the camera spreads one spatial dimension into the 2D image, consisting of one spatial and one spectral dimension. The whole image is acquired by scanning the whole area with the camera. The filtering method is usually implemented with a Liquid Crystal Tunable Filter (LCTF), which is an electronically adjusted band-pass filter. The LCTF

method is used in (Leonardi, Sowa & Payette 2000; Payette, Kohlenberg & Leonardi 2005). The line imagery method may be more accurate in the spectral domain, but it is not used as often as the LCTF method for human skin imaging. Some examples are shown in (Nagaoka, Eikje, Nakamura, Aizawa, Kiyohara, Ichikawa, Yamazaki, Doi, Nakamura, Otsubo & Sota 2007).

Hyperspectral imaging is especially beneficial in research projects, and when the target is not well known. Because all wavelengths are treated equally, the same image acquisition setup fits for many purposes. The disadvantages of the hyperspectral, compared to multispectral imaging, are the relatively long time needed for image acquisition, more complex operation, higher price and higher data storage and transfer needs. The multispectral imaging system often needs be tailored for a specific application, to record only the most important wavelengths. The bands of a multispectral imaging system are also usually wider, which limits the possibility to observe sharp peaks or valleys in the spectra. By optimising the imaging system to acquire only the most important channels, the acquisition time becomes shorter, which reduces movement artefacts, often causing problems when imaging humans or animals.

As explained in Chapter (3), the human skin is after all very well known target. Both scattering and absorption spectra are well known. Therefore, a-priori optimisation of the wavelengths can be made reasonably easily. Therefore, the hyperspectral imaging cannot yet totally replace multispectral imaging in skin analysis.

4.2.1 Illumination

Illumination and probe geometry are important for spectrometer measurements, but the problem is much more challenging in spectral imaging.

Three illumination options are shown in Figure 11. Option a) minimises shadows by placing the light sources as close to the optical axis as possible. Even better would be to illuminate the target through the optical axis, using a beam splitter. Then the light would come exactly from the optical axis, and no shadow could be seen in the image. Option b) tries to minimise specular reflection to the camera, by using oblique incident angle. Baffles may be necessary to prevent light passing directly from the light source to the camera. With reflectors around the light sources option c), increases the intensity of the illumination, since stray light is reflected back to the target. And additional

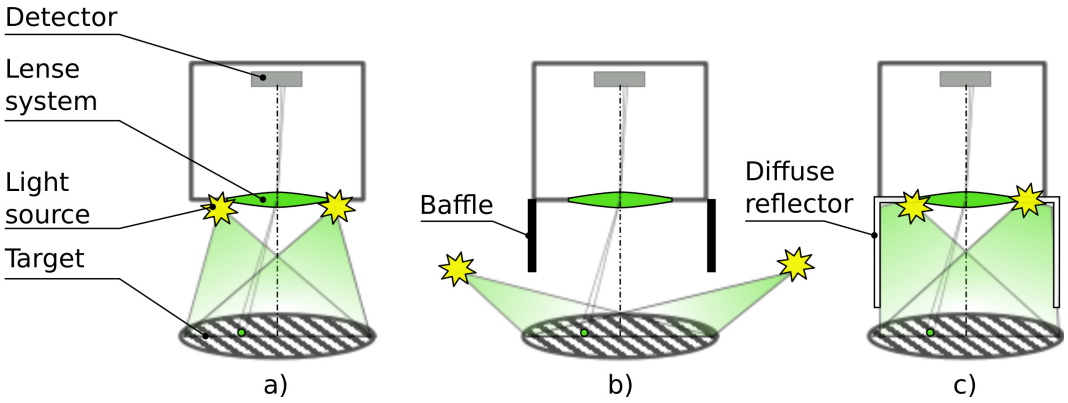

Figure 11. Illumination for spectral imaging. Three options for positioning the illumination sources for imaging are shown. In option a) the light sources are located close to the optical axis to minimise shadows and only direct illumination is accepted. In option b) the light sources are placed far from the optical axis to minimise specular reflection. Baffles may be needed to prevent direct light passing to the lense. In option c) the illumination is amplified by using diffuse reflectors.

advantage of reflectors is that the light field will be smoother, since the light is coming more uniformly.

When designing the illumination for the spectral camera, the following objectives need to be considered. The light field should be uniform, the formation of shadows should be minimised and the specular reflections should also be minimised. These objectives may be mutually exclusive, since surface roughness causes shadows if the illumination angle is too oblique, and an oblique angle would be needed to guide specular reflectance out of the lens. It may be easier to prevent shadows than specular reflectance with the illumination geometry, since the roughness of the skin would scatter the specular reflection to all directions notwithstanding the incident angle of the light. Therefore, illumination geometry a) may often be better than b). Option c) increases the illumination, but the disadvantage is the formation of partial shadows, because part of the light is coming in an oblique angle, far from the optical axis. The second disadvantage is the interreflectance between the target, R, and the reflector, r. As a consequence, the observed reflectance, R', is non-linearly dependent on the real reflectance of the target. But this can be easily compensated mathematically as follows (Publication V):

$$R = \frac{R'}{1 - r + rR'} \tag{55}$$

Therefore, if partial shadows are not the problem, c) is a better option than a). If the intensity suffices, a) is a better option than c). The small nonuniformity of the light

field is not usually a big problem, since it will be compensated in calibration, as shown in Equation (54).

4.3 Probes

4.3.1 Integrating sphere

Integrating sphere (IS) can be used in averaging the remittance over a large solid angle or providing diffuse light to the target, over a large angle. The remittance collection method is shown in Figure 12, where the integrating sphere integrates the remitted light over a hemisphere. In case a), IS is used in measuring the transmittance of the sample, and in case b), the IS is used in measuring the reflectance. If the sample is turbid and inhomogeneous or its surface is rough, the remittance can be different in different angles, while the average transmittance or reflectance are still quite stable. The remittance measurement of one angle only would be much more sensitive to inhomogeneousness and surface roughness than the measurement integrated over the whole hemisphere.

When an IS is used for illumination, a light source is installed in place of a detector in Figure 12 a), the sample will be illuminated evenly with diffuse light. The benefit of diffuse illumination is that the shadow formation due to surface roughness is cancelled, and the specular reflection is equal regardless of the orientation of the elements of the surface.

The integrating sphere can also present some challenges. In turbid media, the incident beam of light diffuses in every direction, spreading the beam radially. Therefore, the remittance from the sample, both in transmission and in reflectance measurements, can extend to a larger area than the hole in the integrating sphere. In this case, part of the remittance is lost behind the edge of the sphere. These edge losses are especially difficult in spectroscopic measurements, since different wavelengths may suffer differently from the edge losses. For example, when measuring human skin, a significant amount of red light is often lost, but the remittance in green may be mostly collected. The compensation of the edge loss was studied in (Publication VI) with MCML simulation. It was assumed in the simulation that skin is illuminated with a collimated beam, of radius $r_b = 0.15$ cm, and the remittance is collected with an integrating spere, which aperture radius $r_a = 0.5$ cm. The results of the simulation are shown in Figure 13.

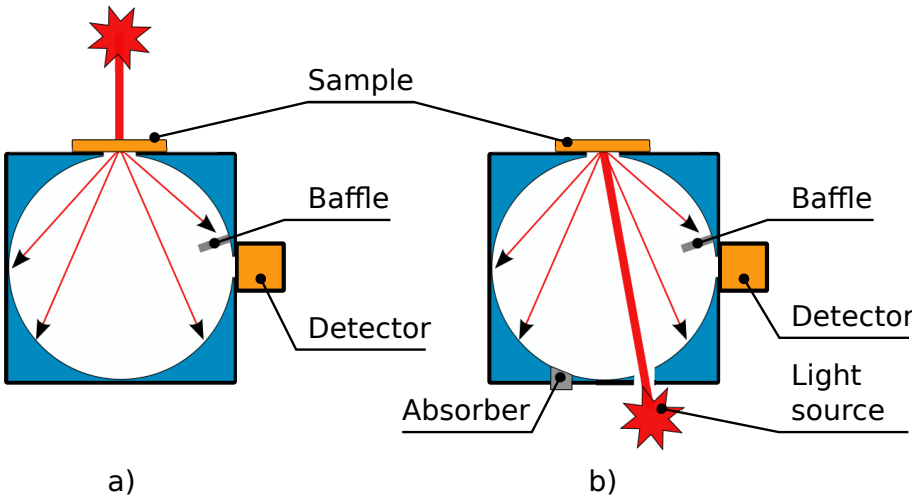

Figure 12. Integrating sphere: A beam of light comes either through a sample a) or reflects from the sample b). A baffle is needed to prevent direct transmittance or reflectance from the sample to be detected and additional absorber can be used in reflectance measurements to cancel specular reflectance.

In case of normal skin reflectance, the edge losses were compensated using following detector efficacy factor:

$$\eta(\lambda) = \begin{cases} 1 & \text{if } \lambda \leq \lambda_t \\ E_L + (1 - E_L) e^{k(\lambda_t - \lambda)} & \text{if } \lambda > \lambda_t, \end{cases} \tag{56}$$

where $E_L \in [0,1]$ is an edge loss coefficient, describing the maximum detection efficacy in the NIR range and k is an experimental constant. For simulated skin parameters and given integrating sphere geometry $E_L = 0.7$ and $k = 0.02$. The proposed compensation method depends on both the properties of the particular integrating sphere and the absorption spectra of the target. Therefore the edge loss compensation needs to be adjusted in each case separately.

Another challenge introduced by an integrating sphere is interreflectance, described in (Publication V). The compensation method is shown by Equation (55). The problem of interreflection can be sometimes solved also by carefully designed measurement configurations, as shown in (SphereOptics LLC 2007).

Often the reflection measurements of turbid media are improved by gating away the specular reflections and single scattered photons with cross polarising filters. This is usually rather impossible for integrating sphere measurements using reflectance setup, because the incident light is fed through the same hole than the remitted light, and the polarisation is mixed in the integrating sphere, too.

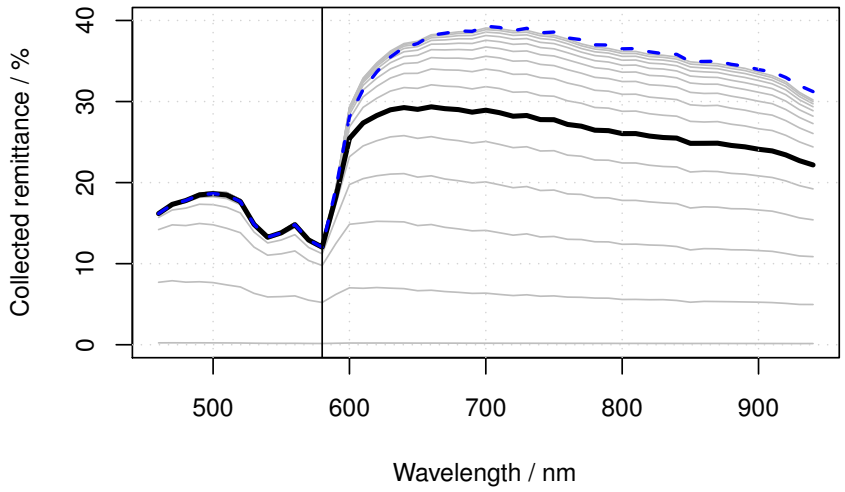

Figure 13. Edge loss model of an integrating sphere: The thin gray lines show the collected reflectance as a function of wavelength, when the aperture radius, r_a of the integrating sphere is increased from 0 cm (bottom) to 1.5 cm (top) with the steps of 0.1 cm. The thick solid line represents the simulated reflectance spectrum when $r_a = 0.5$ cm. The thick dashed line shows the previous spectrum compensated, when $E_L = 0.71$.

4.3.2 Plain fibers

Plain fibers are often used for both illumination and detection. The benefits of the plain fiber probe include both mathematical and manufacturing simplicity. Furthermore, sharply localised incident light makes it possible to examine the spatial distribution of the light field. For example, Equation (34) predicts the reflectance of a turbid medium, from a distance, r, from the narrow collimated incident beam. This formula can be used together with the measured spatial distribution of light to estimate both the reflectance and the absorption coefficients of the medium. Often, the challenge when measuring turbid media is to reach deep enough. The average information depth of the two-fiber probe can be controlled by adjusting the distance of the fibers (Publication I).

4.3.3 Other probe geometries

Many other kinds of probes are often used. Sometimes the illumination fiber is replaced with a coherent laser beam, or focused incoherent light beam. The average measurement depth can be further increased using a circular light source and measuring the reflectance in the center (Publication I), as shown in Figure 15.

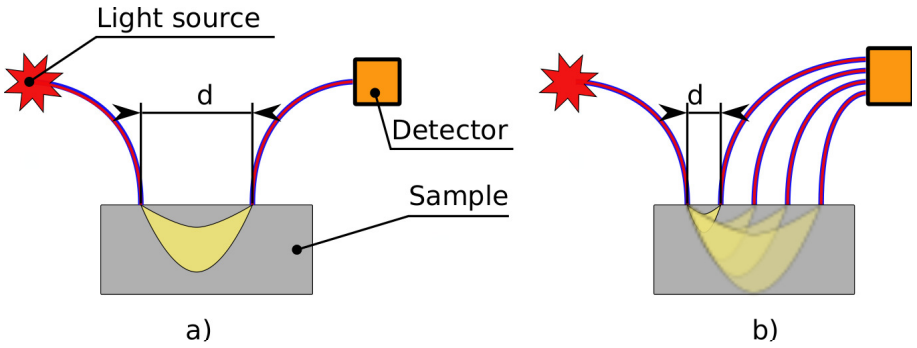

Figure 14. Plain fiber probe with one detector a) and several detectors b). The illumination is provided by a fiber from the light source and the reflectance from one point of skin is detected by one or more fibers and guided to the spectrometer. The average information depth can be controlled by the distance, *d*, between the fibers.

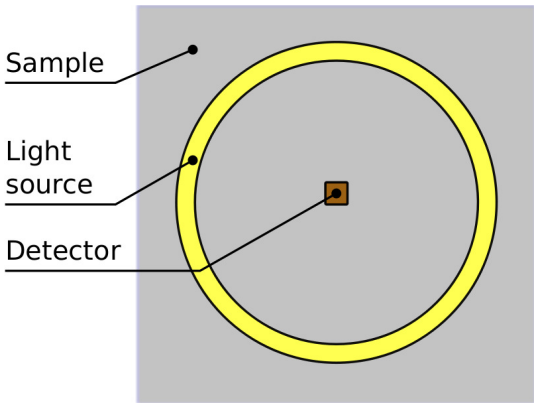

Figure 15. Ring shaped probe can measure deeper than the plain fiber probe.

4.4 Solving clinical chromophore indices

The goal when studying skin optics is often to find out clinically significant parameters about the conditions of the skin, the clinical chromophore indices, such as pigmentation index (PI) and erythema index (EI). These parameters may be the actual concentrations or sometimes artificial variables either linearly or non-linearly related to the actual concentrations, melanin and haemoglobin. General strategies for solving the clinical chromophore indices are shown in Figure 16.

Various light transport models of skin make it possible to estimate the reflectance of skin when the optical properties are known. But usually, reflectance is straightforward to measure and it is the optical properties, which are unknown, that need to be estimated. Because skin, and therefore also the models, are non-linear, they cannot be

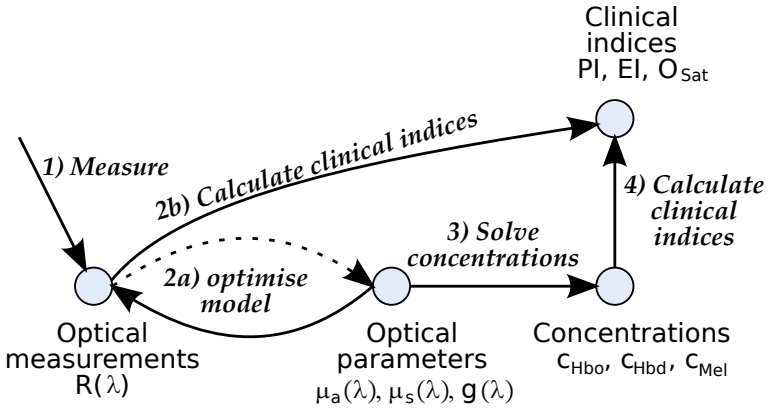

Figure 16. Schematic diagram of strategies to solve the clinically significant chromophore indices: In phase 1), the reflectance spectra is measured. 2a) the optical properties of the skin are searched by fitting a skin model to the spectra. 3) The concentrations of the chromophores are solved from the optical properties. 4) The given clinical indices are calculated from the concentrations. Sometimes chromophore indices are calculated directly from the shapes of the reflectance or absorption spectra 2b).

easily inverted. Therefore, the optical properties are often searched iteratively, using an optimisation method, through the parameter space, until the reflectance predicted by the model fits to the measured reflectance spectrum. Some widespread optimisation methods are linear least squares, Levenberg-Marquardt and genetic algorithms.

4.4.1 Linear least squares

Linear least squares (LLS) is a method for fitting a linear model to the statistical data. A linear model for predicting the dependent variable y from predictor variables x_i can be expressed as:

$$\hat{y}_i = \sum_{j=1}^{N} \beta_j x_{i,j} \tag{57}$$

The goal for optimisation is to find optimal values for coefficients β_j to minimise the squared error:

$$E = \sum_{i=1}^{M} (y_i - \hat{y}_i)^2 \tag{58}$$

The linear least squares problem can be solved in closed form. The solution is well known:

$$\beta = (\mathbf{X}^T\mathbf{X})^{-1}\mathbf{X}^T\mathbf{y} \tag{59}$$

The least squares optimisation method is implemented in most linear algebra packages and suitable libraries are available, including LAPACK (Anderson, Bai & Bischof 1999). Often the LLS problem is solved using orthogonal decomposition of $\mathbf{X}$, for example QR- or Singular Value Decomposition (SVD).

4.4.2 Levenberg-Marquardt

No general closed form optimisation method is known for fitting a non-linear least squares (NLS) model. Therefore, the methods for NLS are iterative and thus much slower than LLS methods. One popular iterative method for the fitting of a non-linear model is the Levenberg-Marquardt method (LMA) (Moré 1978).

The Levenberg-Marquardt method uses both the steepest descent and Gauss-Newton methods. When the solution is still far away, the algorithm behaves like the steepest descent, which is slow, but guaranteed to converge. Close to the solution, the algorithm behaves like the Gauss-Newton method, which converges faster (Lourakis 2005). The Gauss-Newton method is similar to Newton's method, but it does not require the computation of the second derivatives, and it can only be used for minimising the sum of squares.

LMA implementation for many programming languages and computing platforms is available in the LEVMAR library (Lourakis Jul. 2004) and MINPACK library (Moré, Garbow & Hillstrom 1980).

4.4.3 Genetic algorithm

Genetic algorithms (GA) are evolutionary algorithms often used for optimisation of complex systems (Goldberg 1989; Alander 1992). GAs require neither computation of derivatives, nor continuous fitness space. They can be used for very many kinds of optimisation problems. In case the fitness space contains several local optima in addition to the global optimum, the GA is more likely to find the global optimum than LLS or NLS methods. The expense is a much longer computation time.

Instead of using matrix operations or derivatives, GAs use methods inspired by biological evolution, such as inheritance, mutation, selection, and crossover. Genetic algorithms are explained in (Whitley 1994). An overview of the optimisation phases used by genetic algorithm are shown in Figure (17).

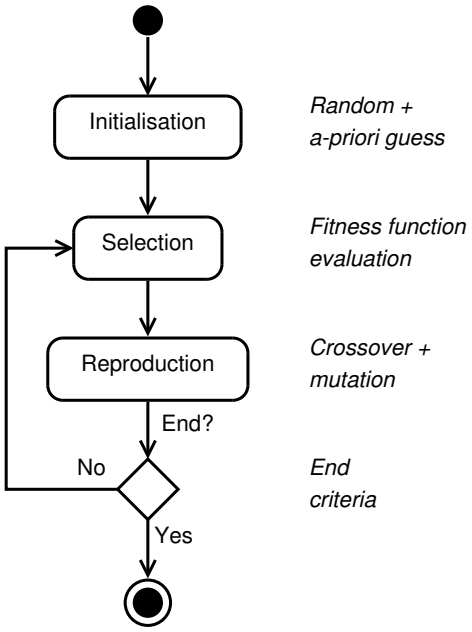

Figure 17. The steps of Genetic Algorithm. GA starts with the initialisation of the population using random individuals and possibly utilising a-priori knowledge of the problem domain. Then the population is breed in selection–reproduction loop until the end criterion is reached. In selection phase, the individuals which are the best according to the fitness function evaluation are selected for reproduction step. The new population consists of the results of crossover and mutation of the selected parents.

Genetic algorithms start with a population of solution candidates. The population consists of N individuals. Each individual contains the model parameters, β_j, encoded often as a sequence of bits. The initial population is often sampled at least partly randomly from the parameter space. A priori information can be utilised by including individuals with presumably good genes in the initial population.

The initial population is breed towards higher fitness population by population, by iterating selection and reproduction steps. To select the best individuals of the population, the fitness of each individual is evaluated using a fitness function, which can be arbitrary. The sum of squares function, shown in Equation (58) is a common choice. Having evaluated the fitness of the individuals, the optimisation proceeds to the reproduction step. When reproducing a new population, few best individuals are preserved

as such, if elitism is used. All high fitness individuals take part in the reproduction process, which uses crossover and mutation operators in producing the next generation which is supposed to share most of the properties of the best individuals of the parent population. The mutation randomly changes one or more individual genes of the target individual and the crossover composes a new child from the blocks of genes of two parents.

Each population explores part of the parameter space often much more effectively than random search, according to the so called building block hypothesis introduced by (Goldberg 1989) also described in (Whitley 1994). Most of the individuals tend to converge towards global and local optima, generation by generation. The mutations help GAs not to stick to the local optima.

4.5 Direct methods

Some clinical indices are calculated directly from the spectra, without calculating the optical parameters first. The benefit of these methods is that they can be calculated in closed form, thus no iteration is needed. Examples of directly calculated clinical indices are shown in the following list:

- Correlation coefficient index (CC_{index}) (Clancy *et al.* 2010) Linear to the change compared to the normal image.
- Tissue Viability Index ($TiVi_{index}$). (O'Doherty, Henricson, Anderson, Leahy, Nilsson & Sjöberg 2007)
- CIEL*a*b* colour coordinates, Minolta Chromameter (Clarys, Alewaeters, Lambrecht & Barel 2000), chromophore mapping (Jung, Choi, Durkin, Kelly & Nelson 2004)
- Mexameter estimates erythema and pigmentation indices, calculated from the reflectance of three narrow channels (Clarys *et al.* 2000),
- DermaSpectrometer also estimates erythema and pigmentation indices, but only from the reflectance of two channels (Clarys *et al.* 2000),
- The PI and EI indices are estimated from three narrow channels by EMM-01 device (Dolotov, Sinichkin, Tuchin, Utz, Altshuler & Yaroslavsky 2004),

The disadvantages of these methods are that the model has to be rather simple and the theoretical background may not always be as sound as for those methods using more sophisticated models.

4.6 Light transport model based methods

Skin reflectance model based methods are more general. They concentrate on modelling the reflectance of skin as accurately as possible when the optical properties of skin are known. The reflectance of the skin depends non-linearly on the optical properties of the skin, thus most of the models are also non-linear. Sometimes the Beer-Lambert model is used for approximating the relationship between skin reflectance and optical parameters. In this case the model is linear. Some examples of the reflectance models are listed below:

- MCML model, optimised using MATLAB optimisation toolbox (Tsumura, Kawabuchi, Hideaki Haneishi & Miyake 2000)
- Kubelka-Munk model, inverted with lookup table (Claridge *et al.* 2002)
- Beer-Lambert model, an homogeneous, closed form used in the assesment of cutaneus haemodynamics (Sowa, Matas, Schattka & Mantsch 2002) and imaging of burn injuries (Leonardi *et al.* 2000)
- Spectrocutometry, a hybrid model, using diffusion theory and differential BLL (Publication III; Publication IV; Publication VI) and (Kaartinen *et al.* 2011a)

4.7 Differential pathlength spectroscopy

Absorption spectroscopy and Beer-Lambert law are used regularly for estimating chemical concentrations from samples without scattering. The Beer-Lambert law assumes that the change in absorbance is caused by the change in concentration only, and the pathlength stays constant. The problem in turbid media is that the average pathlength of the photons is affected by changes in both the scattering and the absorption coefficient. Stronger scattering makes the path of the photons more curvy and the higher absorption increases the probability that the photons travelling a long path in the medium will be

absorbed (Publication VI), (Reif, Wang, Joshi, A'Amar & Bigio 2007; Mourant, Johnson, Los & Bigio 1999). Nevertheless, some means are available to use the BLL also for turbid media.

Mourant *et al.* used one fiber to illuminate skin and another fiber for collecting the reflectance signal from the skin to the spectrometer (Mourant *et al.* 1999). They noticed that if the distance, d, between the illumination and detecting fiber is in the range of [1.5, 2.2] mm, the pathlength does not significantly depend on the scattering coefficient for the typical values of skin, where $\mu_s' \in [5, 15]$ 1/cm. They modelled the effect of μ_a on the pathlength, L, as follows:

$$L(\mu_a) = x_0 + x_1 e^{-x_2 \mu_a}, \tag{60}$$

where x_i are calibration coefficients which depend on the probe geometry. Therefore, the Beer-Lambert law could be used for estimating μ_a, if the probe consists of illumination and detecting fibers separated by a distance of 1.5–2.2 mm and Equation (60) is used instead of assuming constant pathlength. However, in this case the BLL modified like this is not linear any more, and the solution of μ_a based on measurements requires a nonlinear optimisation method.

Amelink *et al.* , in turn, improved the method developed by Mourant by introducing a special probe involving two detector fibers. One is the illumination fiber itself (dc) and the second is placed close to the illumination fiber (c). Instead of using the two reflectance signals separately, their difference is calculated. This difference signal is the following (Amelink & Sterenborg 2004):

$$R_{\mathrm{dc}}(\lambda) - R_{\mathrm{c}}(\lambda) = C \mu_s'(\lambda) e^{-\tau \mu_a(\lambda)}, \tag{61}$$

where $R_{\mathrm{dc}}(\lambda)$ is the reflectance from the delivery–collection fiber, $R_{\mathrm{c}}(\lambda)$ is the reflectance from the collection only fiber, C is a calibration constant, and $\tau = 0.8\, d_{\mathrm{fiber}}$ is the apparent differential pathlength, which only depends on the fiber diameter d_{fiber}. This differential pathlength spectroscopy allows using a BLL, which is only corrected by a term related to scattering. If the scattering is constant, μ_a can be solved using LSS.

4.8 SIAscopy

Spectrophotometric Intracutaneous Analysis (SIA) is an optical method for studying pigmented lesions or diagnosing melanoma (Moncrieff, Cotton, Claridge & Hall 2002). SIAScopy can be used in measuring the total melanin, epidermal melanin, haemoglobin, and collagen content of skin. The SIAscope measures an area of 24×24 mm or smaller using visible and near infrared (NIR) light in the range of $\lambda \in [400, 1000]$ nm.

The prediction of skin chromophores is based on the Kubelka-Munk model (Claridge & Preece 2003), which is one of the most often used methods for approximating the Radiative Transfer Equation (RTE). The model can be used in calculating the reflectance spectra for given chromophore concentrations. The prediction can be made by searching through the parameter space, until the generated spectra match with the measured spectra. The SIAscope samples the reflectance spectra by acquiring several narrow band images of skin. For each pixel, the corresponding parameters of skin are searched, until the model produces a spectrum, which matches the spectral data of the images (Claridge *et al.* 2002).

(Claridge & Preece 2003) searched for an optimal filter set for SIAscopy by means of Genetic Algorithm (GA). The centre wavelengths of the optimal filters were 485 nm, 560 nm and 700 nm and the bandwidths (FWHM) correspondingly 24, 14, and 95 nm. The average prediction error for melanin varied between 5% and 17%, depending on the melanin concentration and correspondingly the average prediction error for blood varied from 9% to 16% depending on the blood concentration.

The new version of the SIAscope uses eight spectral channels (Moncrieff *et al.* 2002). The prediction accuracy is not reported, but it could be better, because more spectral information is used. The prediction in both cases is based on pre-calculated values in a look-up table.

The benefits of SIAscopy in melanoma diagnostics remains controversial (Govindan, Smith, Knowles, Harvey, Townsend & Kenealy 2007; Terstappen, Larko & Wennberg 2007).

4.9 TiVi imaging

Tissue Viability imaging (TiVi) is a method for making chromophore maps of skin. The purpose of the TiVi imaging system is to measure the concentration of red blood cells (RBC) in tissue. The measurement depth of the imaging system is about 300 μm (O'Doherty *et al.* 2007). Instead of using calibrated narrow band images, the TiVi system uses a ratio of red and green colour channels, and therefore it is not sensitive to the intensity of the illumination as long as the balance of red and green of the light source stays constant. The TiVi system uses a flash light, which is assumed to be much brighter than any ambient light, and therefore ambient light has only a small effect on the results (Nilsson, Zhai, Chan, Farahmand & Maibach 2009). Since the spectrum of the flash light is known, no calibration is needed in normal use. The TiVi imaging system consists of cross polarisers to block specular reflections and single scattered photons to improve contrast for the deeper layers of skin.

The calculation of the RBC index, called Tissue Viability index ($\mathrm{TiVi}_{\mathrm{index}}$), is based on the following equation (McNamara, O'Doherty, O'Connell, Fitzgerald, Anderson, Nilsson & Leahy 2010):

$$M_{\mathrm{out}} = K \cdot e^{-p \cdot K}, \tag{62}$$

where

$$K = G_1 \frac{M_{\mathrm{red}} - G_2 M_{\mathrm{green}}}{M_{\mathrm{red}}} \tag{63}$$

The output value, M_{out} of Equation (62) is the ($\mathrm{TiVi}_{\mathrm{index}}$). The purpose of the empirical constant p, is to calibrate the system to produce correct $\mathrm{TiVi}_{\mathrm{index}}$ values. Similarly G_1 and G_2 are calibration constants. The value for $G_2 = 0.9905$ was calculated from the tissue properties and the value for $p = 2.6$ is selected by empirical measurements to achieve the best linearity (O'Doherty *et al.* 2007). The speed and resolution of the TiVi imaging system depends on the capabilities of the camera. For example, 15 images per second at a resolution of 1024 times 768 is possible (McNamara *et al.* 2010). The processing of the images is done off-line, after the recording of data.

4.10 Point-wise chromophore index estimation

Devices capable of measuring the reflectance of the skin from one location are available, too. They measure either the colour of the reflected light as tri-stimulus values, or specific index-values, such as the pigmentation index (PI) or erythema index (EI).

The Chromameter CR 200 (Minolta) measures the tri-stimulus reflectance values of a target, such as human skin, illuminated with a wideband xenon arc lamp. The reflectance values provided by the Chromameter are based on the average reflectance from a circular area, of diameter about 8 mm. The tri-stimulus values are converted to the CIE L*a*b* coordinates. The a* parameter is found to correlate with erythema whereas the luminance parameter, L, and the b* parameter correlate with pigmentation. (Clarys *et al.* 2000)

The Mexameter MX-16 (Courage-Khazaka) is a device specifically made for measuring the melanin index, MI, and the erythema index, EI. The light source consists of twelve LEDs, whose wavelengths are $\lambda_g = 568$ nm, $\lambda_r = 660$ nm, $\lambda_{nir} = 880$ nm. The device measures the reflectance of the skin from a circular area, having a diameter of about 5 mm. (Clarys *et al.* 2000)

The DermaSpectrometer (Cortex Technology) uses only two wavelengths, $\lambda_g = 568$ nm and $\lambda_g = 655$ nm. The device measures the reclectance from skin, averaging a circular area, the diameter of which is about 6 mm. (Clarys *et al.* 2000)

The EMM-01 is a new device for estimating the pigmentation and melanin indices. It uses twelve LEDs for illumination and one photodiode for detection. The wavelengths of the LEDs are $\lambda_g = 560$ nm, $\lambda_r = 650$ nm, and $\lambda_{nir} = 710$ nm. The placing of the illumination LEDs and the detector is designed to reject specular reflections. The erythema and pigmentation indices are calculated as follows:

$$M = k \cdot \frac{A(\lambda_r) - A(\lambda_{nir})}{\lambda_{nir} - \lambda_r} \tag{64}$$

$$E = 100 \left(A(\lambda_g) - A(\lambda_r) - \frac{M}{k}(\lambda_r - \lambda_g) \right), \tag{65}$$

where M is the pigmentation index, E is the erythema index and $A(\lambda)$ is absorption. (Dolotov *et al.* 2004)

5 SPECTROCUTOMETRY

In this section, two prototypes of the Spectrocutometer hardware are introduced. The light transport models and algorithms for solving the optical properties of the tissues and for calculating clinical indices is explained. Finally, the section presents two clinical studies made using the Spectrocutometer prototypes to asses the healing of wounds and the properties of matured scars. The description of the studies shows how the digital planimetry, and chromophore mapping would work in practise, how the acquired clinical parameters relate to current medical practises, and what is the clinical significance of these measurements. The second study includes also some statistical analysis to find out which scar parameters have highest clinical value, and how do these different properties depend on each other.

5.1 Spectrocutometer prototype

Several pilot studies have been already made to study how the digital planimetry and chromophore mapping would work in practise. For these studies, a prototype of the hardware of the Spectrocutometry was needed. A schematic diagram of the second generation prototype is shown in Figure 18.

The main part of the prototype is the protecting dome, which has tree purposes 1) to act as a support where the camera and the lighting unit are connected, 2) to protect the target from ambient light, 3) to keep the angle and the distance of the camera standard for all images.

The protection for ambient light is essential because it allows the calibration of the system by imaging a known target, usually a white reference. When the image of the actual target is acquired, the spectral characteristics of the camera and the light source and the inevitably uneven light field are compensated as shown in Equation (54). The digital camera in this prototype is Canon Powershot G5 (Canon Inc, Tokyo, Japan), which is modified by removing the IR-cut filter from the sensor in order to extend the range of the camera to NIR-range. The illumination unit consist of 72 moderate power surface mounted LEDs with large illumination angles. The center wavelengths of the LEDs are 468, 520, 639, and 939 nm and bandwidths (FWHM) are correspondingly 33, 39, 19, and 81 nm. The diameter of the support unit is 83 mm, and the distance between the illumination unit and the target is 40 mm.

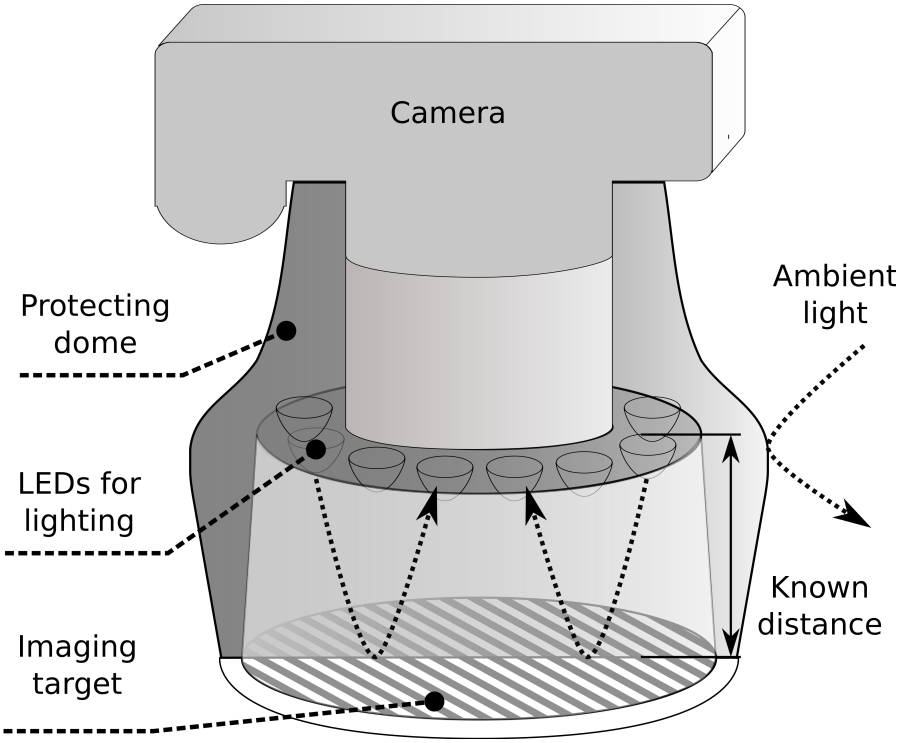

Figure 18. Prototype of the hardware of the Spectrocutometer: The central part of the prototype is the protecting dome, which both protects the target from ambient light and acts as a support for camera and the lighting system keeping the imaging distance and angle constant for every shot. The lighting system consists of LED:s and a control unit, which is not shown in the figure.

The third prototype is based on a digital single lens reflex camera (DSLR), Fuji IS Pro (Fujifilm corporation,Tokyo, Japan), which is already capable of imaging through UV-VIS-NIR range as far as approximately 1000 nm. In this case the protecting dome has the shape of a cuboid of height 13 cm, width 13 cm, and length 20 cm. The size of the imaged area is thus 20x13 cm. The illumination is similar to that of the cylinder shaped prototype. This prototype is shown in Figure 19. The illumination is more even in this prototype than in the previous prototype but the light comes further away from the optical axis and shadow formation is stronger.

In both cases the images are transferred from the camera to the computer in raw format to retain the full resolution of the sensor, which is 14 bits/colour in Fuji and 12 bits/-colour in Canon. The calibration and other image processing was calculated in 16-bit format to avoid rounding errors. The accuracy of the reflectance measurements using Spectrocutometry prototype is comparable to the accuracy of a spectrometer, using integrating sphere (Publication V). In both cases, the specular reflections are somewhat disturbing, and in the future the cross-polarising filters are planned to be used as explained in Subsection (2.1.5).

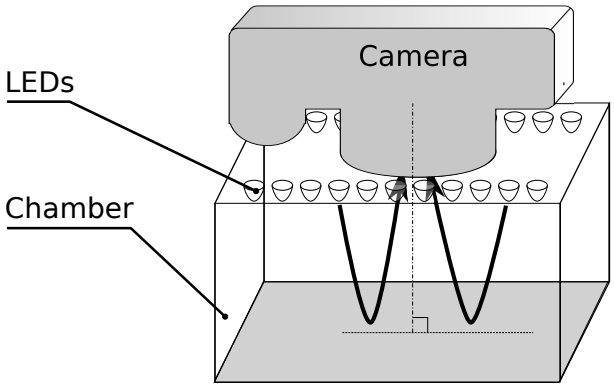

Figure 19. The third prototype of the hardware of the Spectrocutometer: The protecting dome is now cuboid shape, and the imaged area is larger.

5.2 Methods

The Spectrocutometer hardware and related algorithms were tested in pilot studies. The first pilot was used to only test the blood prediction methods using standard spectrometer hardware. The next two pilots were done using the Spectrocutometer prototype in a hospital environment.

5.2.1 Blood concentration modelling using MCML model

The prediction of blood concentration with MCML simulation model was tested using an Allen's test (Asif & Sarkar 2007) for altering the blood volume of palm. The reflectance spectra from the palm was measured after occluding the arterials in the wrist and pumping the blood off the blood vessels using hand muscles. Then the arterials were released, and the spectra was measured all the time without moving the probe. In this way, the estimation of the blood volume in skin could be tested. The measurements were made using HR4000 spectrometer and ISP-REF integrating sphere (Ocean Optics Inc, Dunedin, Florida, USA). The estimation was made by fitting and MCML simulation model to the measured spectra (Publication III). The model was first optimised using genetic algorithm, as shown in (Publication II), and then by changing the blood concentration manually.

5.2.2 Melanin, blood, and oxygen saturation

The chromophore mapping was tested in the skin graft donor site study, where the clinical goal was to evaluate the healing of wounds (Kaartinen *et al.* 2011a). In this study,

the skin graft donor sites were imaged after 14, 30 and 90 days after surgery, using the third prototype of the Spectrocutometer. The Spectrocutometer was calibrated regularly to compensate for the drifting of the light source characteristics. The images of the skin were segmented manually to the skin disorder area and normal skin. The median reflectance of the normal skin was converted to absorption and used as a reference. The absorption in each pixel in the skin disorder area was compared with the absorption of the normal skin. This absorption difference was assumed to be due to pigmentation and vascularisation together, and the share of each was solved from the following equation:

$$\Delta A(\lambda) = A_{\delta \mathrm{Hb}}(\lambda)\, \Delta c_{\mathrm{Hb}} + A_{\delta \mathrm{mel}}(\lambda) \Delta c_{\mathrm{mel}}, \tag{66}$$

where $\Delta A(\lambda)$ is the measured absorption change, and $A_{\delta \mathrm{Hb}}(\lambda)$ is the simulated absorption change when the haemoglobin concentration change is δ_{Hb}, and the $A_{\delta \mathrm{mel}}(\lambda)$ is the simulated absorbtion change when the melanin concentration change is δ_{mel}. The concentration changes Δc_{Hb} and Δc_{mel} can be solved if the absorption change is measured in at least two wavelengths, and the absorption changes due to melanin and haemoglobin are linearly independent. In the pilot study, the measurements were made using three bands, defined by red, green, and blue LEDs. The overdetermined system was solved using LLS according to Equation (59).

According to the pilot, the Spectrocutometer values correlate with the values estimated by a set of human observers. But it proved to be difficult to subjectively estimate whether two areas of the wound, treated with different methods, had different vascularisation or not, if the areas were examined separately. The Spectrocutometer was better in observing changes both in between differently treated areas and in terms of time.

The estimation method shown in Equation (66) is linear, because nonlinear methods are not usually fast enough for predicting chromophore concentrations in high resolution image. The proposed method was later improved by using derivatives $\partial A/\partial c_{\mathrm{Hbo}}$, $\partial A/\partial c_{\mathrm{Hbd}}$, and $\partial A/\partial c_{\mathrm{mel}}$ instead of the differences. Mathematically, the model can now be expressed as a first order Taylor series of $A(\lambda)$. The required derivatives can be obtained by numerically differentiating the MCML simulation results, but it is a rather slow method. Therefore, the MCML model was replaced with a hybrid model, consisting of a diffusion theory model of the dermis and Beer-Lambert model of the epidermis, shown in Figure 20. The Beer-Lambert law in Equation (20), and the diffu-

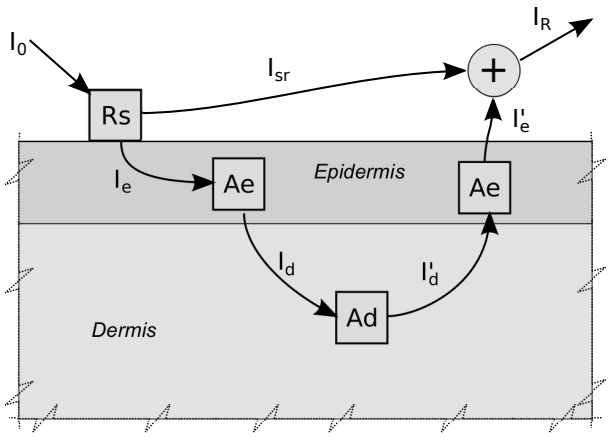

Figure 20. Diffusion theory based dermis model extended by a Beer-Lambert model of the epidermis: part of the incident light I_0 is reflected from the surface. The rest, I_e, is transported through the epidermis and partly absorbed. The remaining part, I_d, is partly absorbed, partly transmitted and partly reflected, I'_d. The reflectance from the dermis is partly absorbed in the epidermis again. The remaining part, I'_e is added to the specularly reflected light, I_{sr}, to obtain the total reflectance, I_R.

sion approximation of reflectance shown in Equation (37) can be analytically differentiated (Publication VI). The intensity of the reflectance from the hybrid model can be calculated step by step, as follows:

$$I_e = I_0(1 - Rs) \tag{67}$$

$$I_d = I_e / e^{A_e} \tag{68}$$

$$I'_d = I_d / e^{A_d} \tag{69}$$

$$I'_e = I'_d / e^{A_e} \tag{70}$$

$$I_{sr} = I_0 R_s \tag{71}$$

$$I_R = I_{sr} + I'_e \tag{72}$$

The differential of the diffusion model of the dermis by the absorption coefficient is (Publication VI):

$$\frac{\partial A_d}{\partial \mu_a} = \frac{z_0}{2(U+1)} \left(2(U+1) + \frac{3 z_0 \mu'_s}{U} + \frac{4K z_0 \mu'_s (U+1) e^{-4/3KU}}{U(e^{-4/3KU}+1)} \right) \tag{73}$$

where U and K are shown in Equations (38) and (30).

The differential of the Beer-Lambert model of the epidermis is (Publication VI):

$$\frac{\partial A_e}{\partial \mu_a} = p_e, \tag{74}$$

where p_e is the average pathlength of the photons in the epidermis. Because the epidermis is thin, the pathlength is assumed to be independent on absorption.

The absorption difference between given locations of the skin can now be formulated using Taylor series expansion:

$$\Delta A = \frac{\partial}{\partial \mu_a} A \cdot (\Delta \mu_{a,b} + \Delta \mu_{a,d}) + 2\, p_e \Delta \mu_{a,e}, \tag{75}$$

where $\mu_{a,e}$, $\mu_{a,d}$, and $\mu_{a,b}$ are the absorption coefficients of the epidermis, dermis and skin baseline.

By using these analytical derivatives, the solution for the optical properties of skin can be found orders of magnitude faster than using nonlinear least squares optimisation methods, making it possible to resolve the chromophore maps of high resolution multispectral images in reasonable time (Publication VI, Table 2). The accuracy of the method suffers from linearisation, but it can be minimised by selecting the operating point for linearisation inside the range of optical properties in the given image. The method used here is to adapt the hybrid skin model to the observed spectra once, using the nonlinear least squares method. The Levenberg Marquardt algorithm can find the model parameters, the chromophore concentrations in a few iterations. When the model is adapted, for example to the absorption of normal skin, the analytical derivatives are calculated, and the chromophore concentration estimation for other pixels can be calculated fast, by solving Equation (75) using LLS.

5.2.3 Segmentation of foreign objects

In a scar assessment pilot study (Publication IV) the scar images contained mostly normal skin, the scar itself and other skin disorders, mostly melanocytic nevi. The scar was close to the centre of the image. The image areas near the borders contained more often disturbing shadows or foreign objects, such as clothes.

The median colour of the pixels near the centre of the image was used as a rough estimate of the normal skin colour, R_n, of the image. The centre area was defined by a larger elliptic mask covering 56% of the image or a smaller elliptic mask covering

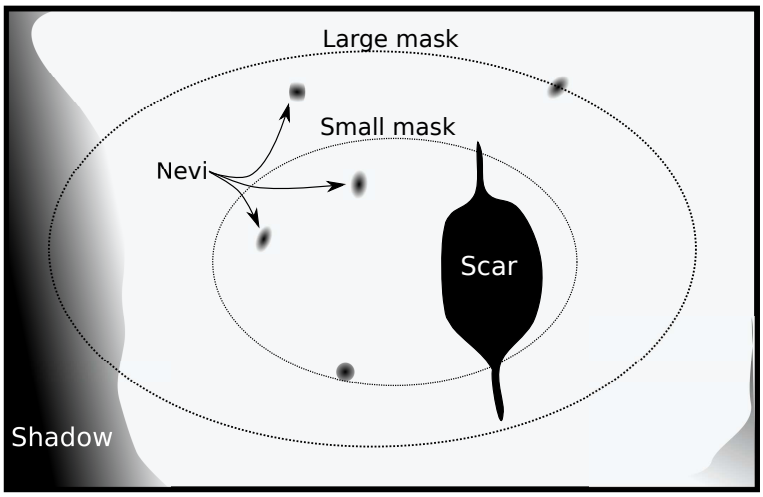

Figure 21. An example of typical scar image and masking: the scar is near the middle, and shadows on the left side and lower right corner. Several melanocytic nevi are scattered randomly. In this case, the larger mask was used, since it covers a larger percentage of normal skin than the smaller mask.

20% of the image. The larger mask was used whenever possible, and the smaller one for those images where shadows and other artefacts prevented using the larger mask, see Figure 21. This rough segmentation provides an acceptable estimate of the normal skin colour on average, but may fail in some images. Therefore, the normal skin colour average over all patients was used instead of individual averages as a starting point.

It was assumed that the differences in normal skin absorption between samples are due to changes in pigmentation and haemoglobin concentrations alone. Therefore, the absorption of each pixel can be constructed from normal skin absorption by increasing or decreasing the amount of chromophores in the corresponding skin model. The model was fitted to the absorbance and the residual of the solution is the difference between the measured absorbance and the absorbance given by the fitted model.

The colour of each pixel is classified as skin if ΔC_b, ΔC_m and the residual are small; otherwise, the pixel is assumed to be skin disorder, foreign object, shadow, etc. This obtained healthy skin area is used for estimating the average normal skin absorption in the given image.

5.2.4 Scar assessment

The scar area was segmented manually from the image by selecting the skin area surrounding the scar, where the colours of the pixels were significantly different than in

normal skin. If visual examination revealed other probable causes for colour change, they were excluded from the scar area.

The concentration model was again fitted to the absorption of the pixel, but this time the normal skin estimate of the individual image was used. The medians of ΔC_b and ΔC_m were calculated over the whole scar area to summarise the level of vascularisation and pigmentation of the scar.

The obtained vascularisation and pigmentation ind were then compared with the subjective estimation and the symptoms observed by the patient. The Pearson and Spearman correlation coefficients were used for estimating linear and nonlinear, but monotonic, dependencies. An easily understandable graphical dependency model, a Bayesian network, was also built from both the objective and subjective variables. It was found that the pliability, thickness, and measured vascularisation are the most important parameters in analysing these kinds of well matured linear scars. The vascularisation can be measured accurately using a Spectrocutometer and assessment of pigmentation was not meaninfull at all in case of linear scars. Therefore human observer can be replaced by Spectrocutometer in colour-based assesments. The possibilities in measuring the pliability and thickness of the scar will be studied in the future.

6 CONCLUSION

The objective of the thesis was to study methods for measuring skin disorders optically. In Publication I, it was found that the probe design affects the depth of the measurement results. In general, the longer the distance is between emitter and detector fibers, the deeper is the measurement. But later it became evident that it is important to compare the absorption of the skin disorder with the absorption of normal skin, because the absorption difference is sensitive to local changes only, rejecting the effect of global changes. The local changes are related to the skin disorder itself, and global changes to the metabolism and physical exercise of the person. By using multispectral imaging and segmentation, the comparison of healthy skin and skin disorder is straightforward; in addition, colour images of the disorder can be obtained from the spectral image, e.g. for documentation purposes. Furthermore, when imaging the whole skin disorder, the influence of the operator is minimised, since the measurement location is not chosen by the operator. Therefore, spectral imaging was considered to be a clinically better approach than point wise measurements.

In Publication II, it was shown that increasing the spectral resolution improves the accuracy of the estimation only to a certain limit, consequently multispectral imaging with proper bands is as good as hyperspectral imaging for predicting blood and melanin concentrations. Unfortunately, the probe and illumination geometries cannot be optimised as freely as those for point wise systems, thus excluding some recent, otherwise promising, measurement setups, such as differential pathlength spectroscopy. The benefit of differential pathlength spectroscopy is that the clinical skin parameters can be solved in closed form, whereas with other methods iterative nonlinear least squares methods are usually needed. These iterative methods are too slow in practice to be applied for high resolution multispectral images.

A prototype for multispectral diffuse reflectance imaging system, the Spectroctutometer, suitable for clinical use, was built. The accuracy of reflectance measurement of the Spectrocutometer was tested in Publication V, and the measurements were found to be only slightly more inaccurate than those obtained using a spectrometer. The imaging system uses selected wavelengths in the therapeutic-diagnostic window, and is calibrated in the spectral domain and normalised in the spatial domain. The operation of the imaging system was tested in a clinical pilot study, explained in Publication IV.

To estimate local melanin and haemoglobin concentration changes, as well as oxygen saturation difference from a multispectral image, a new approach was taken, which is based on the corresponding difference in the absorption spectra. The absorption change spectra is projected into an oblique coordinate system, where each axis corresponds to the apparent absorption of a particular skin chromophore. In this way, the absorption change can be mapped to the changes of individual chromophore concentrations. The axes of the coordinate system were obtained by simulating the apparent absorption change when only the concentration of one chromophore changes. The simulations were performed using the MCML simulation model and validated by *in vivo* measurements for blood in Publication III. The measured absorption difference spectrum was then constructed as a linear combination of these difference spectra of individual chromophores. The linear approximation is accurate only when the concentration changes are small, therefore it is important to select the reference concentration values so that the differences are as small as possible. The method was validated by applying it in two clinical pilots, one of them shown in Publication IV.

The developed chromophore mapping method was further improved in Publication VI, by replacing the MCML skin model with a hybrid model, consisting of a Beer-Lambert model of the *epidermis* and diffusion model of the *dermis*. The benefit of this model is that analytical differentials of absorption by absorption coefficients of the *dermis* and *epidermis* can be obtained. The more flexible model makes it easy to fit the model to each image to be analysed, to find the optimal reference value for linearisation, and the use of differentials makes the model mathematically more sound and it is also easier to adapt the model to new estimation tasks.

In the future, more work is needed in choosing optimal wavelengths for estimating the blood and melanin concentrations and oxygen saturations to further improve the prediction accuracy. The effect of scattering change should be modelled in the same way as absorption is handled now. A proper calibration method when using cross-polarising filters needs to be studied as well. A new pilot is planned to test whether the usability of the Spectrocutometer can be improved by designing it smaller and wireless. More research is needed to find out whether the method is also suitable for other kinds of wounds than those studied so far.

BIBLIOGRAPHY

Alander, J. T. (1992). On optimal population size of genetic algorithms. In P. Dewilde & J. Vandewalle (Eds.), *CompEuro 1992 Proceedings, Computer Systems and Software Engineering, 6th Annual European Computer Conference*. IEEE Computer Society, The Hague: IEEE Computer Society Press, 65–70.

Amelink, A. & Sterenborg, H. (2004). Measurement of the local optical properties of turbid media by differential path-length spectroscopy. *Applied Optics* 43: 15, 3048–3054.

Anderson, E., Bai, Z. & Bischof, C. (1999). *LAPACK Users' guide*. Society for Industrial Mathematics.

Asif, M. & Sarkar, P. K. (2007). Three-digit Allen's test. *The Annals of Thoracic Surgery* 84, 686–7.

Baranoski, G. V. G. & Krishnaswamy, A. (2008). Light interaction with human skin: from believable images to predictable models. In *SIGGRAPH Asia '08: ACM SIGGRAPH ASIA 2008 Courses*. New York, NY, USA: ACM, 1–80.

Baryza, M. & Baryza, G. (1995). The Vancouver Scar Scale: an administration tool and its interrater reliability. *Journal of Burn Care & Research* 16: 5, 535.

Beitner, H. (1988). Immediate pigment-darkening reaction. *Photodermatology* 5: 2, 96.

Bochko, V., Välisuo, P., Harju, T. & Alander, J. (2010). Lower extremity ulcer image segmentation of visual and near-infrared imagery. *Skin Research and Technology* 16: 2, 190–197.

Bon, F.-X., Briand, E., Guichard, S., Couturaud, B., Revol, M., Servant, J.-M. & Dubertret, L. (2000). Quantitative and kinetic evolution of wound healing through image analysis. *IEEE Transactions on Medical Imaging* 19: 7, 767–772.

Chandrasekhar, S. (1960). *Radiative Transfer*. Dover Pubns.

Changizi, M., Zhang, Q. & Shimojo, S. (2006). Bare skin, blood and the evolution of primate colour vision. *Biology Letters* 2, 217–221.

Cheong, W., Prahl, S. & Welch, A. (1990). A review of the optical properties of biological tissues. *IEEE Journal of Quantum Electronics* 26: 12, 2166–2185.

CIE (1931). *Commission internationale de l'Eclairage proceedings*. Cambridge, UK: Cambridge University Press.

Clancy, N., Nilsson, G., Anderson, C. & Leahy, M. (2010). A new device for assessing changes in skin viscoelasticity using indentation and optical measurement. *Skin Research and Technology* 16: 2, 210–228.

Claridge, E., Cotton, S., Hall, P. & Moncrieff, M. (2002). From colour to tissue histology: Physics based interpretation of images of pigmented skin lesions. In T. Dohi & R. Kikinis (Eds.), *Medical Image Computing and Computer-Assisted Intervention — MICCAI 2002*, vol. 2488 of *Lecture Notes in Computer Science*. Berlin, Germany: Springer Berlin / Heidelberg, 730–738.

Claridge, E. & Preece, S. (2003). An inverse method for the recovery of tissue parameters from colour images. In *Information Processing in Medical Imaging*, vol. 2732. Ambleside, UK: Springer, 306–317.

Clarys, P., Alewaeters, K., Lambrecht, R. & Barel, A. (2000). Skin color measurements: comparison between three instruments: the Chromameter®, the DermaSpectrometer® and the Mexameter®. *Skin Research and Technology* 6: 4, 230–238.

Dawson, J. B., Barker, D. J., Ellis, D. J., Grassam, E., Cotterill, J. A., Fisher, G. W. & Feather, J. W. (1980). A theoretical and experimental study of light absorbtion and scattering by *in vivo* skin. *Physics in Medicine and Biology* 25: 4, 695–709.

Dolotov, L., Sinichkin, Y., Tuchin, V., Utz, S., Altshuler, G. & Yaroslavsky, I. (2004). Design and evaluation of a novel portable erythema-melanin-meter. *Lasers in Surgery and Medicine* 34: 2, 127–135.

Draaijers, L., Tempelman, F., Botman, Y., Tuinebreijer, W., Middelkoop, E., Kreis, R. & van Zuijlen, P. (2004). The patient and observer scar assessment scale: a reliable and feasible tool for scar evaluation. *Plastic and Reconstructive Surgery* 113, 1960–1965.

Du, H., Fuh, R. A., Li, J., Corkan, A. L. & Lindsey, J. S. (1998). Photochemcad: A computer-aided design and research tool in photochemistry. *Photochemistry and Photobiology* 68: 2, 141–142.

Ebner, M. (2007). *Color constancy*. West Sussex, UK: Wiley.

Farrell, T., Patterson, M. & Wilson, B. (1992). A diffusion theory model of spatially resolved, steady-state diffuse reflectance for the noninvasive determination of tissue optical properties *in vivo*. *Medical Physics* 19: 4, 879–888.

Gandjbakhche, A. (2001). Diffuse optical imaging and spectroscopy, *in vivo*. *Comptes Rendus de l'Académie des Sciences-Series IV-Physics* 2: 8, 1073–1089.

Geladi, P. & Kowalski, B. (1986). Partial least-squares regression: a tutorial. *Analytica Chimica Acta* 185, 1–17.

van Gemert, M. J. C., Jacques, S. L., Sterenborg, H. J. C. M. & Star, W. M. (1989). Skin optics. *IEEE Transactions on Biomedical Engineering* 36: 12.

Goldberg, D. E. (1989). *Genetic Algorithms in Search Optimization & Machine Learning*. Addison Wesley.

Govindan, K., Smith, J., Knowles, L., Harvey, A., Townsend, P. & Kenealy, J. (2007). Assessment of nurse-led screening of pigmented lesions using SIAscope. *Journal of Plastic, Reconstructive & Aesthetic Surgery* 60: 6, 639.

Hecht, E. & Zajac, A. (1974). *Optics (Addison-Wesley Series in Physics)*. Addison-Wesley Pub. Co.

Hietanen, H., Iivanainen, A., Seppänen, S. & Juutilainen, V. (2002). *Haava*. Helsinki: WSOY, 3 edn..

Horecker, B. L. (1942). The absorbtion spectra of hemoglobin and its derivatives in the visible and near infra-red regions. *The Journal of Biological Chemistry* 148: 1, 173–183.

Hughes, V., Ellis, P., Burt, T. & Langlois, N. (2004). The practical application of reflectance spectrophotometry for the demonstration of haemoglobin and its degradation in bruises. *British Medical Journal* 57: 4, 355.

Igarashi, T., Nishino, K. & Nayar, S. (2007). The appearance of human skin: A survey. *Foundations and Trends in Computer Graphics and Vision* 3: 1, 1–95.

Ishimaru, A. (1977). Theory and application of wave propagation and scattering in random media. *Proceedings of the IEEE* 65: 7, 1030 – 1061.

Jacques, S., Alter, C. & Prahl, S. (1987). Angular dependence of HeNe laser light scattering by human dermis. *Lasers in the Life Sciences* 1: 4, 309–333.

Jacques, S. L. (1996). Origins of tissue optical properties in the UVA, Visible, and NIR regions. *Advances in Optical Imaging and Photon Migration* 2, 364–369.

Jacques, S. L. & McAuliffe, D. J. (1991). The melanosome: threshold temperature for explosive vaporization and internal absorption coefficient during pulsed laser irradiation. *Photochemistry and Photobiology* 53, 769–775.

Joseph, J., Wiscombe, W. & Weinman, J. (1976). The delta-Eddington approximation for radiative flux transfer. *Journal of the Atmospheric Sciences* 33: 12, 2452–2459.

Jung, B., Choi, B., Durkin, A., Kelly, K. & Nelson, J. (2004). Characterization of port wine stain skin erythema and melanin content using cross-polarized diffuse reflectance imaging. *Lasers in Surgery and Medicine* 34: 2, 174–181.

Kaartinen, I. S., Välisuo, P. O., Alander, J. T. & Kuokkanen, H. O. (2011a). Objective scar assessment–a new method using standardized digital imaging and spectral modelling. *Burns* 37: 1, 74–81.

Kaartinen, I. S., Välisuo, P. O., Bochko, V., Alander, J. T. & Kuokkanen, H. O. (2011b). How to Assess Scar Hypertrophy? A Comparison of Subjective Scales and Spectrocutometry – A New Objective Method. *Wound Repair and Regeneration* 19: 2.

Kubelka, P. & Munk, F. (1931). An article on optics of paint layers. *Zeitschrift für technische Physik* 12, 593–601.

Leonardi, L., Sowa, M. G. & Payette, J. R. (2000). Near-infrared spectroscopy and imaging: A new approach to assess burn injuries. *American Clinical Laboratory* , 20–22.

Lourakis, M. (2005). A brief description of the Levenberg-Marquardt algorithm implemented by levmar. *Matrix* 3, 2.

Lourakis, M. (Jul. 2004). levmar: Levenberg-marquardt nonlinear least squares algorithms in C/C++. [web page] `http://www.ics.forth.gr/~lourakis/levmar/`. [Accessed on 31 Jan. 2005.].

McNamara, P., O'Doherty, J., O'Connell, M., Fitzgerald, B., Anderson, C., Nilsson, G. & Leahy, M. (2010). Tissue viability (TiVi) imaging: utility in assessment of rapid changes in the cutaneous microvasculature. In V. V. Tuchin, D. D. Duncan & K. V. Larin (Eds.), *Dynamics and Fluctuations in Biomedical Photonics VII*, vol. 7563. Bellingham, WA, USA: SPIE.

Mie, G. (1908). Beiträge zur Optik trüber Medien, speziell kolloidaler Metallösungen. *Annalen der Physik* 330: 3, 377–445.

Moncrieff, M., Cotton, S., Claridge, E. & Hall, P. (2002). Spectrophotometric intracutaneous analysis: a new technique for imaging pigmented skin lesions. *British Journal of Dermatology* 146: 3, 448–457.

Moré, J. (1978). The Levenberg-Marquardt algorithm: implementation and theory. *Numerical Analysis* , 105–116.

Moré, J., Garbow, B. & Hillstrom, K. (1980). User guide for MINPACK-1. Tech. Rep., Argonne National Laboratory, Illinois, USA.

Mourant, J., Johnson, T., Los, G. & Bigio, I. (1999). Non-invasive measurement of chemotherapy drug concentrations in tissue: preliminary demonstrations of *in vivo* measurements. *Physics in Medicine and Biology* 44, 1397.

Nagaoka, T., Eikje, N., Nakamura, A., Aizawa, K., Kiyohara, Y., Ichikawa, F., Yamazaki, T., Doi, M., Nakamura, K., Otsubo, S. & Sota, T. (2007). Inspection of skin hemodynamics with hyperspectral camera. In *Engineering in Medicine and Biology Society, 2007. EMBS 2007. 29th Annual International Conference of the IEEE*. IEEE, 3357 –3361.

National Institute for Health and Welfare (2009). *Statistical Yearbook on Social Welfare and Health Care*. Helsinki, Finland.

Nilsson, G., Zhai, H., Chan, H., Farahmand, S. & Maibach, H. (2009). Cutaneous bioengineering instrumentation standardization: the Tissue Viability Imager. *Skin Research and Technology* 15: 1, 6–13.

O'Doherty, J., Henricson, J., Anderson, C., Leahy, M., Nilsson, G. & Sjöberg, F. (2007). Sub-epidermal imaging using polarized light spectroscopy for assessment of skin microcirculation. *Skin Research and Technology* 13: 4, 472–484.

Ostermeyer, M. (1999). *Light Transport in Inhomogeneous Scattering Media: Perturbation Theory and Biomedical Application*. Phd thesis, Deutsche Nationalbibliothek.

Payette, J., Kohlenberg, E. & Leonardi, L. (2005). Assessment of skin flaps using optically based methods for measuring blood flow and oxygenation. *Plastic and Reconstructive Surgery* 115, 539–546.

Perry, D., McGrouther, D. & Bayat, A. (2010). Current tools for noninvasive objective assessment of skin scars. *Plastic and Reconstructive Surgery* 126: 3, 912.

Prahl, S. (1999). Optical absorption of hemoglobin. Internet: http://omlc.ogi.edu/spectra/hemoglobin/index.html, cited at 31.01.2008, Oregon Medical Laser Center.

Prahl, S., Keijzer, M., Jacques, S. & Welch, A. (1989). A Monte Carlo model of light propagation in tissue. *Dosimetry of Laser Radiation in Medicine and Biology* IS 5, 102–111.

Prahl, S., Van Gemert, M. & Welch, A. (1993). Determining the optical properties of turbid media by using the adding-doubling method. *Applied Optics* 32: 4/1.

Preece, S. J. & Claridge, E. (2004). Spectral filter optimization for the recovery of parameters which describe human skin. *IEEE Transactions on Pattern Analysis and Machine Intelligence* 26: 7.

Ramella-Roman, J., Prahl, S. & Jacques, S. (2005). Three Monte Carlo programs of polarized light transport into scattering media: part II. *Optics Express* 13: 25, 10392–10405.

Randall, B. S. (2006). Introduction to Hyperspectral Imaging. Tech. Rep., Microimages Inc, Lincoln, Nebraska, USA.

Reif, R., Wang, M., Joshi, S., A'Amar, O. & Bigio, I. (2007). Optical method for real-time monitoring of drug concentrations facilitates the development of novel methods for drug delivery to brain tissue. *Journal of Biomedical Optics* 12, 034036.

Reuss, J. L. (2005). Multilayer modeling of reflectance pulse oximetry. *IEEE Transactions on Biomedical Engineering* 52: 2, 153–159.

Routaboul, C., Denis, A. & Vinche, A. (1999). Immediate pigment darkening: description, kinetic and biological function. *EJD* 9, 95–99.

Saidi, I. S. (1992). *Transcutaneous Optical Measurement of Hyperbilirubinemia in Neonates*. Phd thesis, Rice University, Houston, USA.

Saidi, I. S., Jacques, S. L. & Tittel, F. K. (1995). Mie and Rayleigh modeling of visible-light scattering in neonatal skin. *Applied Optics* 34: 31, 7410–7418.

Schwertner, H., Jackson, W. & Tolan, G. (1994). Association of low serum concentration of bilirubin with increased risk of coronary artery disease. *Clinical Chemistry* 40: 1, 18.

Segelstein, D. (1981). *The Complex Refractive Index of Water*. Masters thesis, University of Missouri–Kansas City.

Sowa, M. G., Matas, A., Schattka, B. J. & Mantsch, H. H. (2002). Spectroscopic assessment of cutaneous hemodynamics in the presence of high epidermal melanin concentration. *Clinica Chimica Acta* 317: 1-2, 203 – 212.

SphereOptics LLC (2007). Integrating sphere, design and applications. Tech. Rep..

Stamatas, G., Zmudzka, B., Kollias, N. & Beer, J. (2004). Non-Invasive Measurements of Skin Pigmentation *In Situ*. *Pigment Cell Research* 17: 6, 618–626.

Terstappen, K., Larko, O. & Wennberg, A. (2007). Pigmented basal cell carcinoma–comparing the diagnostic methods of SIAscopy and dermoscopy. *Acta Dermato-Venereologica* 87: 3, 238–242.

Thompson, M. S. (2004). *Photodynamic Therapy Utilizing Interstitial Light Delivery Combined With Spectroscopic Methods*. Phd thesis, Lund Institute of Technology.

Tsumura, N., Kawabuchi, M., Hideaki Haneishi, H. & Miyake, Y. (2000). Mapping pigmentation in human skin by multi-visible-spectral imaging by inverse optical scattering technique. In *8th IS&T/SID Color Imaging Conference*. Scottsdale, Arizona, USA: IS&T - The Society for Imaging Science and Technology, 81–84.

Tsumura, N., Ojima, N., Sato, K., Shiraishi, M., Shimizu, H., Nabeshima, H., Akazaki, S., Hori, K. & Miyake, Y. (2003). Image-based skin color and texture analysis/synthesis by extracting hemoglobin and melanin information in the skin. *ACM Transactions on Graphics (TOG)* 22: 3, 770–779.

Tuchin, V. (2007). *Tissue Optics: Light Scattering Methods and Instruments for Medical Diagnosis*. Bellingham, WA, USA: SPIE press.

Tuchin, V. V., Utz, S. R. & Yaroslavsky, I. V. (1994). Tissue optics, light distribution, and spectroscopy. *Optical Engineering* 33: 10.

van de Hulst, H. C. (1980). *Multiple Light Scattering*, vol. 1. New York: Academic Press.

Välisuo, P. & Alander, J. (2008). The effect of the shape and location of the light source in diffuse reflectance measurements. In *21st IEEE International Symposium on Computer-Based Medical Systems*. IEEE Computer Society, 81–86.

Välisuo, P., Harju, T. & Alander, J. (2011a). Reflectance measurement using digital camera and a protecting dome with built in light source. *Biophotonics* 4: 4.

Välisuo, P., Kaartinen, I., Kuokkanen, H. & Alander, J. (2010). The colour of blood in skin: a comparison of Allen's test and photonics simulations. *Skin Research and Technology* 16: 4, 390–396.

Välisuo, P., Kaartinen, I., Tuchin, V. & Alander, J. (2011b). New closed–form approximation for skin chromophore mapping. *Journal of Biomedical Optics* 16: 4, 046012.

Välisuo, P., Mantere, T. & Alander, J. (2009). Solving optical skin simulation model parameters using genetic algorithm. In *The 2nd International Conference on BioMedical Engineering and Informatics*. 376–380.

Wald, N., Boreham, J., Hayward, J. & Bulbrook, R. (1984). Plasma retinol, beta-carotene and vitamin E levels in relation to the future risk of breast cancer. *British Journal of Cancer* 49: 3, 321.

Wang, L. & Jacques, S. (1992). Monte Carlo modeling of light transport in multi-layered tissues in standard C. Tech. Rep., University of Texas MD Anderson Cancer Center.

Wang, L., Jacques, S. L. & Zheng, L. (1995). MCML – Monte Carlo modeling of light transport in multi-layered tissues. *Computer Methods & Programs in Biomedicine* 47, 131–146.

Wang, L. H., Jacques, S. L. & Zheng, L. Q. (1997). CONV - Convolution for responses to a finite diameter photon beam incident on multi-layered tissues. *Computer Methods and Programs in Biomedicine* 54: 3, 141–150.

Whitley, D. (1994). A genetic algorithm tutorial. *Statistics and Computing* 4: 2, 65–85.

Wright, C., Kroner, C. & Draijer R. (2006). Non-invasive methods and stimuli for evaluating the skin's microcirculation. *Pharmacological and Toxicological Methods* 54, 1–25.

Yoon, G., Welch, A., Motamedi, M. & Gemert, M. (1987). Development and application of three-dimensional light distribution model for laser irradiated tissue. *IEEE Journal of Quantum Electronics* 23: 10, 1721 – 1733.

Zhai, H., Chan, H. P., Farahmand, S., Nilsson, G. E. & Maibach, H. I. (2009). Tissue viability imaging: mapping skin erythema. *Skin Research and Technology* 15: 1, 14–19.

Zijlstra, W. G., Buursma, A. & van der Meeuwsen, R. (1991). Absorbtion spectra of human fetal and adult oxyhemoglobin, de-oxyhemoglobin, carboxyhemoglobin and methemoglobin. *Clinical Chemistry* 37: 9, 1633–1638.

Publication I

Välisuo, P. & Alander, J. (2008). The effect of the shape and location of the light source in diffuse reflectance measurements. In *21st IEEE International Symposium on Computer-Based Medical Systems*, pp. 81–86. IEEE Computer Society.

Errata:

- The numbers in x-axis in Figure 9 are in centimeters. They should be multiplied by 10 to get them in millimeters.
- Word *remission* should be replaced with *re–emission* through the whole article.

The effect of the shape and location of the light source in diffuse reflectance measurements

Petri Välisuo
University of Vaasa
petri.valisuo@uwasa.fi

Jarmo Alander
University of Vaasa
jarmo.alander@uwasa.fi

Abstract

Optical measurements are fast and convenient mode to obtain information from human skin. However, the complicated interactions of light with skin may overwhelm our understanding of the measurements. Moreover, the high remittance from the surface of the skin may be often an obstacle for making measurements regarding deeper layers of skin. In this research, we have constructed a simulation model to show from which depths the remittance is coming from. Using this model we have studied the effects of light source shape and location to measure the remittance originating deeper. According to the model, the ring-shaped light source more than doubles the measurement depth, compared with the diffuse light. In fiber-based measurements, increase of the fiber separation increases the measurement depth.

***Index terms* — dermatology, spectroscopy, medical imaging, simulation**

1. Introduction

Remittance spectra of skin conveys information about the structure and state of the dermis, epidermis and even from subcutaneous tissue. The measurement of the spectra is fast and convenient, requiring no contact to the target. The spectra can be measured from a certain point of skin using spectrophotometer, or from a larger area using spectroscopic camera.

The main modes for measuring the spectra are transmission and reflectance setting. In transmission spectroscopy, the sample is illuminated on one side and the light penetrating through the sample is measured on the other side. In reflectance spectroscopy, the sensor and the light source are both situated on the same side. In this mode, the spectroscope measures the light which is reflected back from the skin.

In reflectance spectroscopy, the skin is illuminated with known light source I_0 and the spectra of the reflected light, I_r is measured. Typically visible and near infrared (NIR) light are used for measurements. It is known that certain wavelengths penetrate deeper into the skin than the others. The green light (520 nm) is not going very deep, because it is strongly absorbed by hemoglobin, while red (650 nm) penetrates much deeper, because the skin chromophores absorb it only slightly. Furthermore, the scattering of the skin surface, *stratum corneum*, is so strong, that the diffuse reflectance from the epidermis may partly mask the signal coming deeper under the skin.

The wavelength isn't, by any means, the only parameter influencing to the measurement depth. The relative positions and the geometries of the light source and the detector on the skin surface has also great influence. It is possible to control the measurement depth by light source position and shape design. It is important to know the penetration depth in different conditions to be able to design and optimise the measurement setup for each measurement—to know what was actually measured.

In this paper, a skin model is constructed to simulate light propagation in tissue. The simulation model is first verified by comparing it with the spectrophotometer measurements and then utilised for penetration depth simulations. Several light source shapes and positions are simulated to design a measurement setup which is optimised for epidermis measurements.

2. Background

Optical measurements of skin have been done quite regularly. Typical applications are: blood circulation and oxygenation measurements and skin disorder diagnostics, follow up and treatment. Examples from blood circulation measurements are pulse oximetry [1] and photoplethysmography. The examples of the skin diagnostics are melanoma diagnostics [2, 3, 4, 5]. Shi-

mada *et al.* have also studied the melanin and blood concentration in skin using optical measurements in [6]. Gemert *et al.* have studied skin parameters to improve skin treatment possibilities [7].

2.1. Skin models

The light propagation in tissue is described by the radiative transmission equation [8]. In the general case, the equation is complex and cannot be solved analytically. There are many approximations of the equation, such as Kubelka-Munk theory and diffusion theory. These approximations do not describe well, the light propagation in turbid media, such as human tissue, where neither absorbtion nor scattering can be neglected. Therefore a simulation method which tracks the propagation of separate photons is used more often than the mathematical approximations. The most often used algorithm used in literature is the Monte Carlo Multi Layer (MCML) algorithm developed by Wang *et al.* [9, 10]. It simulates an infinitely thin beam propagating in a medium. If the light source have some finite shape, the light propagation can be calculated by integrating the infinitely thin beam over the area of the light source. Wang *et al.* have also created a program called CONV [11], which can be used to numerically convolute over a finite light beam.

Tuchin [12], Claridge [2] and Reuss [1] have used MCML skin models. Reuss have apparently developed his model from Tuchin's model by adding hypodermis or subcutis layer under the actual skin model. Reuss has also somewhat modified layer thicknesses to be better suited for MCML simulation. Otherwise the model structures are similar. In Claridge's model the *stratum corneum* has been modelled separately from the rest of the epidermis. The Claridge's dermis model consists of only two layers, where Tuchin's and Reuss's model consists of four layers. The number of layers in the model doesn't necessarily mean that the model would be better, but the Reuss's model is documented most accurately. Furthermore, Reuss model was used for pulse-oximeter studies, which suits well for our purposes, to model for blood concentration calculations.

3. Methodology

3.1. Model construction

We adopted Reuss MCML model structure for our simulations mostly as such. Only the thickness of the subcutis was increased to 2 mm, to be able to perform the penetration depth measurements deep enough. This model is shown in Figure (1).

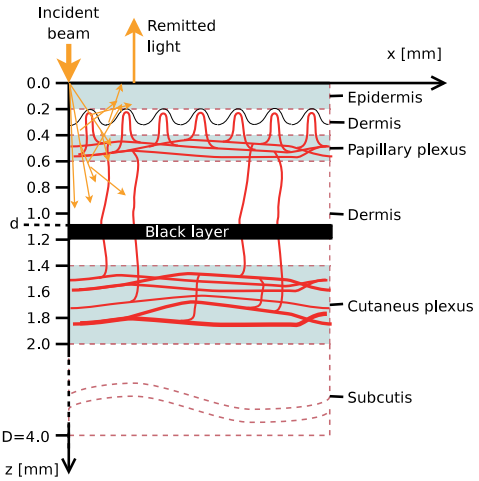

Figure 1. The model of the skin. The names of the layers are in the right hand side. Left hand side displays depths z, from the skin surface in mm.

The model consists of the model structure and its model parameters. The parameters of each layer are absorbtion coefficient μ_a, scattering coefficient μ_s, and anisotropy g. To be able to estimate the absorbtion coefficients, the skin chromophores and their concentrations are needed. The most important chromophores of the skin are hemoglobin and melanin. The absorbtion spectra of hemoglobin is described by Horecker in [13] and tabulated by Prahl in [14]. Both oxygenated hemoglobin and deoxygenated hemoglobin spectra was used. We assumed the oxygen saturation level of 0.98. The nominal value of hemoglobin concentration in blood, 150 g/l, was assumed.

A formula for reproducing the absorbtion spectra of melanin is suggested by Jacques in [15]. This formula was also used here.

Concentrations are also needed, to calculate the absorbtions from absorbtion coefficients. We used the same blood and melanin concentrations than Reuss in [1]. The data is listed in Table (1).

Because we measured also in the NIR band, we added the effect of water into the model. The tabulated absorbtion coefficients of water were taken from the MiePlot program. They are measured by Segelstein in [16]. Obata *et al.* have concluded [17] that the water concentration in epidermis increases linearly from zero to the concentration of dermis c_{wd}. Therefore we can use in the model the concentration c_{wd} in dermis and $c_{we} = c_{wd}/2$ as the average concentration in epidermis.

Table 1. Blood and melanin fractions

Layer	Layer name	Blood fraction	Melanin fraction
1	*Epidermis*	0	0.05
2	*Dermis*	0	0
3	*Papillary Plexus*	0.0556	0
4	*Dermis*	0.0417	0
5	*Cutaneus plexus*	0.2037	0
6	*Subcutis*	0.0417	0

3.2. Model validation

The model is tuned to match its spectra with the measured spectra as closely as possible. To make the model even better, it is also tuned to match to the measured spectra in several distances from the incident light beam.

The hemoglobin concentrations described by Reuss [1] were suitable for our model too. We tuned the melanin concentration to 2%. It is somewhat lower than reported in [6]. But the thickness of the epidermis in the model is thicker than what is actually measured. Therefore the total volume of the melanin was pretty close to measurements. Too low or too high levels of melanin caused the two first reflectance peak at the wavelengths of 510 nm and 560 nm to be inbalanced.

The water concentration adjusts the slope from 700 nm to 900 nm. Without water in the model, the reflection is almost constant in that range.

The measured and simulated spectra are shown in Figure (2). They resemble each other in each distance, but there are also differences. The difference of the two spectra are shown in Figure 3. The model needs clearly more optimisation to be able to really replace measurements in all wavelengths and distances. The relative error e, is quite large, except at 770 nm where $e \in \pm 5\%$. The inaccuracy of the model in other wavelengts prevents using it to make much absolute conclusion based only to the model. The model is still useful for estimating relative quality of different light source shapes. For $\lambda \approx 770$ nm we may even make rough absolute estimates.

3.3. The penetration depth simulation

To simulate the penetration depth of the light in the skin, a simulation arrangement shown in Figure (1) was made. The skin surface is illuminated by an infinitely thin light beam. A perfectly absorbing black layer is constructed by defining its refraction coefficient to be exactly the same than the skin, the absorbtion coefficient approaching to infinity and scattering coefficient to zero. We refer to this layer later shortly as black layer. The black layer is put under the epidermis layer, at depth d from the skin surface. The spatial distribution of light escaping from the skin surface, around the beam is spherically symmetric. The light intensity on the skin surface is highest near the incident beam, where $x \approx 0$ and decreases roughly exponentially by increasing distance, x. The light intensity as a function of the distance x is shown in Figure (4).

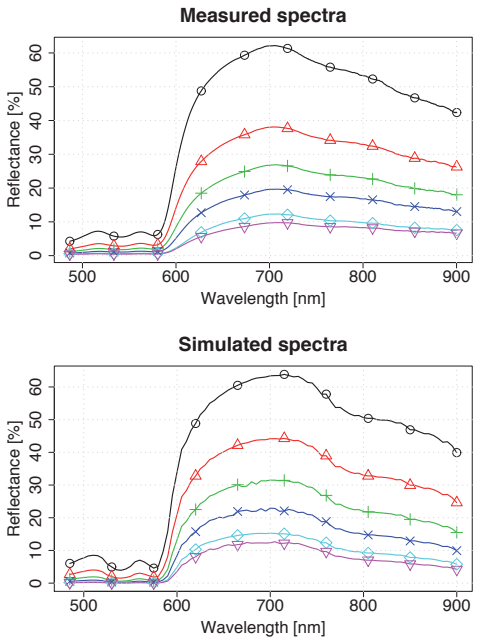

Figure 2. Measured and simulated reflectance spectra, x is: O = 3.3, Δ = 4.0, $+$ = 4.8, $\times$ = 5.6, $\diamond$ = 6.5 and ∇ = 7.3 mm

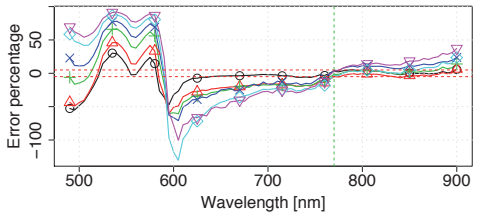

Figure 3. Difference of measured and simulated spectra, x is: O = 3.3, Δ = 4.0, $+$ = 4.8, $\times$ = 5.6, $\diamond$ = 6.5 and ∇ = 7.3 mm

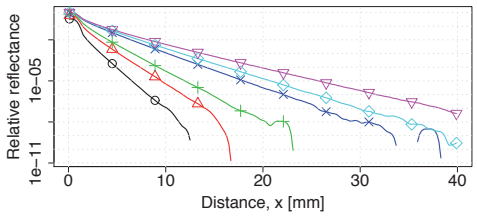

Figure 4. Spatial light profile of 1 mm light beam. Black layer is placed below: O = epidermis, Δ = dermis 1, + = papillary plexus, × = dermis 2, ◇ = cutaneous plexus, ∇ = subcutis.

When the black layer is near skin surface, it has a strong effect to the light intensity on top of the skin surface. The effect of the black layer depends on x, too. Figure (4) shows the simulated light intensity as a function of x. The influence of the black layer is the strongest far away from the incident beam, whereas it has to be really close to the surface to be seen near the incident beam.

To be able to better examine the exact proportions of information coming from different depths, contained in the remitted light, the simulation data can be plotted in a way described next.

The light intensity I, on the surface is highest, when the black layer is lying infinitely deep. I could then be calculated by integrating the reflectance over all depths z:

$$I_{tot} = \int_0^\infty i(z)dz. \tag{1}$$

If the thickness of the skin model, D is large enough, the amount of light transmitted through it is negligible. Therefore the remittance which would be caused by the layers deeper than D is also negligible. In this case, the upper limit of integration in Equation (1) can be replaced by D. Therefore the subcutis layer is thicker in our model than in Reuss model. The simulations will reveal if the assumption of negligible transmittance truly holds for the model or not.

After inserting the black layer at depth d, the remitted light intensity is only:

$$I_d = \int_0^d i(z)dz. \tag{2}$$

The amount of light coming deeper than d can now be calculated:

$$I_l = \int_d^D i(z)dz = I_{tot} - I_d. \tag{3}$$

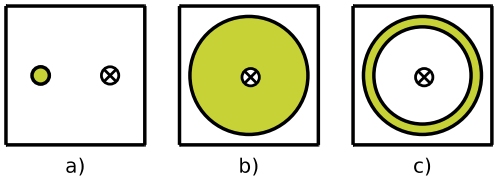

Figure 5. Simulated light source shapes: a) 1mm beam, b) diffuse field, c) ring shape. Crossed circle shows the measurement point.

The proportion of light coming deeper than $z = d$, when there is no black layer preventing it is:

$$P_d = \frac{I_l}{I_{tot}} = \frac{I_{tot} - I_d}{I_{tot}} = 1 - \frac{I_d}{I_{tot}}. \tag{4}$$

Using Equation (4), it is now possible to plot a measurement depth profile, by running simulation using different values of $d \in [0, D]$.

3.4. Light source shape simulation

The MCML program simulates the light field produced by the infinitely thin light beam. This result needs to be convoluted over finite light source shapes. To study the effect of the shape of the light source, we will simulate three different kind of light sources, shown in Figure (5). These are: a) a fiber beam, which diameter $d = 1$ mm, b) diffuse light field, radius R and c) ring-shaped light source, outer radius R and inner radius r.

Relatively thin light beam is used often when the measurements are done using optical fibers in guiding the light into the skin and guiding the remitted light to the measurement device, such as spectrophotometer. The CONV program is used to convolve the fiber beam field. The benefits of the point-source is that the remittance from the epidermis is mostly avoided in the area of the measurement, provided that the distance in between measurement and incident light is sufficient.

The diffuse light field is often conceived as an optimal lighting condition in photography. It is also used often in spectroscopic measurements with measurement probe containing an integrating sphere. When the incident light beam encounters the *stratum corneum* on the epidermis, the light will be scattered strongly and will be quite diffuse irrespective of the original light beam direction. Therefore, the diffuse field simulation is done by convolving the incoming perpendicular light beam over a large disk. In this way the light field will be even, and the *stratum corneum* will make it diffuse before the light hits the dermis. The remitted light is then measured in the middle of this approximately diffuse large

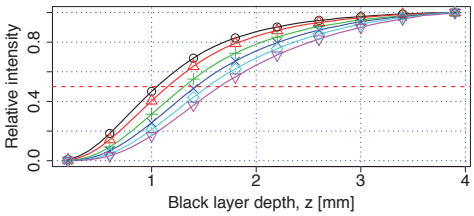

Figure 6. Depth profile of 1 mm beam, x is: O = 3.3, Δ = 4.0, + = 4.8, × = 5.6, ◇ = 6.5, ∇ = 7.3 mm

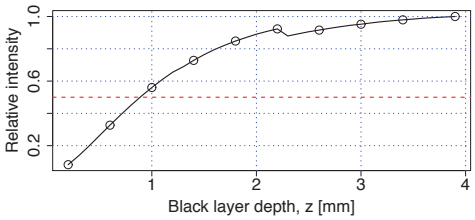

Figure 7. Depth profile of diffuse light source

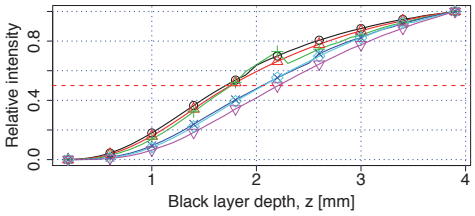

Figure 8. Depth profile of ring-shaped light source, x is: O = 3.3, Δ = 4.0, + = 4.8, × = 5.6, ◇ = 6.5, ∇ = 7.3 mm

disk.

In the middle of the ring-shaped light source, the light is propagating radially towards the center of the ring. Again the epidermis remittance is avoided and the light intensity is accumulating in the middle improving the signal to noise ratio of the measurement. The ring-shaped light field is simulated with a modified CONV-program, simulating first the field by the disk having radius R, and subtracting the field of the disk radius of r.

4. Experiment

The simulation is repeated at 6 different distances x, from the incident light beam. These are the same distances which were used for measurements. The wavelength used in the simulation was 770 nm, because the model was most accurate at this wavelength.

4.1. Single fiber light source simulation

The simulations for 1 mm fiber beam are shown in Figure (6). The curves in the figure show how much remittance is accumulated due to the layers from the top of the skin to the depth z. For example, half of the remittance is caused by the layers above 1.0 mm, when the x is 3.3 mm. If we increase x to 7.3 mm, then this 50% remittance threshold will be 1.6 mm.

4.2. Diffuse light source

The distance x does not change the depth profile of the measurement. Therefore the Figure 7 contain only one curve. The 50% remittance value is 0.88 mm and it cannot be improved. The sudden step in the curve is an artifact produced by the random nature of the Monte Carlo simulation method.

4.3. Ring-shaped light source

The depth profile of the ring-shaped light source is not as steep as the profile of the fiber beam, as shown in Figure 8. The distance x has now smaller effect to the depth. This is because the remitted light is now accumulated from several points and it therefore contains always light originating from different distances simultaneously. The 50% remittance value is in between 1.7 - 2.2 mm depending on the value of x.

4.4. Summary

The depths of the 50% remittance thresholds of diffuse light, fiber beam and ring-shaped light sources over all six values of x are shown in Figure 9. The remittance from the ring-shaped light-source originates clearly deeper than the others. The performance of both fiber beam and ring light can be controlled. In diffuse light, 50% of the remittance is originated above 0.88 mm and it cannot be improved.

5. Discussion

The general skin model, fulfilling also the spatial requirements, is difficult to make. Currently we tried to fit the model with the measurements by changing only the skin chromophore concentrations, which affect

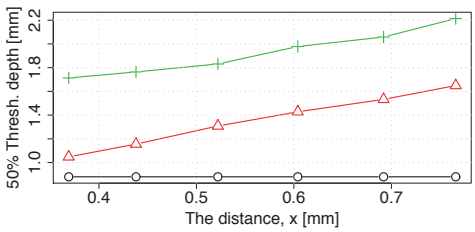

Figure 9. Half remittance thresholds of simulated light source shapes for all simulated values of x. Light sources are: O = Diffuse, Δ = 1 mm beam and $+$ = ring.

to the absorbtion coefficients of the layers. Accurate model fitting may also require adjusting the scattering coefficients and layer thicknesses. The evaluation of the each combination takes several hours. Therefore it is not possible to fit all these parameters by hand, but a suitable optimization method should be used.

6. Conclusion

We simulated the depth profile of the reflectance measurements. These simulations make it possible to understand, from where the information included in the remitted light is coming.

In reflectance measurements, the location and the shape of the light source is crucial. If the target is to measure epidermis or even subcutis, the diffuse light field does not work very well. The measurements performed using one fiber leading the light into the skin and another for guiding the remitted light to the measurement device, may double the depth of the measurement, provided that the distance in between the fibers is large enough. A light source shape, which is optimised for the measurement, may further increase the depth of the measurement. The ring-shaped light source allows measurements more than 50% deeper than the fiber-beam.

7. Acknowledgement

We like to express our gratitude to Oy Abilita Ab and TEKES for financing this work.

References

[1] J. L. Reuss, “Multilayer modeling of reflectance pulse oximetry,” *IEEE Transactions on Biomedical Engineering*, vol. 52, no. 2, Feb. 2005.

[2] E. Claridge, S. Cotton, P. Hall, and M. Moncrieff, “From colour to tissue histology: physics based interpretation of images of pigmented skin lesions,” in *MICCAI (1)*, 2002, pp. 730–738.

[3] T. E. M. Nordling, J. Koljonen, J. Nyström, I. Bodèn, B. Lindholm-Sethson, P. Geladi, and J. T. Alander, “Wavelength selection by genetic algorithms in near infrared spectra for melanoma diagnosis,” *Proceedings of the 3rd European Medical and Biological Engineering Conference (EMBEC’05)*, vol. 11, 2005.

[4] E. Claridge and S. J. Preece, “An inverse method for the recovery of tissue parameters from colour images,” in *Information processing in Medical Imaging*. Springer, 2003.

[5] S. J. Preece and E. Claridge, “Spectral Filter Optimization for the Recovery of Parameters Which Describe Human Skin,” *IEEE Transactions on Pattern Analysis and Machine Intelligence*, vol. 26, no. 7, Jul. 2004.

[6] M. Shimada, Y. Yamada, M. Itoh, and Yatagai T., “Melanin and blood concentration in human skin studied by multiple regression analysis: experiments,” *Physics in Medicine and Biology*, no. 46, pp. 2385–2395, 2001.

[7] M. J. C. van Gemert, S. L. Jacques, H. J. C. M. Sterenborg, and W. M. Star, “Skin optics,” *IEEE Transactions on Biomedical Engineering*, vol. 36, no. 12, Dec. 89.

[8] M. Kinnunen, “Comparison of optical coherence tomography, the pulsed photoacoustic technique, and the time-of-flight technique in glucose measurements in vitro,” Ph.D. dissertation, University of Oulu, 18 Aug. 2006.

[9] S. A. Prahl, M. Keijzer, and S. L. Jacques, “A Monte Carlo model of light propagation in tissue.” in *SPIE Proceedings of Dosimetry of Laser Radiation in Medicine and Biology*, D. H. S. G. J. Müller, Ed., vol. IS 5, 1989, pp. 102–111.

[10] L. Wang, S. L. Jacques, and L. Zheng, “MCML – Monte Carlo modeling of light transport in multi-layered tissues,” *Computer Methods & Programs in Biomedicine*, vol. 47, pp. 131–146, 1995.

[11] L. H. Wang, S. L. Jacques, and L. Q. Zheng, “CONV - Convolution for responses to a finite diameter photon beam incident on multi-layered tissues,” *Computer Methods and Programs in Biomedicine*, vol. 54, no. 3, pp. 141–150, 1997.

[12] V. V. Tuchin, S. R. Utz, and I. V. Yaroslavsky, “Tissue optics, light distribution, and spectroscopy,” *Optical Engineering*, vol. 33, no. 10, Oct. 1994.

[13] B. L. Horecker, “The absorbtion spectra of hemoglobin and its derivatives in the visible and near infra-red regions,” *The Journal of Biological Chemistry*, pp. 173–183, Dec. 1942.

[14] S. Prahl, “Optical absorption of hemoglobin,” Oregon Medical Laser Center, Internet: http://omlc.ogi.edu/spectra/hemoglobin/index.html, cited at 31.01.2008, Dec. 1999.

[15] S. L. Jacques and D. J. McAuliffe, “The melanosome: threshold temperature for explosive vaporization and internal absorption coefficient during pulsed laser irradiation,” *Photochemistry and Photobiology*, vol. 53, pp. 769–775, 1991.
[16] D. Segelstein, “The Complex Refractive Index of Water,” Master’s thesis, University of Missouri–Kansas City, 1981.
[17] M. Obata and H. Tagami, “Electrical determination of water content and concentration profile in simulation model of in vivo stratum corneum,” *Journal of Investigative Dermatology*, vol. 92, no. 6, Jun. 1989.

Publication II

Välisuo, P., Mantere, T. & Alander, J. (2009). Solving optical skin simulation model parameters using genetic algorithm. In *The 2nd International Conference on BioMedical Engineering and Informatics*, 376–380.

Solving optical skin simulation model parameters using genetic algorithm

Petri Välisuo
University of Vaasa
firstname.lastname@uwasa.fi

Timo Mantere
University of Vaasa
firstname.lastname@uwasa.fi

Jarmo Alander
University of Vaasa
firstname.lastname@uwasa.fi

***Abstract*—Near infrared spectroscopy is noninvasive method to obtain information from materials, such as human skin. A simulation model of light interaction with skin is used to simulate skin reflectance spectra when the chemical and physical parameters of the skin are known. Genetic algorithm is utilised for tuning the simulator to solve the inverse problem; to calculate the skin parameters from the measured reflectance spectra. The inverse problems are often ill-posed, which was also true for this problem in its original form. After assuming all physical parameters as fixed, the problem was regularised and a unique solution for blood melanin and water concentrations was found in all simulations. The accuracy and the uniqueness of the solution proved to be almost independent of the provided spectral resolution, as long as it is larger than three wavelengths. The accuracy of the solution depends on the MCML simulation noise level and the fitness function used. The performance of four different fitness functions was evaluated using fitness landscape and noise analysis, and the best of them was chosen. The achieved accuracy is satisfactory for many applications and it can probably be further improved by increasing the number of photons used in the MCML simulation or by further optimising the fitness function.**

***Index Terms*—Genetic algorithms, Monte Carlo methods, Inverse problems, Biomedical engineering, Optics, Biological tissues.**

I. Introduction

The reflectance spectra of human skin can be used to infer its physical structure and chemical contents. The reflectance spectra measurement is fast and convenient method for obtaining information from the skin. The spectra can be measured using a spectrophotometer or even a digital camera. In reflectance spectroscopy, the skin is illuminated with the known light source I_0 and the spectra of the reflected light, I_r is measured. Often visible and near infrared (NIR) light are used for measurements, because they are penetrating deeper into the skin than the longer or shorter wavelengths.

However, the light interaction with skin is complicated, making it difficult to infer skin chromophore concentrations or physical parameters from the measured spectra. The light propagation in tissue is described by the radiative transmission equation [1]. In general case, the equation cannot be solved analytically. There are many approximations of the equation, such as Kubelka-Munk theory and diffusion theory. Baranoski provides a review of typically used methods in [2]. One of the most accurate methods is the Carlo Multi Layer (MCML) algorithm developed by [3] [4] and [5].

The MCML simulation and skin parameter estimation from the reflectance has been used in many works, such as the development of the pulse oximeter [6], melanoma diagnostics [7] [8] [9], melanin and blood concentration measurements [10], skin treatment planning [11]. We used the simulation model also for the determination of the skin information depth [12].

The prerequisite to the MCML simulation is that the skin parameters are known. Normally the case is the opposite, the reflectance spectra is known, and the skin parameters need to be calculated. This inverse problem can be solved by tuning the parameters of the MCML skin model, until the simulated spectra match the measured spectra. Tuning the model manually is an overly tedious process. Zhang *et al.* have used GA for tuning of the MCML model parameters, until the simulated and the measured spectra match [13]. The optimised model parameters are then the solution to the inverse problem. In this article we have also used GA for solving the inverse problem.

A. GA

Genetic algorithms are evolutionary algorithms, which search solutions for optimisation problems using techniques inspired by evolutionary biology such as inheritance, mutation, selection, and crossover. The genetic algorithms are introduced by [14] and [15].

Genetic algorithms start with a population of solution candidates. A new population is created by keeping the best individuals, and replacing the rest with the new candidates. The new candidates are recombined and mutated versions of the individuals in the old population, and some of the best previous individuals left intact. The new candidates tend to converge towards local and global optima. The better the optima is, the more probably some individual solution candidates will converge near it. The mutations help GA not to stuck to the local optima.

B. Organisation of the article

This article is organised as follows. First several fitness function candidates are evaluated by analysing the fitness space, and the one which provides the most accurate solution is selected. Then the skin model is regularized to establish one to one mapping between the model parameters and the

978-1-4244-4134-1/09/$25.00 ©2009 IEEE

reflectance spectra. Then the skin model parameters are solved from the reflectance spectra using genetic algorithm.

II. Optimisation

A. Skin model

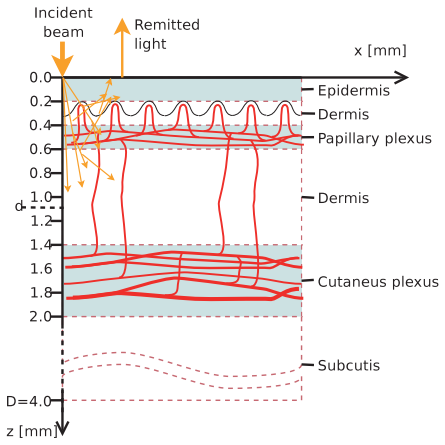

Fig. 1. MCML skin model

The skin model for MCML simulation is used in many works [16] [7] [6] [12]. Here we will use the same skin model that we used in [12], which was originally adopted from the Reuss model. The structure of the model is shown in Figure (1). The model parameters consist of values which determine how much the thicknesses of the skin layers and the concentrations of the most important skin chromophores differs from the nominal values given in [12]. Those nominal values were obtained by tuning the model to the measured spectra of the fingertip.

B. Fitness function candidates

By simulating the skin model with certain input parameters P_i, a simulated reflectance spectrum is obtained. The similarity of the simulated spectrum and the measured spectrum is proportional to the fitness of the current parameter combination P_i. In this research, we have used the difference of the simulated spectrum and the measured spectrum as a measure of fitness. The task of the optimisation is then to find the minimum value for the fitness function.

The suitable fitness function should be selected first. The quality of the fitness function for inverse problems can be estimated by performing the forward simulation with different parameter values P_i and then examining the fitness space of the selected fitness function. The MCML simulation is stochastic inducing noise to the fitness space. The sensitivity of the fitness function to the parameter change versus its sensitivity to the noise determines the eventual accuracy of the optimisation.

In this research, several typical fitness function candidates: Mean Square Error (MSE), Mean Absolute Error (MAE), Relative MSE (rMSE) and relative MAE (rMAE) are evaluated. These candidates are shown in Equations (1-4), where R_i is the ideal spectrum value at wavelength λ_i and r_i is the simulated value at the same wavelength and N is the number of simulated and measured wavelengths, e.g. the spectral resolution.

$$\text{rMSE}: \quad F_1 = \frac{1}{N}\Sigma_{i=i}^{N}\left(\frac{R_i - r_i}{R_i}\right)^2 \tag{1}$$

$$\text{rMAE}: \quad F_2 = \frac{1}{N}\Sigma_{i=1}^{N}\left|\frac{R_i - r_i}{R_i}\right| \tag{2}$$

$$\text{MAE}: \quad F_3 = \frac{1}{N}\Sigma_{i=1}^{N}|R_i - r_i| \tag{3}$$

$$\text{MSE}: \quad F_4 = \frac{1}{N}\Sigma_{i=i}^{N}\left(R_i - r_i\right)^2 \tag{4}$$

C. Noise sensitivity

The sensitivity of the each fitness function to the noise was estimated by performing the MCML simulation 30 times over the wavelength range $\lambda \in [450, 960]$ nm, with the same parameters P_i. The mean spectrum and the duplicated standard deviation are shown in Figure (2). The line represents the mean value and the dots show the range in which the simulated value will reside with the probability of 95%.

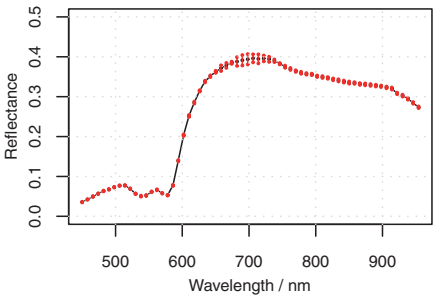

Fig. 2. The mean spectrum, μ_r of 30 simulations, shown with black line. The red dots show the range in between the individual simulations are within the certainty of 95%.

The noise of the spectra is also observable from the fitness. The noise level, η_i, of each fitness function shown in Equations (1-4) were estimated. The noise level was determined as a fitness of such a spectrum, which resides two times the standard deviation, 2σ, above the mean spectra. The noise levels of each fitness function are shown in Table (I).

TABLE I
THE SIMULATED NOISES OF THE FITNESS FUNCTIONS

rMSE:	$\eta_1 = 2.122189 \cdot 10^{-04}$
rMAE:	$\eta_2 = 1.313832 \cdot 10^{-02}$
MAE:	$\eta_3 = 2.995423 \cdot 10^{-03}$
MSE:	$\eta_4 = 1.554092 \cdot 10^{-05}$

The noise, η_i, is dependent on the accuracy of the simulation. The MCML simulation approximates the reflectance spectra stochastically by simulating the propagation of individual photons. The larger the number of the photons in the simulation, the smaller the noise level. The spectral resolution used may also have an effect to η_i. To study the dependency of rMSE of the simulation parameters, the noise analysis for η_1 was repeated by using several spectral resolutions, $N = \{3, 5, 9, 17, 33, 65\}$ and different number of photons $n_p = \{10\ 000, 20\ 000, 100\ 000\}$. According to the noise statistics, shown in Figure (3), number of photons, n_p, was expectedly the most important factor for η_1, whereas the spectral resolution, N, seems to have only modest effect. The rest of the simulations are executed using values $N = 17$ and $n_p = 100\ 000$. The N and N_p are assumed to have similar effect to η_2, η_3 and η_4 as well.

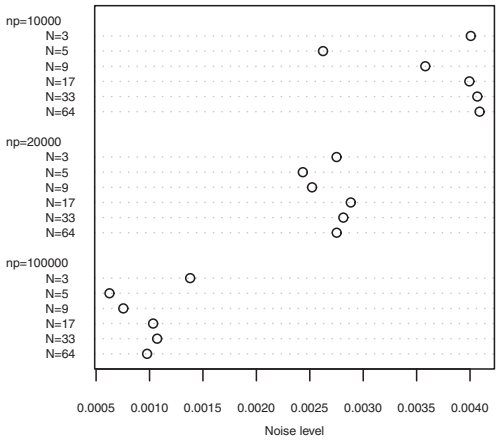

Fig. 3. The noise level with different spectral resolutions (N) and number of photons used in MC simulation (np)

D. Fitness space

Next, the sensitivity of the fitness functions to the parameter perturbation was evaluated. First, an ideal spectrum R_{ideal}, was simulated, using input parameter combination P_{ideal}. Then several spectra r_i were simulated, letting one of the parameters in the set P_i to iterate over a range of values near to its initial value. Then the fitnesses F_i of the parameter combinations P_i were calculated using each of the fitness functions listed in Equations (1-4). When P_i approaches P_{ideal}, the fitness F_j goes below the noise level η_j. In this case, the fitness function can no longer differentiate the current parameter combination from the initial anymore. The quality criteria for the fitness function is the area of the fitness surface, which is under the noise level. The smaller the area, the more accurate the optimisation result. The sensitivities of the fitness functions 1 and 3 related to the noise levels are shown in Figure 4.

TABLE II
THE EXPECTED ACCURACY OF THE ESTIMATED CONCENTRATIONS ($\hat{C}_M$, $\hat{C}_B$, $\hat{C}_W$), WHEN THE ACTUAL CONCENTRATIONS (C_M, C_B, C_W) ARE NORMALIZED AS 1.

Fun	Melanin $\hat{C}_M$	Blood $\hat{C}_B$	Water $\hat{C}_W$
F_1	$\in [0.96, 1.06]$	$\in [0.96, 1.04]$	$\in [0.84, 1.20]$
F_2	$\in [0.94, 1.06]$	$\in [0.96, 1.04]$	$\in [0.73, 1.13]$
F_3	$\in [0.93, 1.07]$	$\in [0.96, 1.05]$	$\in [0.77, 1.23]$
F_4	$\in [0.93, 1.07]$	$\in [0.95, 1.05]$	$\in [0.84, 1.20]$

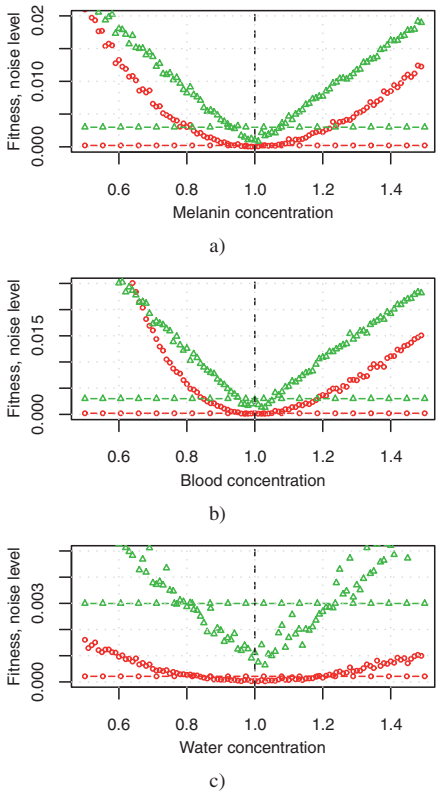

Fig. 4. The fitness function values F_1 and F_3 related to the noise levels η_1 and η_3, when perturbing a) melanin concentration, b) blood concentration, and c) water concentration. The fitness function F_1 and the noise η_1 values are shown as circles (O) and the F_3 and η_3 values as triangles (Δ). The noise levels are the dashed horizontal lines.

The rMSE fitness function, given by Equation (1) is the best and it was used for following simulations. The Figure (4) shows the results of the simulations and reveals the accuracy which can be achieved with estimating the parameter values. These accuracies are listed in Table (II).

E. Regularisation

Often the inverse problems are ill-posed and some regularisation assumptions are needed. When analysing skin, the chemical properties, i.e. the chemical concentrations, are more interesting than the physical ones, such as layer thicknesses and scattering coefficients, since the physical parameters are rather constant whereas the chemical parameters change over time. The change in chemical concentrations may express certain pathological states, such as hypoxia, inflammation, etc.

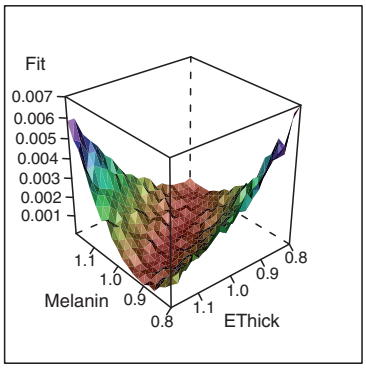

a)

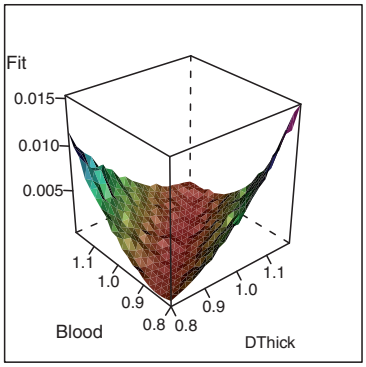

b)

Fig. 5. The fitness values as a function of a) melanin concentration and epidermis thickness and b) blood concentration and dermis thickness.

Claridge *et al.* show in [8] that with their method, there exists one-to-one mapping between the skin color and the skin parameters. However, we found out that in MCML model, some parameters will have too similar effect to the spectra to solve them all by optimisation. The thickness of the epidermis and the melanin concentration seem to have similar effect to the simulated spectra e.g. see Figure (5 a). According to Beer-Lambert-law [17], [18], the absorbtion is directly proportional to the pathlength, concentration and absorbtion coefficient. In this case the pathlength is proportional to the epidermis thickness, d_E, and the melanin concentration C_M. The melanin absorbtion coefficient is $a_M(\lambda)$.

TABLE III
THE FINALL FITNESS OF THE SOLUTION AS A FUNCTION OF SPECTRAL RESOLUTION

N	3	5	9	17	33	64
Fit	0.065	0.033	0.036	0.037	0.037	0.037

$$A = a_M(\lambda) d_E C_M \tag{5}$$

According to Equation (5), it would be impossible to separate the effect of d_E and C_M, if epidermis would only absorb light. Actually the change of d_E should be distinguishable from the change of C_M due to different scatter coefficients of the layers, but this difference is so small that the separation would be difficult in practice. Therefore we assume here, that the thickness is constant and the melanin concentration is solved by the optimisation.

Almost the same applies to the blood concentration and the dermis thickness, see Figure (5 b). Therefore only the blood concentration is solved, and the thickness of the dermis is kept constant. The effect of the scattering coefficient is negligible and therefore its value can be fixed to the nominal value. The remaining parameters for optimisation are: melanin, blood, and water concentrations.

F. GA optimisation

GA simulations were done using Parallel Genetic Algorithm Library, PGAPack [19]. The population sizes in all simulations were 30 individuals and the simulation was executed for 300 generations. The fitness function is shown in Equation (1).

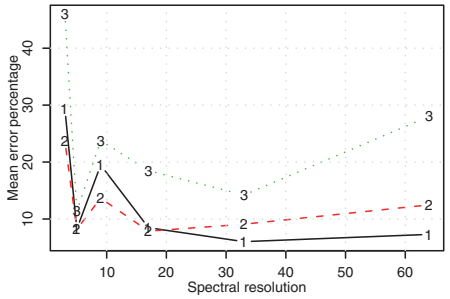

Fig. 6. The accuracy of the parameters of the best individual as a function of spectral resolution: 1=Blood concentration, 2=Melanin concentration, 3=Water concentration.

The original reference spectra R contains 64 wavelengths from the range where $\lambda \in [450, 960]$ nm. The values of R are obtained as an output of the MCML simulation by using the following values. The physical parameters of the skin: the thickness of the dermis d_E, the thickness of the epidermis d_x, and the scattering coefficient μ_s are set to the nominal value, 1.0. The chemical concentrations of blood (C_B), melanin (C_M) and water (C_W) are set to random value in between $[0.1, 3.0]$. The GA starts with random population and it is expected to approach these values before the completion. The same simulation is executed eight times in order to have better statistical estimation of the accuracy of the result. To examine how the spectral resolution affects the final fitness, the same simulation was repeated with six spectral resolutions: $n \in \{3, 5, 9, 17, 32, 64\}$.

III. Results

The result of the simulation is shown in Table (III). The value of N does not seem to have much effect to the final fitness, if it is larger than three. The reason for this is that the absorbtion peaks of the chemicals in the VIS-NIR range are not as sharp as in the NIR–MID-IR range. The scattering is only slightly wavelength dependent. Therefore each parameter will change the shape of the spectra quite smoothly. Only a few sample points are needed for detecting the change of the shape.

What is even more important, is how much the parameter values of the solution differ from the correct values. This is shown in Figure (6). Again, the spectral resolution does not have much effect, if there is more than three wavelengths. The uncertainty of the resolved melanin and blood concentration is above $\pm 8\%$ and respectively above $\pm 18\%$ of the water concentration.

IV. Conclusion

An MCML skin model was used in order to reveal the relation between the skin parameters and the skin color. The model was inversed with the genetic algorithm to find the skin parameters, when the skin spectra was known. The quality of the solutions with several spectral resolutions were evaluated. It was concluded that the spectral resolution has not much effect to the quality of the solution, because absorbance peaks in the VIS-NIR band are quite smooth. It was also examined, if the relation between the skin spectra and the skin model parameters are unique. It was found that some parameters are heavily dependent on each other, and therefore unique solution cannot be found. To make the solution unique, the regularisation assumption, that the physical parameters are fixed, and the chemical parameters are free, was used. The GA was able to find the solution every time, and it was always the same, notwithstanding the noise that was due to the stochastic simulation model. Four different fitness functions were evaluated and the one which produced the best accuracy was selected. The final accuracy of the optimisation was found to comply with the estimates made before the simulation, as shown in Table (II).

V. Acknowledgement

The author is very gratefull to the Oy Abilita Ab, TEKES and The Finnish Cultural Foundation South Ostrobothnia Regional Fund for financing this work.

References

[1] M. Kinnunen, "Comparison of optical coherence tomography, the pulsed photoacoustic technique, and the time-of-flight technique in glucose measurements in vitro," Ph.D. dissertation, University of Oulu, 18 Aug. 2006.

[2] G. V. G. Baranoski and A. Krishnaswamy, "Light interaction with human skin: from believable images to predictable models," in *SIGGRAPH Asia '08: ACM SIGGRAPH ASIA 2008 courses*. New York, NY, USA: ACM, 2008, pp. 1–80.

[3] S. A. Prahl, M. Keijzer, and S. L. Jacques, "A Monte Carlo model of light propagation in tissue." in *SPIE Proceedings of Dosimetry of Laser Radiation in Medicine and Biology*, D. H. S. G. J. Müller, Ed., vol. IS 5, 1989, pp. 102–111.

[4] L. Wang, S. L. Jacques, and L. Zheng, "MCML – Monte Carlo modeling of light transport in multi-layered tissues," *Computer Methods & Programs in Biomedicine*, vol. 47, pp. 131–146, 1995.

[5] L. H. Wang, S. L. Jacques, and L. Q. Zheng, "CONV - Convolution for responses to a finite diameter photon beam incident on multi-layered tissues," *Computer Methods and Programs in Biomedicine*, vol. 54, no. 3, pp. 141–150, 1997.

[6] J. L. Reuss, "Multilayer modeling of reflectance pulse oximetry," *IEEE Transactions on Biomedical Engineering*, vol. 52, no. 2, Feb. 2005.

[7] E. Claridge, S. Cotton, P. Hall, and M. Moncrieff, "From colour to tissue histology: physics based interpretation of images of pigmented skin lesions," in *MICCAI (1)*, 2002, pp. 730–738.

[8] E. Claridge and S. J. Preece, "An inverse method for the recovery of tissue parameters from colour images," in *Information processing in Medical Imaging*. Springer, 2003.

[9] S. J. Preece and E. Claridge, "Spectral filter optimization for the recovery of parameters which describe human skin," *IEEE Transactions on Pattern Analysis and Machine Intelligence*, vol. 26, no. 7, Jul. 2004.

[10] M. Shimada, Y. Yamada, M. Itoh, and Yatagai T., "Melanin and blood concentration in human skin studied by multiple regression analysis: experiments," *Physics in Medicine and Biology*, no. 46, pp. 2385–2395, 2001.

[11] M. J. C. van Gemert, S. L. Jacques, H. J. C. M. Sterenborg, and W. M. Star, "Skin optics," *IEEE Transactions on Biomedical Engineering*, vol. 36, no. 12, Dec. 89.

[12] P. Välisuo and J. Alander, "The effect of the shape and location of the light source in diffuse reflectance measurements," in *21st IEEE International Symposium on Computer-Based Medical Systems*, 2008, pp. 81–86.

[13] R. Zhang, W. Verkrusse, B. Choi, J. A. Viator, B. Jung, L. O. Svaasand, G. Aguilar, and J. S. Nelson, "Determination of human skin optical properties from spectrophotometric measurements based on optimization by genetic algoriths," *Journal of Biomedical Optics*, vol. 10, no. 2, Mar. 2005.

[14] J. H. Holland, *Adaptation in Natural and Artificial System*, Ann Arbor, Ed. The University of Michigan press, 1975.

[15] D. E. Goldberg, *Genetic Algorithms in Search Optimization & Machine Learning*. Addison Wesley, 1989.

[16] V. V. Tuchin, S. R. Utz, and I. V. Yaroslavsky, "Tissue optics, light distribution, and spectroscopy," *Optical Engineering*, vol. 33, no. 10, Oct. 1994.

[17] P. N. Prasad, *Introduction to Biophotonics*. Wiley, 2003.

[18] T. Igarashi, K. Nishino, , and S. Nayar, *The Appearance of Human Skin: A Survey*, ser. Foundations and Trends in Computer Graphics and Vision, B. Curless, L. Van Gool, , and R. Szeliski, Eds. Now Publishers Inc, 2007, vol. 3.

[19] D. Levine, "Users guide to the PGAPack parallel genetic algorithm library," U. S. Department of Energy, Tech. Rep., 1996, pGAPACK is available at ftp://ftp.mcs.anl.gov/pub/pgapack/.

Publication III

Välisuo, P., Kaartinen, I., Kuokkanen, H. & Alander, J. (2010). The colour of blood in skin: a comparison of Allen's test and photonics simulations. *Skin Research and Technology* 16: 4, 390–396.

Errata: A reference is missing. Paragraphs two and three from subsection "Tristimulus values" are cited from:
Wikipedia contributors, CIE 1931 color space [Online] (2009). In Wikipedia, The Free Encyclopedia. Cited at September 2009, Available at `http://en.wikipedia.org/w/index.php?title=CIE_1931_color_space&oldid=315738095`

Skin Research and Technology 2010; ■■: 1–7
Printed in Singapore · All rights reserved
doi: 10.1111/j.1600-0846.2010.00449.x

Skin Research and Technology

The colour of blood in skin: a comparison of Allen's test and photonics simulations

Petri Välisuo[1], Ilkka Kaartinen[2], Hannu Kuokkanen[2] and Jarmo Alander[1]

[1]Department of Electrical Engineering and Automation, University of Vaasa, Wolffintie, Vaasa, Finland and [2]Department of Plastic Surgery, Tampere University Hospital, Tampere, Finland

Background: The colour of the skin reflects many physiological and pathological states of an individual. Usually, the skin colour is examined by the bare eye alone. Several scaling systems have been developed to quantify the sensory evaluation of skin colour. In this work, the reflectance of the skin is measured directly using an objective instrument. Haemoglobin inside the dermal circulation is one of the key factors of skin colour and it also has a major role in the appearance of many skin lesions and scars. To quantitatively measure and analyse such conditions, the relation between the skin colour and the haemoglobin concentration in the skin needs to be resolved.
Methods: To examine the effect of blood concentration on the skin colour, five Allen's tests were performed on 20 persons. The skin colour change was measured using a spectrophotometer by changing the blood concentration by the Allen's test. Light interaction with the skin was simulated with a Monte Carlo model, tuning the blood concentration parameter until the simulated and the measured spectra matched, yielding the relationship between the skin colour and the blood concentration.
Results: The simulation produced spectra similar to those measured. The change in the blood concentration in the simulation model and in the skin produced changes similar to the spectra. The reflectance of the skin was found to be a nonlinear function of the blood concentration.
Conclusion: The relationship found between skin colour and blood concentration makes it possible to quantify those skin conditions expressed by blood volume better than plain colour.

Key words: spectrophotometry – medical imaging – colour vision – haemodynamics – skin imaging – dermatology – Monte Carlo simulation

Accepted for publication 23 January 2010

THE SKIN is the largest organ of a human being. Still, it is only several millimetres thick and its surface is easily accessible everywhere. The combination of thinness and low optical absorption and sufficient scattering allows visible light to penetrate deep into the skin and scatter back to its surface. The skin reacts to many kinds of local and global stimuli by adjusting the perfusion and thus its blood volume. Injuries and other disorders may also permanently change the physical structures of the skin and bring additional chromophores into the injured area. These changes affect both the scattering coefficient and the absorption spectra of the skin, which can be seen as a difference in colour on the surface. The human colour vision may have been especially adapted to observe changes in skin colour (1). Still, the interpretation of the colour sensation is always subjective and it is better in providing qualitative than quantitative measures (2). Therefore, machine vision provides essential improvements to colour-based skin analysis. Noninvasive optical measurements are a convenient method to obtain information on the state of the human skin. It may help in diagnosing and following up various skin disorders and other diseases that may manifest as changes in the appearance of the skin (3).

The reason why optical measurements are not used more is that the relation between the skin structure and chromophore concentrations is extremely complicated. The optics of the skin have been studied perhaps for a century. A recently published review (4) covers many areas of the topic and so does Baranoski and Krishnaswamy in (5). Although the colours of the skin chromophores are well known (6–8), the light interaction with skin is so complicated that it cannot be completely solved mathematically, but merely approximated with suitable simplifications. Several simplifications have been used

to model light behaviour in skin, Kubelka–Munk theory, diffusion theory and Monte Carlo multilayer (MCML) simulation being the most regularly used. The MCML simulation is the most accurate, but it may often be inconvenient and slow.

Tsumura et al. (9, 10) and Claridge et al. (11) suggest that the possible normal skin colour spans a two-dimensional space in the three-dimensional colour space. Therefore, the skin colour can be mostly described by the absorbance of melanin and the absorbance of haemoglobin alone. This model may be accurate when producing different skin colours but these axes are not directly relational to the pigment concentrations, even in the logarithmic space, due to the non-linear nature of skin. Takiwaki et al. (3) measured the spectra of many skin disorders and compared the spectra with normal skin colour. They concluded that the spectral difference in absorbance (SDA) yields useful information about skin disorders. They were able to show that the levels and the shapes of the SDA spectra correlate with the melanin and haemoglobin levels. Yet, the exact shapes and values of the SDA profiles due to haemoglobin- and melanin-level changes are still unknown. Further research is needed to gain a better understanding of the relationships of the reflectance and the skin structure and chromophore concentrations.

There are several sensors that are suitable for spectrophotometric measurements and imaging. Imaging sensors that are based on tri-stimulus or monochromatic sensors are often more affordable and easier to use than actual spectrophotometric cameras. The estimation of skin chromophores does not require excessive number of wavelengths, as each chromophore has a smooth spectrum in the VIS-NIR range (6–8). The sensitivity curves of the sensors and the geometries of the light source and the detector influence the measurements (12). These factors need to be carefully examined to provide more accurate measurements.

In this article, the relationships between skin chromophore concentrations and skin colour are examined in spectral and in three tri-stimulus colour domains. The examination is based on a simulation model similar to the one used in (13, 14). The results of the simulations are compared with spectrophotometric measurements during five Allen's tests performed on 20 persons.

Materials and Methods

Skin reflectance measurement

To measure the reflectance of the skin, it is illuminated with a light source, whose intensity at each wavelength, λ, is $E(\lambda)$. The reflectance of the skin $R(\lambda)$ describes the skin property to remit back the incident light. The remitted light is measured with a sensor, whose sensitivity is $S(\lambda)$. The response, v, of the measurement system is therefore

$$v = \int S(\lambda)E(\lambda)R(\lambda)d\lambda \qquad (1)$$

The bandwidth of the sensor $S(\lambda)$ and the illumination spectra $E(\lambda)$ determine the characteristics of the measurement.

The spectral measurement system measures several narrow band channels. The bandwidths of these channels use either narrowband light sources or narrowband sensors. To record n pure reflectances, R_n, the characteristics of the channel are compensated by calibrating the values with the values of the known reflectance R_w, usually a reference white:

$$R_n = \frac{\int S_n(\lambda)E_n(\lambda)R(\lambda)}{\int S_n(\lambda)E_n(\lambda)R_w}R_w \qquad (2)$$

The bandwidth of the light source and the detector together defines the bandwidths of each channel. The measured reflectance of the channel is the weighted average of the reflectance of the sample within the channel bandwidth. The observation of narrow reflectance peaks or notches requires many narrow channels, whereas fewer and wider bands are sufficient if the spectrum is smoother, which is the case in this study.

Tri-stimulus values

The spectral sensors, which mimic human colour vision, are common and easily affordable. Even though the channel bandwidths of these tri-stimulus sensors are wide, they are in many cases satisfactory for skin analysis, as the chromophores in skin have quite smooth spectra.

The human eye has receptors, called cone cells, for short, middle and long wavelengths. Thus, in principle, three parameters are enough to approximate a colour sensation. The tri-stimulus values of a colour are the amounts of three primary colours in a three-component additive colour model needed to match that test colour.

The tri-stimulus values are most often given in the CIE 1931 colour space, in which they are denoted by X, Y and Z (15).

Any specific method for associating tri-stimulus values with each colour is called a colour space. CIE XYZ, one of many such spaces, is special because it is based on direct measurements of human visual perception, and serves as the basis from which many other colour spaces are defined.

The responses of the channels of the tri-stimulus sensors mimic human colour vision and thus approximate the three CIE standard colourimetric observer (SCO) curves.

$$X = \int_{380}^{680} x(\lambda)E(\lambda)R(\lambda)d\lambda \quad (3)$$

$$Y = \int_{380}^{680} y(\lambda)E(\lambda)R(\lambda)d\lambda \quad (4)$$

$$Z = \int_{380}^{680} z(\lambda)E(\lambda)R(\lambda)d\lambda \quad (5)$$

where $x(\lambda)$, $y(\lambda)$ and $z(\lambda)$ are the CIE SCO curves (15), and X, Y and Z are the resulting colour values in the XYZ space.

The XYZ colour values can be further transformed to other tri-stimulus colour spaces, such as RGB and CIE-$L^*a^*b^*$, using matrix transformations and additional nonlinear gamma correction for RGB.

The skin model

The model used in Välisuo and Alander (13) was used in this study too. It is shown in Fig. 1.

The model consists of the model structure and its model parameters. The parameters of each layer are the absorption coefficient, the scattering coefficient and the anisotropy. To be able to estimate the absorption coefficients, the skin chromophores and their concentrations are needed. The chromophores in the skin are either deposited in skin cells or are carried with blood. The concentrations of chromophores in blood vary with the blood fraction, while the concentration of the chromophores deposited in skin cells remains rather constant in time. The most important chromophores of the skin are haemoglobin and melanin. Bilirubin and β-carotene may have a significant effect too. Water has significant effect for wavelengths longer than 800 nm, but it does not influence the skin colour.

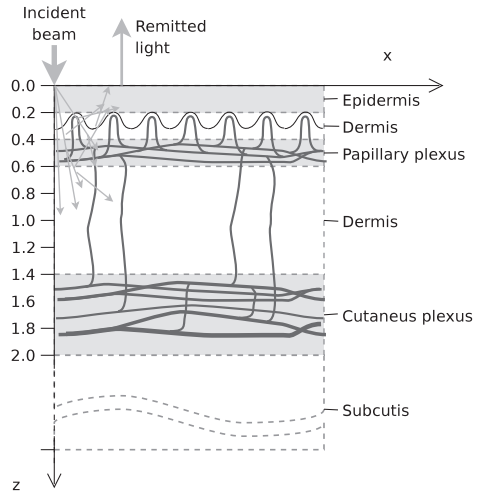

Fig. 1. The model of the skin. The names of the layers are on the right-hand side. The left-hand side displays depths, z, from the skin surface in mm.

TABLE 1. Blood fractions

Layer	Layer name	Nominal blood fraction, f_i
1	Epidermis	0
2	Dermis	0
3	Papillary plexus	0.0556
4	Dermis	0.0417
5	Cutaneous plexus	0.2037
6	Subcutis	0.0417

The blood fractions in the skin layers when the total blood fraction $f_0 = 0.5$.

The absorption of the plain skin, without haemoglobin, melanin and other skin chromophores, is called the skin baseline. The baseline measured by Saidi was used here (16).

The absorption spectra of haemoglobin are described by Horecker in (8) and tabulated by Prahl in (7). Both oxygenated haemoglobin and deoxygenated haemoglobin spectra were used. An oxygen saturation level of 0.70 and a nominal haemoglobin concentration value of 150 g/L or 2.33 mmol/L were assumed. The blood distribution in different skin layers, described by Reuss (17), was used. It is presented in Table 1. The absolute blood concentration in each layer is achieved by multiplying f_i with the blood fraction in the total tissue volume f_0. Reuss reported f_0 values from 0.015 to 0.05.

A formula for reproducing the absorption spectra of melanin is suggested by Jacques in

(18). This formula was also used here as well as Prahl's formula for approximating Mie and Rayleigh scattering in skin.

The spectra of bilirubin and β-carotene are included in the Photochemcad software (19). The normal concentration of total bilirubin in blood is between 5 and 25 μmol/L.

Allen's test

The simulations were validated by measuring the *in vivo* skin spectra from the palm of the hand during Allen's test (20). The HR4000 spectrometer and the ISP-REF integrating sphere (Ocean Optics Inc., Dunedin, FL, USA) were used in the measurements.

The palm of the hand has a rich vascular network and a very low concentration of melanin. Allen's test is normally used to test the patency of ulnar circulation, when harvesting of the radial artery is planned. In this experiment, we used Allen's test to alter the skin's blood volume and to measure the vascularity-related changes in skin spectra. For this purpose, 20 healthy volunteers (ages 20–39), six males and 14 females, with Fitzpatrick skin types I–IV, were enrolled in the study. The experiment was started by performing Allen's test in which both ulnar and radial arteries were occluded at the wrist level by manual compression, and the blood was pumped out from the palm by clenching and unclenching the hand several times. Then, with minimal blood concentration in the skin, the spectra were measured, and while releasing compression of both arteries leading to rapid inflow of blood to the hand, the skin spectra were recorded approximately every 0.55 s until the maximum blood concentration in the skin was reached. This resulted in 10 spectral images from the beginning to the end of each measurement with different degrees of haemoglobin concentrations. The measurements were taken from five different reference points of the right palm, shown in Fig. 2, of each volunteer, adding up to 100 measurements altogether. The experiment was performed in normal room temperature and humidity.

Results

The concentrations of the skin chromophores in the simulation and their reference values are given in Table 2.

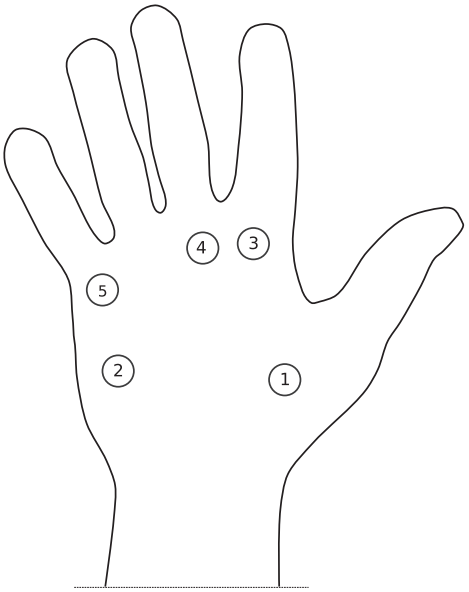

Fig. 2. The measurement locations in the right palm.

TABLE 2. Chromophore concentrations

Parameter	Value	Reference value
Melanin	$f_M = 0.012$	[0, 0.05]
Total blood	$f_0 = [0.0016, 0.0045]$	[0.015, 0.05]
Oxysat	0.70	[0.2, 1]
Haemoglobin	$C_{HB} = 2.33$ mmol/L	2.33 mmol/L
Bilirubin	$C_{Br} = 10$ μmol/L	<[5, 25] μmol/L
β-carotene	$C_{BC} = 2$ μmol/L	[1, 4] μmol/L

Skin chromophore concentrations in the simulation model.

The absorbance of the skin in green ($\lambda =$ 522 nm) during Allen's test, as a function of time, is shown in Fig. 3. The reflectance of green in the skin decreased to approximately one-third during Allen's test. Then the normal blood volume was retained within 1 s. The curve in the middle represents the median values of all 100 measurements. The topmost line is the 75% percentile and the lowest curve is the 25% percentile.

The simulated and measured reflectance spectra of skin during the Allen's test are shown in Fig. 4. The topmost line shows the reflectance in the beginning, when the blood volume is the smallest. The other curves from the top to bottom correspond to measured and simulated spectra after 1.1, 1.65 and 4.95 s after artery release.

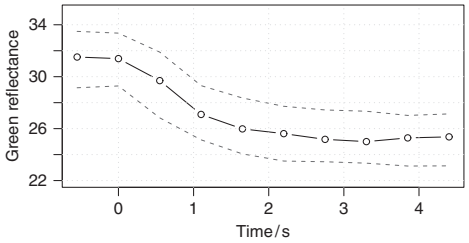

Fig. 3. The median reflectance of skin in green (λ = 522 nm) during Allen's test is shown as a continuous line. Dashed lines show the 25% and 75% percentiles.

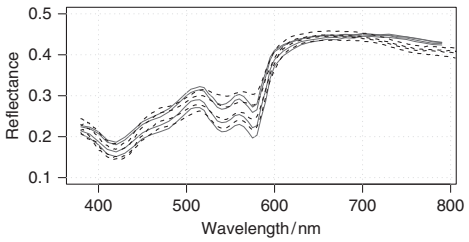

Fig. 4. The measured (continuous line) and simulated (dashed line) skin reflectance spectra during Allen's test, after approximately 0, 0.5, 1 and 5 s after the release of the arteries.

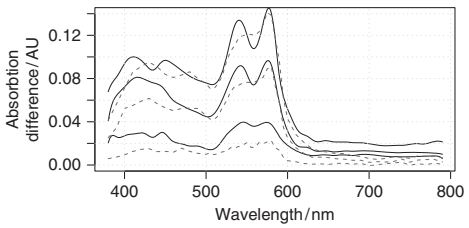

Fig. 5. The measured (continuous line) and simulated (dashed line) difference of the skin absorption spectra with different total blood fractions, f_0.

The SDA spectra shown in Fig. 5 were obtained by subtracting the spectra measured in the beginning of Allen's test from the spectra measured 1.1, 1.65 and 4.95 s after arterial release. The SDA spectra calculated from the corresponding simulated spectra are also shown.

The root mean square (RMS) differences of the simulated spectra, corresponding to the observed spectra at different times during Allen's test, can be mostly explained by different blood concentrations, as shown in Fig. 6. The total blood fractions that make the simulated spectra match

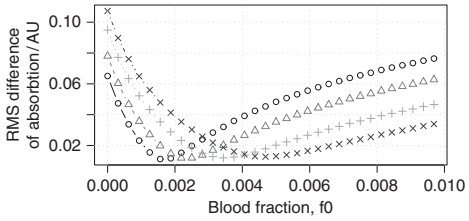

Fig. 6. The root mean square difference between the simulated reflectance spectra and the observed reflectance spectra when the observed spectra are measured after ∘ *= 0,* Δ *= 0.5, X = 1 and + = 5 s after artery release.*

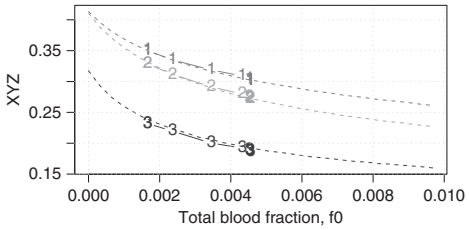

Fig. 7. XYZ reflectance values (1 = X, 2 = Y and 3 = Z) as a function of total blood fraction (dashed line) vs. measurement results (continuous line).

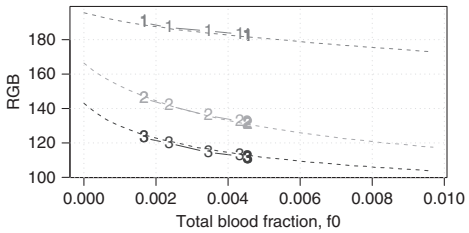

Fig. 8. The RGB values (1 = red, 2 = green and 3 = blue) of skin reflectance with different total blood fractions (dashed line) vs. measurement results (continuous line).

closest to the observed spectra are: $f_0 = \{0.16\%, 0.23\%, 0.034\%, 0.45\%\}$.

Figures 7–9 show the different tri-stimulus values as a function of blood volume. The blood fractions for measured values are those minimizing the RMS differences, as reported above. The *XYZ* values are calculated from the measured and the simulated reflectance spectra using Eqs (3)–(5). The sRGB values are obtained from the *XYZ* values using a linear transformation and by applying a γ correction. The curves in Fig. 9 are obtained by using a narrow band, red, green and blue LEDs instead of CIE SCO curves as sensor channels.

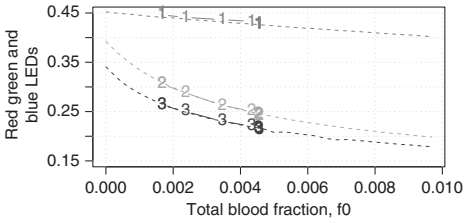

Fig. 9. The reflectance values of (1 = red), (2 = green) and (3 = blue) LEDs with different total blood fractions (dashed line) vs. measurement results (continuous line).

Conclusion and Discussion

The exact knowledge of the relationship between skin blood concentration and its spectra is important when quantifying the intensity of different skin lesions. An increase in vascularity occurs in erythema and also scars. The subjective colour assessment scales and the commercial equipment used in colour measurement assume that the colour change related to increase of haemoglobin in the skin follows a linear model (21). The measurements and simulations in this work show the dependence between the skin reflectance spectra and the blood concentration. The RGB or other tri-stimulus values can be calculated from the reflectance spectra to show how the skin colour depends on the blood concentration. As seen in the results of Allen's test and the simulation model, the skin colour does not linearly follow the blood concentration changes. When the blood concentration is high, further increase has less effect on the colour intensity than when the concentration is low. Based on this knowledge, the intensity of different hyperaemic conditions, especially scars, should be expressed in terms of the relative haemoglobin concentration in the skin rather than the mere intensity of colour.

The simulated skin spectra approximate the measured spectra in the whole visual range, $\lambda \in [380,780]$ nm. The simulation model can be tuned to match to all the spectra measured in Allen's test by tuning only the blood concentration in the simulation model. The RMS error between the simulated and the measured spectra is below 0.013 in all cases. Potentially, the simulation model also holds outside the validated region.

Takiwaki and colleagues measured SDA spectra from different skin lesions and assumed that the main difference between certain lesions is the different blood concentration. The SDA spectra shown in Fig. 5 are similar, but in this work, it is known that the only difference in the skin was the blood concentration. The SDA of the simulated spectra also agrees satisfactorily with the measured SDA, after a suitable amount of bilirubin was added to the model. The SDA spectra of Allen's test have potential in investigating whether certain chromophore is mixed in the blood or deposited in the skin, because a change in the total blood fraction also changes the concentrations of all the pigments in blood. This change is seen as a peak in the SDA spectra. If the pigment is deposited in the skin, the SDA spectra are flat.

The parameters of the model correspond mainly to those mentioned in the previous work. The absolute value of the blood concentration in skin is not very well known and it varies widely between persons, skin regions and time. The total blood fraction, f_0, was from 0.16% to 0.45%, while it was from 1.5% to 5% in the previous work (17). The nominal concentrations of bilirubin and β-carotene are so small that they did not seem to have any measurable effect on the skin colour if they are only in blood. Therefore, it was assumed that the concentration of these pigments in the skin is equal to the concentration in blood. This assumption helped to construct the simulation model to match with the measured spectra using bilirubin and β-carotene concentrations, which are in the middle of their reference minimal and maximal values. The spectra of bilirubin and β-carotene are so close to each other that it is difficult to separate them from each other.

More research is needed to tune the model to match with the measurements even further. More work is also needed to validate the model in the larger range.

Acknowledgements

We would like to express our gratitude to Oy Abilita Ab, TEKES and the Finnish Cultural Foundation The South Ostrobothnia Regional Fund for financing this work.

References

1. Changizi M, Zhang Q, Shimojo S. Bare skin, blood and the evolution of primate colour vision. Biol Lett 2006; 2: 217–221.

2. Nedelec B, Correa JA, Rachelska G, Armour A, LaSalle L. Quantitative measurement of hypertrophic scar: intrarater reliability, sensitivity, and specificity. J Burn Care Res 2008; 29: 489–500.
3. Takiwaki H, Miyaoka Y, Arase S. Analysis of the absorbance spectra of skin lesions as a helpful tool for detection of major pathophysiological changes. Skin Res Technol 2004; 10: 130–135.
4. Igarashi T, Nishino K, Nayar S. The appearance of human skin: a survey, volume 3 of foundations and trends in computer graphics and vision. Now Publishers Inc., 2007.
5. Baranoski GVG, Krishnaswamy A. Light interaction with human skin: from believable images to predictable models. In: SIGGRAPH Asia '08: ACM SIGGRAPH ASIA 2008 courses. New York, NY, USA: ACM, 2008: 1–80.
6. Zijlstra WG, Buursma A, van der Meeuwsen R. Absorbtion spectra of human fetal and adult oxyhemoglobin, de-oxyhemoglobin, carboxyhemoglobin and methemoglobin. Clin Chem 1991; 37: 1633–1638.
7. Prahl S. Optical absorption of hemoglobin. Oregon: Oregon Medical Laser Center, 1999. Available at http://omlc.ogi.edu/spectra/hemoglobin/index.html (accessed 31 January 2008)
8. Horecker BL. The absorbtion spectra of hemoglobin and its derivatives in the visible and near infra-red regions. J Biol Chem 1942; 148: 173–183.
9. Tsumura N, Haneishi H, Miyake Y. Independent-component analysis of skin color image. J Opt Soc 1999; 16: 2169–2176.
10. Tsumura N, Kawabuchi M, Haneishi H. Mapping pigmentation in human skin by multi-visible-spectral imaging by inverse optical scattering technique. In: 8th IS&T/SID Color Imaging Conference. Scottsdale, AZ, USA, 2000.
11. Claridge E, Cotton S, Hall P, Moncrieff M. From colour to tissue histology: physics based interpretation of images of pigmented skin lesions. MICCAI 2002; 1: 730–738.
12. Takiwaki H. Instrumental quantification and its clinical application in the future. Skin Res Technol 2002; 8: 94–97.
13. Välisuo P, Alander J. The effect of the shape and location of the light source in diffuse reflectance measurements. *21st IEEE Int Symp Comput Based Med Syst* Jyväskylä, Finland, 2008: 81–86.
14. Välisuo P, Mantere T, Alander J. Solving optical skin simulation model parameters using genetic algorithm. *The 2nd International Conference on BioMedical Engineering and Informatics*, Tianjin, China 2009.
15. CIE. Commission internationale de l'Eclairage proceedings. Cambridge: Cambridge University Press, 1931.
16. Saidi IS. Transcutaneous optical measurement of hyperbilirubinemia in neonates. PhD thesis, Rice University, Houston, USA, 1992.
17. Reuss JL. Multilayer modeling of reflectance pulse oximetry. IEEE Trans Biomed Eng 2005; 52: 153–159.
18. Jacques SL, McAuliffe DJ. The melanosome: threshold temperature for explosive vaporization and internal absorption coefficient during pulsed laser irradiation. Photochem Photobiol 1991; 53: 769–775.
19. Du H, Fuh RA, Li J, Corkan AL, Lindsey JS. PhotochemCAD: a computer-aided design and research tool in photochemistry. Photochem Photobiol 1998; 68: 141–142. Available at http://dx.doi.org/10.1111/j.1751-1097.1998.tb02480.x.
20. Asif M, Sarkar PK. Three-digit Allen's test. Ann Thorac Surg 2007; 84: 686–687.
21. Draaijers LJ, Tempelman FRH, Botman YAM, Kreis RW, Middelkoop E, van Zuijlen PPM. Colour evaluation in scars: tristimulus colorimeter, narrow-band simple reflectance meter or subjective evaluation? Burns 2004; 30: 103–107.

Address:
Petri Välisuo
Department of Electrical Engineering and Automation
University of Vaasa
Wolffintie 34
65320 Vaasa
Finland
Tel: +358 445 804 320
Fax: +35 863 248 677
e-mail: petri.valisuo@uwasa.fi

Publication IV

Kaartinen, I. S., Välisuo, P. O., Bochko, V., Alander, J. T. & Kuokkanen, H. O. (2011b). How to Assess Scar Hypertrophy? A Comparison of Subjective Scales and Spectrocutometry – A New Objective Method. *Wound Repair and Regeneration*, 19: 2.

Wound Repair and Regeneration

How to assess scar hypertrophy—a comparison of subjective scales and Spectrocutometry: A new objective method

Ilkka S. Kaartinen, MD[1]; Petri O. Välisuo, MSC[2]; Vladimir Bochko[2]; Jarmo T. Alander[2]; Hannu O. Kuokkanen, MD, PhD[1]

1. Department of Plastic Surgery, Tampere University Hospital, Tampere, Finland, and
2. Department of Electrical and Energy Engineering, University of Vaasa, Vaasa, Finland

Reprint requests:
Ilkka S. Kaartinen, Department of Plastic Surgery, Tampere University Hospital, PO Box 2000, FI-33521 Tampere, Finland.
Tel: +3583 3116 6019;
Fax: +358 33116 5836;
Email: ilkka.kaartinen@pshp.fi

The study has been presented at the ECSAPS meeting in September 17 in Helsinki, Finland.

Manuscript received: August 27, 2010
Accepted in final form: January 27, 2011

DOI:10.1111/j.1524-475X.2011.00679.x

ABSTRACT

Scar hypertrophy is a significant clinical problem involving both linear scars from elective surgery and scars caused by trauma or burns. The treatment of hypertrophic scars is often time consuming, and patients may need to be followed up for months or even years. The methods for reliable quantification of scar hypertrophy are at present unsatisfying. We have developed a new, objective method, Spectrocutometry, for documentation and quantification of scar hypertrophy. The instrument is based on standardized digital imaging and spectral modeling and calculates the estimated concentration change of hemoglobin and melanin from the entire scar and also provides standardized images for documentation. Three plastic surgeons have assessed 37 scars from melanoma surgery using Spectrocutometry, the Vancouver scar scale, and the patient and observer scar assessment scale. The intraclass correlation coefficient for the Vancouver scar scale and the patient and observer scar assessment scale was lower than required for reliable assessment (r=0.66 and 0.60, respectively). The intraclass correlation coefficient for Spectrocutometry was high (r=0.89 and 0.88). A Bayesian network analysis revealed a strong dependency between the estimated concentration change of hemoglobin and scar pain. Spectrocutometry is a feasible method for measuring scar hypertrophy. It is shown to be more reliable than subjective rating in assessing linear surgical scars.

The process of scar healing is poorly understood. It is known that wounds close under excess tension and, on the other hand, many traumatic wounds, especially burns, are prone to develop hypertrophy.[1,2] Hypertrophic scars (HSs) pose a significant clinical problem.[3] The incidence of postsurgical scar hypertrophy varies between 5 and 44.6% in different studies and among different ethnic populations, with greater risk for developing scar hypertrophy among the more pigmented populations.[4] The rate of postburn scar hypertrophy is found to be even higher because of the larger surface area of the scar.[5]

HSs are managed with a combination of different treatment modalities including both conservative and surgical treatments.[6,7] In the prevention and treatment of HSs, the role of reliable scar assessment in documentation and follow-up is of paramount importance.[8]

One of the essential problems concerning scar treatment and research is the lack of objective instruments to assess and quantify scar hypertrophy. In a clinical setting, this complicates the follow-up of individual patients with HSs; often, there are several professionals who treat the patient, and a precise follow-up of the scars activity would be needed to guide the treatment decisions. In the field of research, where new methods to treat and to prevent scar formation are being developed, objective quantitative instruments are essential.

The number of different observer-based rating scales is vast and new scales are regularly introduced. The Vancouver scar scale (VSS) has been used in studies in both burn scars and linear scars and the patient and observer scar assessment scale (POSAS) has been designed to rate linear scars.[9] Additionally, the Manchester scar scale (MSS) was introduced by Beausung and colleagues, and Duncan proposed the use of the visual analogue scale (VAS) in scar assessment.[10,11]

In the majority of recently published scar studies, subjective evaluation with the VSS has been used as an endpoint.[12] Despite its poor reliability, subjective assessment is considered the "gold standard" in scar assessment.[9,13] This reflects the lack of suitable quantitative methods.

Spectrophotometry has been used for color measurement for over 50 years. In previous studies, it has also been used to measure the color of scars and other skin disorders.[14–16] We have developed an optical instrument for scar assessment, which combines standardized digital imaging (SDI) and spectral modeling (SpM). The color change in scars is caused by variations in hemoglobin and melanin concentrations.[17] The absorbance spectra of these chromophores are well known.[18] From the spectral images, the estimated concentration change (ECC) of melanin and hemoglobin between the scar tissue and adjacent healthy skin can be calculated from the entire scar.[19] This information, especially the quantitative estimation of hemoglobin concentration, is a good indicator of the scar's activity and appearance. At the same time, the method also provides standardized digital images for

documentation and follow-up. We have used this method previously in assessing skin graft donor site scars, and the results have been published in *Burns* journal.[20]

In this study, we have assessed 37 surgical scars after melanoma surgery. The wounds after melanoma excision are often closed with some degree of tension and exhibit more or less hypertrophy, while scars after a sentinel lymph node biopsy and lymphadenectomy usually heal better. This gives us a variation of scars with none to marked hypertrophy. Three plastic surgeons have examined these scars individually using the VSS and the POSAS scar scales and, in addition, the proposed spectrocutometry method described in detail later. This study compares the reliabilities and validity of the different scar assessment methods.

Patients

The patient group in the study included 20 patients (12 males, eight females) who have undergone melanoma surgery in Tampere University Hospital between August 2007 and November 2009. In the study, 37 scars were assessed, including 22 excision scars, 12 sentinel lymph node biopsy scars, and five lymphadenectomy scars. The mean age of the patients was 57 ± 16.9 years and the mean time from melanoma surgery was 17 months (4–30, SD $\pm$ 7.4). All the patients were examined during the same day in the outpatient clinic. Permission for the study was obtained from the Ethical Board of Pirkanmaa Health Care District. A written informed consent was given by all the participants.

MATERIALS AND METHODS

Subjective assessment

The scars were evaluated individually by three plastic surgeons, the corresponding author and two other plastic surgeons from our department serving as independent observers. The assessment was performed under similar lighting in a temperature-controlled room. The VSS (Table 1) and POSAS (Tables 2 and 3) scales were used for rating of each scar. The patients also filled the POSAS patient questionnaire of the corresponding scars.

Image acquisition and reflectance measurement

The digital images of the scars were acquired with the same imaging system as used in our earlier research.[20] The imaging system consists of a camera, a protective cover, and a computer-controlled lighting system (Figure 1). The camera is a digital single lens reflex camera, Fuji IS Pro (Fujifilm Corporation, Tokyo, Japan). The cover protects the target from exterior light and preserves the distance and the angle of the camera constant. The lighting system illuminates the target with reproducible, optimized light. The characteristics of the light source and the camera are obtained by imaging a white reference object. The reflectance of the skin is calculated from the acquired color image by scaling the color image with the image of the white reference in the same illumination. The color precision of the original raw images is 12 bits. All arithmetic operations are calculated using 16-bit precision. The resolution of the apparatus used in the study is 225 pixels/mm.[2] In a study by Välisuo et al.,[21] the accuracy of this imaging system in reflectance measurement was found to be similar to that obtained with a spectrophotometer.

Table 1. Vancouver scar scale

Parameter	Descriptor	Points
Vascularity	Normal	0
	Pink	1
	Red	2
	Purple	3
Pigmentation	Normal	0
	Hypopigmentation	1
	Hyperpigmentation	2
Pliability	Normal	0
	Supple	1
	Yielding	2
	Firm	3
	Banding	4
	Contracture	5
Height	Normal (flat)	0
	> 0 and < 2 mm	1
	≥ 2 and < 5 mm	2
	> 5 mm	3
Total score		/13

Spectral modeling

The concentrations of melanin and hemoglobin were calculated from the reflectance values using similar spectral modeling as in our earlier research.[19] We have calculated the ECC values of hemoglobin and melanin, which means the measured change in the concentration of these chromophores between the scar and the adjacent healthy skin. The main principle of this SpM is the partition of the observed reflectance change into two components, the first corresponding to hemoglobin and the second to melanin concentration change. The rest of the color change, which

Table 2. The POSAS scale observer component

	Normal skin									Worst scar imaginable
	1	2	3	4	5	6	7	8	9	10
Vascularization	O	O	O	O	O	O	O	O	O	O
Pigmentation	O	O	O	O	O	O	O	O	O	O
Thickness	O	O	O	O	O	O	O	O	0	O
Relief	O	O	O	O	O	O	O	O	O	O
Pliability	O	O	O	O	O	O	O	O	O	O

POSAS, patient and observer scar assessment scale.

Table 3. The POSAS scale patient component

	No, not at all									Yes, very much
	1	2	3	4	5	6	7	8	9	10
Is the scar painful?	O	O	O	O	O	O	O	O	O	O
Is the scar itching?	O	O	O	O	O	O	O	O	O	O

	No, just like normal skin									Yes, very different
	1	2	3	4	5	6	7	8	9	10
Is the scar color different?	O	O	O	O	O	O	O	O	O	O
Is the stiffness of the scar different?	O	O	O	O	O	O	O	O	O	O
Is the thickness of the scar different?	O	O	O	O	O	O	O	O	O	O
Is the scar irregular?	O	O	O	O	O	O	O	O	O	O

POSAS, patient and observer scar assessment scale.

cannot be explained by hemoglobin and melanin change, is the residual.[20]

The images were segmented in three areas: the scar, normal skin, and the rest, including skin disorders, shadows, and foreign objects (hairs, clothes, shadows, etc.).[22] The concentration of melanin and hemoglobin was estimated for each pixel of the scar, and the ECC values were obtained by comparing the mean estimated concentration of the scar and the adjacent healthy skin.

Objective assessment

Each observer used the instrument described above to take one digital image of each scar (Figure 2). After taking the image, the observer checked the calibrated picture from the computer screen for approval. If the observer was not satisfied with the quality of the image, another image was immediately taken to replace the disapproved one until an acceptable image was gained. In most cases, only one picture was needed for approval. As the camera has an incorporated lighting device, the images were shot without any additional lighting. Two parameters were calculated from the spectral images: the ECC of hemoglobin and melanin.

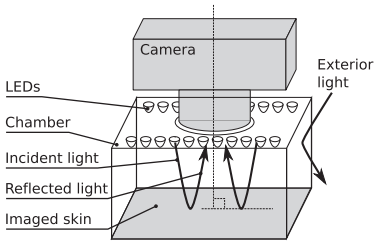

Figure 1. Standardized digital imaging system, picture modified from Zijlstra et al.[18]

Statistical analysis

Statistical analysis was performed using SPSS software version 17.0 (SPSS Inc., Chicago, IL) and R software. The interrater reliability of the measurements between the three observers was calculated using the intraclass correlation coefficient (ICC). The two-way random effect model and consistency type was used in the ICC calculations. The reliability was assessed for both a single measure and average measures including 95% confidence intervals (CI). In this way, the ICC values for single measures indicate the reliability of the ratings of a random set of observers on a single target. The ICC values for average measures, on the other hand, indicate the reliability of the mean ratings of the observers in the target group. The ICC for average measures is always higher than ICC for single measures, but the ICC for single measures is the more relevant measure when testing an instrument designed for use in clinical practice.[23]

When judging the reliability of an instrument, an ICC value of $\geq$0.75 is often considered some kind of a threshold for a reliable instrument, although one must also take into account the CIs. The number of observers needed to achieve a rating with an ICC value of $\geq$0.75 was calculated.

Concurrent validity between the objective and the subjective assessments was analyzed using Pearson's correlation coefficient. To show how the observations and scores depend on each other, the dependency of the overall POSAS and VSS scores of the individual parameters was studied. The Pearson's correlation coefficient, r, can be used for measuring linear and Spearman's correlation coefficient, ρ, for nonlinear monotonic dependencies. Automatic relevance determination (ARD) can also measure nonmonotonic dependencies.[24] Here, the dependencies were first analyzed by constructing a Bayesian network from the data, using the B-Course tool.[25–27] The Bayesian network is a graphical representation of the dependencies between variables, including linear, nonlinear, and also nonmonotonic dependencies. The dependencies shown by the network were checked by calculating r and ρ for all the arcs of the graph. If there was no correlation, the dependency was checked using ARD, too.

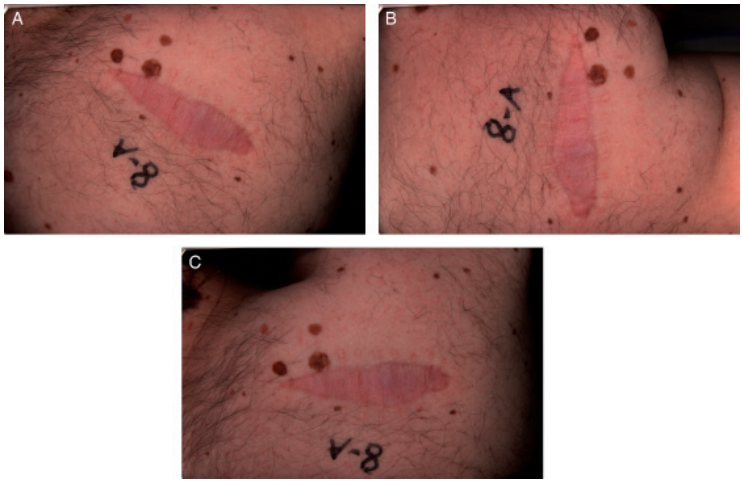

Figure 2. (A-C) Three images from the same scar taken individually by the observers (A, B, C) using standardized digital imaging. The distance and angle of the camera and the lighting remain the same; only the rotational angle around the optical axis may vary as can be seen.

RESULTS

Interrater reliability

The ICCs for subjective and objective ratings are shown in Table 4. The objective measurement for the ECC of melanin and hemoglobin showed high reliabilities for both single and average measurements with very narrow CIs. A single observer could perform the measurement for both parameters reliably.

Both the POSAS and the VSS achieved reliability ratings below the acceptable limit (r=0.60 and 0.66 $p < 0.001$). The number of observers needed to perform a reliable subjective assessment (ICC > 0.75) with these scales was on average four observers for the VSS and five observers for the POSAS.

Concurrent validity

The correlations between the ECC values and the subjective ratings for the corresponding parameters are shown in Table 5. There was a statistically significant correlation between the ECC values for melanin and hemoglobin and the subjective ratings for vascularity and pigmentation with both scales. The correlation between ECC of melanin and POSAS pigmentation rating was slightly higher than the correlation between the vascularity measurements (r=0.68 and 0.50, respectively). However, it must be noted that the subjective ratings for vascularity do not give measures below zero, whereas the ECC values in some scars achieved a negative measure, indicating that the scar has less hemoglobin than the surrounding normal skin.

Dependency analysis

The dependencies shown in the Bayesian network in Figure 3A are mostly linear and monotonic, as they have a high Pearson's correlation coefficient. The dependency of the overall POSAS score on ECC of hemoglobin is an exception. The r and ρ are low, but the α shows almost as strong a dependency as between VSS height and the

Table 4. ICCs of ratings

	Average measures	Single measures	95% CI	p
Subjective assessments				
POSAS	0.821	0.604	0.69–0.90	< 0.005
VSS	0.855	0.662	0.749–0.92	< 0.005
Spectrocutometry				
ECC of melanin	0.959	0.886	0.928–0.978	< 0.005
ECC of hemoglobin	0.955	0.875	0.920–0.976	< 0.005

The intraclass correlation coefficients (ICC) of subjective ratings and spectrocutometry measurements including the 95% confidence intervals (CI) of average measures and their p-values.
ECC, estimated concentration change; POSAS, patient and observer scar assessment scale; VSS, Vancouver scar scale.

Table 5. Concurrent validity

	r	*p*
ECC of melanin vs. POSAS pigmentation subscale	0.67	< 0.001
ECC of melanin vs. VSS pigmentation subscale	0.60	0.002
ECC of hemoglobin vs. VSS vascularity subscale	0.40	0.015
ECC of hemoglobin vs. POSAS vascularity subscale	0.50	< 0.001

The Pearson estimates (*r*) for correlations between the subjective ratings and spectrocutometry measurements.
ECC, estimated concentration change; VSS, Vancouver scar scale; POSAS, patient and observer scar assessment scale.

POSAS score. The α close to zero would have meant no dependency. Therefore, the dependency is true, but it is not monotonic.

The dependencies in the network can be interpreted as follows: the pliabilities of the POSAS and VSS scales are strongly dependent and correlated. The VSS overall score

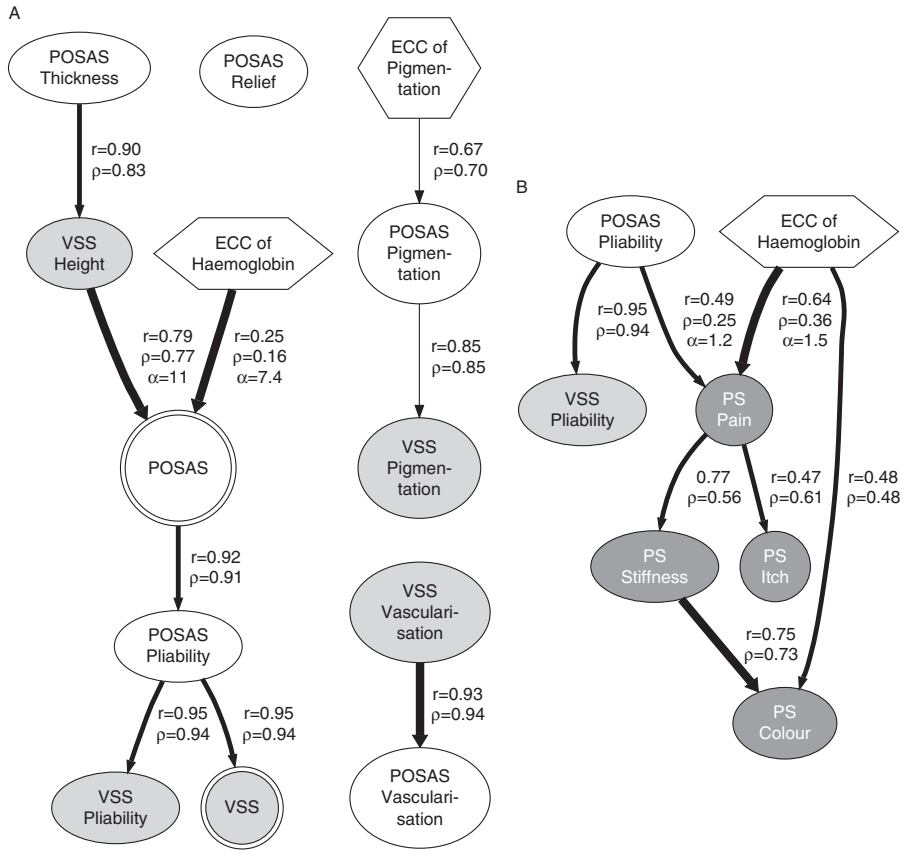

Figure 3. (A) Dependencies of the subjective ratings with the patient and observer scar assessment scale (POSAS) (white ellipses, and double circle for the overall score) and the Vancouver scar scale (VSS) (light gray ellipses, double circle for the overall score) and the spectrocutometry measurements (hexagons) of estimated concentration changes (ECC) of hemoglobin and melanin, (B) the dependencies of the patient score (PS, dark gray ellipses) values to the POSAS, the VSS, and the spectrocutometry values. The widths of the arcs show the strengths of the dependencies. Pearson (*r*) and Spearman (ρ) estimates and automatic relevancy determination (α) results are shown next to the corresponding arrows.

depends mostly on pliability, and to a lesser degree, the height, thickness, and ECC of hemoglobin. When pliability is measured, the other variables have no significance to the overall VSS score. Therefore, the overall VSS value can be calculated from the VSS pliability alone.

Similarly, the overall POSAS score can be calculated if thickness, ECC of hemoglobin, and pliability are known. Thickness can be replaced with VSS height estimate if that is available.

A similar network was constructed from the POSAS patient score (shown in Figure 3B). The patient estimate of scar color depends strongly on stiffness and moderately on ECC of hemoglobin. The patient opinion of pain is strongly dependent on ECC of hemoglobin and moderately on the observer ratings of pliability and patient rating of stiffness. Itching is dependent on pain. The rest of the dependencies were weak. These dependencies are mostly linear, as Pearson's correlation coefficient is also relatively high, but the patient opinion of pain does not strongly correlate with ECC of hemoglobin or observer pliability score. Therefore, the α of these dependencies was determined, too. The α shows that notwithstanding the low correlation, these dependencies are true and that the pain depends on the ECC of hemoglobin slightly stronger than on observer pliability rating.

DISCUSSION

Why is quantitative scar assessment needed? When treating HSs and keloids, quantitative information on the effect of designated treatments is essential. This is emphasized by the fact that the patient is often treated by several physicians and other professionals over time. Such a setting demands an instrument that has a high interobserver reliability.

Secondly, most scar treatments have not been properly tested by well-designed studies. Silicone gel sheeting may be the most widely used conservative method and has been used for over 20 years. Despite its wide use, it was stated in a Cochrane database review from the year 2008 that the evidence of silicone treatment is scarce and studies suggesting its use are susceptible to bias.[28] One reason for the lack of evidence is the fact that the majority of studies investigating scar treatments have been conducted using only subjective rating as an end point.[29,30]

In a recent study by Forbes-Duchart et al.,[31] it was noted that the majority of professionals treating burn scars do not use any instrument, subjective or objective, for scar assessment. In our experience, this makes it difficult to decide whether a treatment has been effective or not. Therefore, we believe there is a demand for a quantitative, objective, easy-to-use instrument for scar assessment both for scientific purposes and for clinical work.

Spectrophotometry has been tested in scar assessment in studies by Nedelec and colleagues and has also been used recently in a clinical study by Bloemen and colleagues.[32–34] The instruments used in these studies, the DermaSpectrometer® (Cortex Technology, Hadsund, Denmark), the Minolta Chromameter® (Minolta, Osaka, Japan), and the Mexameter® (Courage-Khazaka Electronic, Köln, Germany), supply quantitative information of scar color. The problem with these instruments is that they have narrow apertures (5–8 mm) and they can only give a result from a very limited part of the scar. Also, they do not provide an estimate of the concentration levels of the color chromaphores, hemoglobin and melanin, which cause the color change. A clear benefit of Spectrocutometry is that it can be used to measure the entire scar and its surroundings, yielding an average result of the concentration changes of hemoglobin and melanin compared with the healthy skin. This also minimizes the effect of the change in skin circulation between two measurements.

SIAscopy™ (Biocompatibles, Farnham, UK) is a newer innovation that provides more specific information than the previously mentioned spectrophotometers, as it quantifies the concentrations of hemoglobin, melanin, and collagen. SIAscopy™ gives a score of only a 24×24 mm or smaller area. It may be reliable when used to measure small scars, but is less useful when an average measurement of a larger scar is needed.

Various scar rating scales have been introduced in publications. The VSS is still the most popular and well-known alternative for scar assessment.[31] It is relatively easy to use, but many studies have found it to be too unreliable.[9] Our study makes no exception, and although the VSS showed slightly better reliability than the POSAS, it cannot be considered a reliable tool for clinical practice. Also, to incorporate it into a scientific study would require at least four observers, when calculated from the ICC results in this study, which is supported by findings in previous studies.[35]

The POSAS has been the rating scale of interest in recent years. Truong et al.[36] tested the reliabilities of both the POSAS and VSS in rating scars after breast cancer surgery. The ICC for single measures in their study was far from acceptable (r=0.54 and 0.33 for the VSS and the POSAS, respectively). In another study by the same authors, the ICC of the VSS for rating breast cancer surgery scars was 0.64 (0.51–0.74, 95% CI), which is comparable with the levels found in our study, and cannot be considered sufficient.[37] In a study by Draaijers et al.,[38] the POSAS scale showed better interrater reliability, with an ICC of 0.73 for single measurements. It can be stated that standardized training can increase the reliability of subjective scar rating and may produce a better outcome in reliability studies than shown in our study. However, in the study presented here, there was no training involved in the use of the proposed Spectrocutometry method, which still achieved acceptable reliability.

The B-Course tool reveals an interesting aspect of scar assessment, especially with the POSAS scale. The overall score is dependent on only two parameters, the thickness and pliability, while other parameters are independent. Also, the only significant dependency between the patient and the observer scores is between pliability and scar pain. These results indicate that the observer scale is only measuring the thickness and pliability of the scar. Pigmentation, vascularization, and relief are irrelevant and so are all the parameters of the patient scale. The results in this patient group using the POSAS scale question the use of the patient as an additional observer. Durani et al.[39] have presented the Patient Scar Assessment Questionnaire, which showed a better correlation when compared with the clinician assessment carried out with the VAS scale and the MSS.

The properties of a scar change over time, a process known as scar maturation. Scar redness, i.e., increased hemoglobin concentration, is present in the early phase and tends to decrease with time.[11] The maturation process

depends on various factors, such as scar location, etiology, individual response to scarring, wound tightness, etc. The treatment of problematic, HSs, such as burn scars, aims to produce mature scars. It is reasonable to believe that the ECC of hemoglobin value, produced by Spectrocutometry, is a relevant parameter when assessing an immature scar, whereas other measures, such as pliability or volumetric measurements, might be more relevant when rating a mature scar. We believe that Spectrocutometry can be used as a tool in clinical work to gain important information on active, HSs, and on the other hand, in scientific studies, where scar treatment or prevention methods are tested in a prospective, randomized setting.

Logically, it is not possible to gain a full picture of a scar by any single objective method. The VSS and POSAS scales are designed to combine multiple parameters for a thorough scar assessment. Unfortunately, this may result in seemingly different scars in gaining similar scores, as noted by Duncan et al.[11] It would be valuable to obtain an objective measure of such parameters as pliability and thickness, which, based on the finding in our study, seem significant. The Cutometer® (Courage-Khazaka Electronic) has been used by Nedelec et al.[40] to measure the pliability of scars, but the reliability of the method was not sufficient.

The ECC of hemoglobin correlates with the overall POSAS score, and also has a strong dependency on the scar pain, a fact worth noticing. Also, it is known that increased redness, reflecting a high hemoglobin concentration, is strongly associated with scar hypertrophy.[41] The ECC of melanin, on the other hand, as well as the subjective pigmentation ratings, seem to have no correlation with the overall scores, although they are correlated with each other and the patient rating of scar color. It appears that hypo- or hyperpigmentation are factors that may affect the cosmetic outcome of the scars, but do not reflect the scars' activity or degree of hypertrophy.

The proposed Spectrocutometry method showed high reliability in assessing linear scars in this study. A valuable aspect of this method is that it provides standardized image documentation of the scar. Conventional digital photography is dependent on the ambient lighting, and often, the distance and the angle to the target are changed, which makes it difficult to use the digital images for later judgment. As shown in the images in Figure 2, the scar and its surroundings in the images look quite identical even though the images were taken individually by different observers.

The mean age of the scars in this study was 17 months, which means that most of the scars were mature. It would be beneficial to study this method in a group of more immature scars. In the future, we aim to study the reliability and feasibility of Spectrocutometry on burn scars. We believe that this is an easy and reliable way to quantitatively measure and document changes in scar activity, and recommend it for both clinical and scientific work.

ACKNOWLEDGMENTS

Disclosure: None of the authors have a financial interest in any of the commercial products mentioned in this article.

REFERENCES

1. Junker JP, Kratz C, Tollback A, Kratz G. Mechanical tension stimulates the transdifferentiation of fibroblasts into myofibroblasts in human burn scars. *Burns* 2008; 34: 942–6.
2. Shin D, Minn KW. The effect of myofibroblast on contracture of hypertrophic scar. *Plast Reconstr Surg* 2004; 113: 633–40.
3. Sheridan RL, Tompkins RG. What's new in burns and metabolism. *J Am Coll Surg* 2004; 198: 243–63.
4. Li-Tsang CW, Lau JC, Chan CC. Prevalence of hypertrophic scar formation and its characteristics among the Chinese population. *Burns* 2005; 31: 610–6.
5. Bombaro KM, Engrav LH, Carrougher GJ, Wiechman SA, Faucher L, Costa BA, Heimbach DM, Rivara FP, Honari S. What is the prevalence of hypertrophic scarring following burns? *Burns* 2003; 29: 299–302.
6. Ogawa R. The most current algorithms for the treatment and prevention of hypertrophic scars and keloids. *Plast Reconstr Surg* 2010; 125: 557–68.
7. Mustoe TA, Cooter RD, Gold MH, Hobbs FD, Ramelet AA, Shakespeare PG, lla M, Téot L, Wood FM, Ziegler UE, International Advisory Panel on Scar Management. International clinical recommendations on scar management. *Plast Reconstr Surg* 2002; 110: 560–71.
8. Bloemen MC, van der Veer WM, Ulrich MM, van Zuijlen PP, Niessen FB, Middelkoop E. Prevention and curative management of hypertrophic scar formation. *Burns* 2009; 35: 463–75.
9. Durani P, McGrouther DA, Ferguson MW. Current scales for assessing human scarring: a review. *J Plast Reconstr Aesthet Surg* 2009; 62: 713–20.
10. Beausang E, Floyd H, Dunn KW, Orton CI, Ferguson MW. A new quantitative scale for clinical scar assessment. *Plast Reconstr Surg* 1998; 102: 1954–61.
11. Duncan JA, Bond JS, Mason T, Ludlow A, Cridland P, O'Kane S, Ferguson MW. Visual analogue scale scoring and ranking: a suitable and sensitive method for assessing scar quality? *Plast Reconstr Surg* 2006; 118: 909–18.
12. Chan KY, Lau CL, Adeeb SM, Somasundaram S, Nasir-Zahari M. A randomized, placebo-controlled, double-blind, prospective clinical trial of silicone gel in prevention of hypertrophic scar development in median sternotomy wound. *Plast Reconstr Surg* 2005; 116: 1013–20; discussion 21–2.
13. Nguyen DQ, Potokar T, Price P. A review of current objective and subjective scar assessment tools. *J Wound Care* 2008; 17: 101–2, 4–6.
14. Draaijers LJ, Tempelman FR, Botman YA, Kreis RW, Middelkoop E, van Zuijlen PP. Colour evaluation in scars: tristimulus colorimeter, narrow-band simple reflectance meter or subjective evaluation? *Burns* 2004; 30: 103–7.
15. Jung B, Choi B, Durkin AJ, Kelly KM, Nelson JS. Characterization of port wine stain skin erythema and melanin content using cross-polarized diffuse reflectance imaging. *Lasers Surg Med* 2004; 34: 174–81.
16. Latreille J, Gardinier S, Ambroisine L, Mauger E, Tenenhaus M, Guehenneux S, Morizot F, Tschachler E, Guinot C. Influence of skin colour on the detection of cutaneous erythema and tanning phenomena using reflectance spectrophotometry. *Skin Res Technol* 2007; 13: 236–41.
17. Takiwaki H, Miyaoka Y, Kohno H, Arase S. Graphic analysis of the relationship between skin colour change and

variations in the amounts of melanin and haemoglobin. *Skin Res Technol* 2002; 8: 78–83.
18. Zijlstra WG, Buursma A, Meeuwsen-van der Roest WP. Absorbtion spectra of human fetal and adult oxyhemoglobin, de-oxyhemoglobin, carboxyhemoglobin and methemoglobin. *Clin Chem* 1991; 37: 1633–8.
19. Välisuo P, Kaartinen I, Kuokkanen H, Alander J. The colour of blood in skin—a comparison of Allen's test and photonics simulations. *Skin Res Technol* 2010; 16: 390–6.
20. Kaartinen IVP, Kuokkanen H., Alander J. Objective scar assessment—a new method using standardized digital imaging and spectral modelling. *Burns* 2011; 37: 74–81.
21. Välisuo P, Harju T, Alander J. Reflectance measurement using digital camera and a protecting dome with built in light source. *J Biophotonics* 2010; DOI: 10.1002/jbio.201000113
22. Bochko VVP, Harju T., Alander J. Lower extremity ulcer image segmentation of visual and near-infrared imagery. *Skin Res Technol* 2010; 16: 190–7.
23. Shrout PE, Fleiss JL. Intraclass correlations: uses in assessing rater reliability. *Psychol Bull* 1979; 86: 420–8.
24. Nabney I. *Netlab: algorithms for pattern recognition*. Berlin: Springer Verlag, 2002.
25. Cooper GF. The computational complexity of probabilistic inference using Bayesian belief networks. *Artif Intell* 1990; 42: 393–405.
26. Pearl J. *Probabilistic reasoning in intelligent systems: Publisher: Networks of Plausible Inference*. Los Altos, CA: Morgan Kaufmann, 1988.
27. Myllymäki P, Silander T, Tirri H, Uronen P. B-course: a web-based tool for Bayesian and causal data analysis. *J Artificial Int Tools* 2002; 11: 369–88.
28. O'Brien L, Pandit A. Silicon gel sheeting for preventing and treating hypertrophic and keloid scars. *Cochrane Database Syst Rev* 2006: CD003826.
29. Harte D, Gordon J, Shaw M, Stinson M, Porter-Armstrong A. The use of pressure and silicone in hypertrophic scar management in burns patients: a pilot randomized controlled trial. *J Burn Care Res* 2009; 30: 632–42.
30. Karagoz H, Yuksel F, Ulkur E, Evinc R. Comparison of efficacy of silicone gel, silicone gel sheeting, and topical onion extract including heparin and allantoin for the treatment of postburn hypertrophic scars. *Burns* 2009; 35: 1097–103.
31. Forbes-Duchart L, Cooper J, Nedelec B, Ross L, Quanbury A. Burn therapists' opinion on the application and essential characteristics of a burn scar outcome measure. *J Burn Care Res* 2009; 30: 792–800.
32. Bloemen MC, van Leeuwen MC, van Vucht NE, van Zuijlen PP, Middelkoop E. Dermal substitution in acute burns and reconstructive surgery: a 12-year follow-up. *Plast Reconstr Surg* 2010; 125: 1450–9.
33. Draaijers LJ. Colour evaluation in scars: tristimulus colorimeter, narrow-band simple reflectance meter or subjective evaluation? *Burns* 2004; 30: 103–7.
34. Nedelec B, Correa JA, Rachelska G, Armour A, LaSalle L. Quantitative measurement of hypertrophic scar: interrater reliability and concurrent validity. *J Burn Care Res* 2008; 29: 501–11.
35. van Zuijlen PP, Angeles AP, Kreis RW, Bos KE, Middelkoop E. Scar assessment tools: implications for current research. *Plast Reconstr Surg* 2002; 109: 1108–22.
36. Truong PT, Lee JC, Soer B, Gaul CA, Olivotto IA. Reliability and validity testing of the Patient and Observer Scar Assessment Scale in evaluating linear scars after breast cancer surgery. *Plast Reconstr Surg* 2007; 119: 487–94.
37. Truong PT, Abnousi F, Yong CM, Hayashi A, Runkel JA, Phillips T, Olivotto IA. Standardized assessment of breast cancer surgical scars integrating the Vancouver Scar Scale, Short-Form McGill Pain Questionnaire, and patients' perspectives. *Plast Reconstr Surg* 2005; 116: 1291–9.
38. Draaijers LJ, Tempelman FR, Botman YA, Tuinebreijer WE, Middelkoop E, Kreis RW, van Zuijlen PP. The patient and observer scar assessment scale: a reliable and feasible tool for scar evaluation. *Plast Reconstr Surg* 2004; 113: 1960–5; discussion 6–7.
39. Durani P, McGrouther DA, Ferguson MW. The Patient Scar Assessment Questionnaire: a reliable and valid patient-reported outcomes measure for linear scars. *Plast Reconstr Surg* 2009; 123: 1481–9.
40. Nedelec B, Correa JA, Rachelska G, Armour A, LaSalle L. Quantitative measurement of hypertrophic scar: intrarater reliability, sensitivity, and specificity. *J Burn Care Res* 2008; 29: 489–500.
41. Li-Tsang CW, Lau JC, Liu SK. Validation of an objective scar pigmentation measurement by using a spectrocolorimeter. *Burns* 2003; 29: 779–84.

Publication V

This is the pre-peer reviewed version of the following article:

Välisuo, P., Harju, T. & Alander, J. (2011a). Reflectance measurement using digital camera and a protecting dome with built in light source. *Biophotonics* 4: 4.

The final version of the article is available on-line:
http://onlinelibrary.wiley.com/doi/10.1002/jbio.201000113/abstract

Reflectance measurement using digital camera and a protecting dome with built in light source

Petri Välisuo[1]*, Toni Harju*[1] *and Jarmo Alander*[1]

Abstract

The reflectance of the skin reveal the chemical and physical changes of the skin as well as many metabolic changes. The reflectance measurement is an important method for medical diagnosis, follow-up and screening. This article concentrates on designing and validating an imaging system, based on a digital camera. The proposed system can measure the reflectance of the skin with high spatial and currently four channel spectral resolution, in the range of 450 nm to 980 nm. The accuracy of the system was measured by imaging a colour checker board and comparing the obtained values with both given values and spectrometer measurements. The optical feedback of both, the integrating sphere and the lighting dome of the imaging system, was compensated with a correction factor. The accuracy of the proposed system is only slightly weaker than the spectrometer. The imaging system characteristics is independent of the camera characteristics.

1 Introduction

The skin is the largest organ of the human being. It is easily accessible and it's optical thickness is suitable for studying its structure and chemical contents with optical methods. The light, which wavelengths are between 600 and 1300 nm forms so called optical window, in which the light penetrates deeper into the skin than the other wavelengths (Tuchin 2007).

The skin diseases and injuries can usually be observed as skin colour changes. The colour of the skin is caused by the scattering of light from tissue structures and the absorbtion of light by the chromophores deposited in the skin, blood or intra cell fluids. The skin disorders often lead to visible change of skin colour, since they change either the physical structures or concentrations of the chromophores in the skin. Some metabolic disorders may also be observed as skin colour change, such as bilirubinemia,

[1]Department of Electrical Engineering and Automation, University of Vaasa, P.O. Box 700 FI-65101 Vaasa, Finland

which turns skin colour to yellowish. The colour of the skin may also change without any abnormal conditions, for example due to normal blood circulation regulation and increase melanin production due to sun bathing.

Accurate, *in vivo*, reflectance measurement can be used for quantifying the optical changes in skin. These measurements can be used for many purposes, including medical screening, diagnosis and follow-up or treatment. Localized skin disorders can be studied by examining how the concentration of skin chromophores are distributed around the skin disorder. This kind of chromophore mapping is a common topic in the literature (Konishi, Ito, Sakauchi, Kobayashi & Tsunazawa 2003; Jakovels & Spigulis 2010; Yamamoto, Takiwaki, Arase & Ohshima 2008; Kaartinen, Välisuo, Alander & Kuokkanen 2011; Kobayashi, Ito, Sakauchi, Oda, Konishi & Tsunazawa 2001; Clarys, Alewaeters, Lambrecht & Barel 2000). The chromophore maps of the different layers of the skin may provide useful information in medical diagnosis and follow-up. The chromophore concentrations of the melanocytic nevi may be used for diagnosing skin cancer (Claridge, Cotton, Hall & Moncrieff 2002; Claridge & Preece 2003; Preece & Claridge 2004), or evaluating wound healing (Kaartinen *et al.* 2011; Bon, Briand, Guichard, Couturaud, Revol, Servant & Dubertret 2000; Hansen, Sparrow, Kommamuri & Iaizzo PA 1996) or wound segmentation according to skin types (Bochko, Välisuo, Harju & Alander 2010).

The spectrophotometers and digital cameras are the most common equipments for recording and measuring the reflectance of the skin in the literature (Yamamoto *et al.* 2008; Bon *et al.* 2000; Hansen *et al.* 1996; Kaartinen *et al.* 2011; Kobayashi *et al.* 2001). Spectrophotometer provides high resolution in spectral domain, but the measurement is made from a single point only. The raw signal from the detector can be obtained and stored as such for further processing. Calibration and multivariate analysis methods for multispectral data are well established. A digital camera provides high spatial resolution, but measures only three spectral bands, which mimics the human colour vision, described in (CIE 1931), but the exact characteristic is usually unknown. The automatic colour balancing, exposure correction and other image processing made in the camera deteriorates the quality of the obtained reflectance estimate further. The dynamics of the detectors in high quality digital camera may be in par with a spectrophotometer but the image is usually compressed and converted to 8-bit dynamics before transferring it to the computer memory. The spectroscopic camera combines the benefits of the digital camera and the spectrophotometer. The disadvantages are much

higher price and more difficult operation. There are also medical equipments, which are specially made for measuring chromophore concentrations. They are based either on point spectra or tri-stimulus colour values of a small area (Clarys *et al.* 2000).

In this article we develop methods for overcoming the limitations of the usual digital camera and evaluate their suitability for chromophore mapping of human skin. Several techniques are designed to improve the reflectance estimate. Finally, the results are evaluated by measuring all 24 colours of the X-Rite ColorChecker Classic target (X-Rite, Grand Rapids, MI, USA).

2 Materials and methods

To disable all signal processing made by the camera, and to keep the full dynamics of the detector, the images are transferred from the camera to the computer memory in raw image form.

In our earlier work in (Välisuo, Mantere & Alander 2009), we concluded that the spectra of typical skin chromophores are so smooth that high spectral resolution is not needed to estimate chromophore concentrations. Four wavelengths are enough for estimating melanin and haemoglobin concentrations.

To make accurate RGB measurements with a digital camera, the sensitivities of the sensors of the camera should be measured first, since they are not often given in specifications. In this way Wu *et al.* prepared an accurate colorimeter from normal digital camera (Wu, Allebach & Analoui 2000). In our approach, instead of measuring RGB values, we expose the object with several narrow band LEDs, one at a time. The bandwidths of the narrow band LEDs are much narrower than the RGB filters in the sensor making the characteristics of the sensor irrelevant. In this way, the complicated calibration is avoided, and the imaging system can be extended from the tri-stimulus imaging to spectral imaging system, with more channels.

The center wavelengths of the LEDs in the light source are 468, 520, 639, and 939 nm and 3dB bandwidths are correspondingly 33, 39, 19, and 81 nm, see Figure (1). Normal CMOS and CCD image sensors are still sensitive as far as 1000 nm, but the cameras are often equipped with a filter, which attenuates the NIR wavelengths above

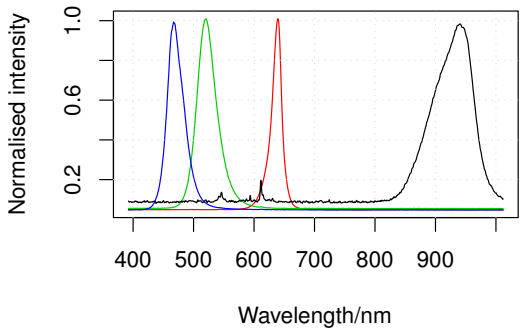

Figure 1. The four spectral bands of the LED light source

700 nm. Therefore we removed this filter from the camera to expand the usable range of the camera.

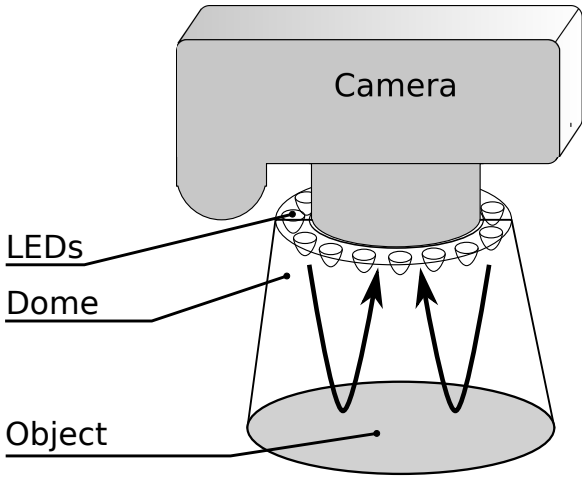

Figure 2. The schematic diagram of the imaging system.

The calibration procedures used with spectrophotometers were also taken into use in our imaging. The controlled light source is important in calibration. Our custom made light source consists of a dome, which protects the object from ambient light. The dome is connected to the camera (Canon Powershot G5, Canon Inc, Tokyo, Japan). The opening for lens of the camera is made in the middle of the roof of the dome. The light is produced by 72 moderate power surface mounted LEDs, placed around the lens hole, as shown in Figure (2). Surface mounted LEDs have usually wide radiation angle, producing smooth light field. The LEDs were placed as close to the optical axis as possible, to minimise shadows. The intensity of light in each band can now be measured by imaging a white reflectance standard. The image of the real object is then

compared with the image of the white standard, to obtain the plain reflectance of the object, R. The calibration of the imaging system in band i, is given by Equation (1).

$$R_i = \frac{\int E_i(\lambda)R(\lambda)C(\lambda)d\lambda}{\int E_i(\lambda)R_{w,i}C(\lambda)d\lambda}R_{w,i}, \tag{1}$$

where R_i is the reflectance of the object in band i, E_i is the spectra of light source in band i as the function of wavelength, λ, R is the true reflectance of the object, C is the sensitivity of the camera and $R_{w,i}$ is the reflectance of the white standard in band i.

The dome also introduces additional challenge in form of optical feedback. The illumination, reflected from the object will be reflected back from the dome, and increase the apparent illumination intensity. Let the light intensity from the light source be I_0, and the light reflected from the object RI_0. If the reflectance from the dome is r, then the light intensity reflecting back from the dome is rRI_0. This light increases the illumination, the reflected light intensity, and again the reflected intensity back from the dome. The total light intensity, I_{tot}, in the object surface is a geometric sum, given by Equation (2).

$$I_{tot} = I_0 + rRI_0 + \ldots = \sum_{i=0}^{\infty}(rR)^i I_0 = \frac{I_0}{1-rR} \tag{2}$$

The intensity I_{det}, which is detected by the sensor is the illumination, I_{tot}, multiplied by the reflectance, R, of the object:

$$I_{det} = I_{tot}R = \frac{I_0 R}{1-rR} \tag{3}$$

Calibration is obtained by first imaging a white reference, $R \approx 1$, and then the real object and normalising the reflectance of the object with a reflectance of the white reference. If the optical feedback of the dome is significant, then the result after calibration, R', is not only dependent on the reflectance of the object, R, but also of the reflectance of the dome, r. The equation for R' can be obtained by substituting Equation (3) to Equation (1) twice:

$$R' = \frac{I_{det}}{I_{det|R=1}} = \frac{I_0 R}{1-rR} \Big/ \frac{I_0}{1-r} = \frac{1-r}{1-rR}R \tag{4}$$

The reflectance of the object, R, can be easily solved from Equation (4), leading to Equation (5).

$$R = \frac{R'}{1 - r + rR'} \tag{5}$$

After this dome correction, measured R is an unbiased estimate of the reflectance.

Table 1. Given RGB values and the reflectances of the gray patches in the colour checker target, n is the index of the colour in the colour checker.

n	Colour name	Colour R, G, B	Reflectance R_r, R_g, R_b
19	White	243, 243, 242	0.896, 0.896, 0.888
20	Neutral 8	200, 200, 200	0.578, 0.578, 0.578
21	Neutral 6.5	160, 160, 160	0.352, 0.352, 0.352
22	Neutral 5	122, 122, 121	0.195, 0.195, 0.191
23	Neutral 3.5	85, 85, 85	0.091, 0.091, 0.091
24	Black	52, 52, 52	0.034, 0.034, 0.034

The imaging system was tested by measuring all 24 colours of the X-Rite ColorChecker Classic target (X-Rite, Grand Rapids, MI, USA). The reflectance values of the colours was obtained by applying a reverse gamma correction to the RGB values. The colour checker includes six shades of gray, from white to black, see Table (1). The white (R=0.90) was used as a white reference for calibration. The other gray shades were used for fitting the value of r for all four wavelength bands separately. Then, the accuracy of predicting the reflectances of the gray shades was calculated. The acquired reflectances for other colours cannot be compared with the RGB values provided with the colour checker, since the light source spectra differs from the D65 which is used for determining sRGB values (Stokes, Anderson, Chandrasekar & Motta 1996).

To verify the accuracy of the camera also for other colours and for the near infrared band, the same procedure was also repeated using a HR400 spectrophotometer (Ocean Optics, Dunedin, Florida, USA) and an ISP-REF integrating sphere (Ocean Optics) instead of the camera and the the light source and dome. The reflectance spectra was converted to the reflectance in the same spectral bands used in the imaging system, by multiplying the reflectance spectra with the spectra of the light source in each band, as shown in Equation (6). The dome correction shown in Equation (5) was applied to the

spectrophotometer results, too.

$$R_i = \int R(\lambda)\hat{E}_i(\lambda)d\lambda, \tag{6}$$

where $\hat{E}_i$ is a normalised spectra of the light source in band i.

Theoretical dome correction factor for the integrating sphere, can be derived from the sphere equations, which are listed for example in (SphereOptics LLC 2007). The reflectance, r_{is}, back from the integrating sphere is the ratio of out and in fluxes of the sphere

$$r_{is} = \Phi_{out}/\Phi_{in} \tag{7}$$

The flux out is the luminance of the sphere surface, L_{Sphere}, multiplied by the aperture area, $A_{Aperture} = \pi R^2_{Aperture}$. The luminance of the sphere surface is (SphereOptics LLC 2007):

$$L_{Sphere} = \frac{\Phi_{in}}{\pi A_{Sphere}} M, \tag{8}$$

where $M = \rho/(1-\rho(1-f))$ is the magnification factor of the sphere, ρ is the surface reflectance of the sphere and f is the ratio of reflective and non-reflective area of the sphere, which is in this case roughly the area of the aperture divided by the area of the surface

$$f = \frac{A_{Aperture}}{A_{Sphere}} = \frac{\pi R^2_{Aperture}}{4\pi R^2_{Sphere}} = \frac{1}{4}\left(\frac{R_{Aperture}}{R_{Sphere}}\right)^2 \tag{9}$$

The reflectance, r_{is}, from the integrating sphere is therefore:

$$r_{is} = \frac{\Phi_{out}}{\Phi_{in}} = \frac{L_{Sphere}A_{Aperture}}{\Phi_{in}} = \frac{A_{Aperture}}{\pi A_{Sphere}} M = \frac{R^2_{Aperture}}{4\pi R^2_{Sphere}} M \tag{10}$$

By substituting values $R_{Aperture} = 10.2$ mm, $R_{Sphere} = 38.1$ mm and $\rho = 0.98$ to Equations(9, 10) leads to following values: $f = 0.0178$, $M = 26.2$, $r_{is} = 0.148$.

3 Results

The compensation coefficients for the dome, r, and for the integrating sphere, r_{is}, are shown in Table (2).

Table 2. The experimental values of the optical feedback of the dome and the integrating sphere

Colour	Imaging dome	Integrating sphere
Blue, 468 nm	0.01	0.12
Green, 520 nm	0.00	0.13
Red, 639 nm	0.09	0.16
NIR, 939 nm	0.01	0.16

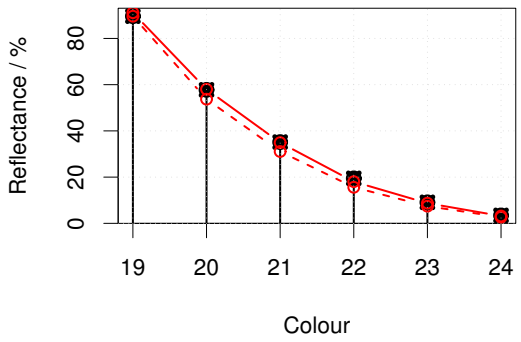

Figure 3. The reflectances of the grey patches. Vertical bars with black squares display the actual reflectances from Table (1), solid line shows the measured reflectance after compensation of the optical feedback and the dashed line shows the plain measurement result without compensation.

The accuracy of the reflectance measurements with camera and integrating sphere as RMSE values, are given in Table (3). The most important findings are related to compensation of the optical feedback and that the similarity of colour values obtained with an integrating sphere and with a camera over all colour patches.

The compensation of the optical feedback significantly improves the accuracy of the integrating sphere. It also improves the accuracy of the imaging dome in red, because the dome is not perfectly black. This kind of compensation is needed for all measuring setups, where any sort of dome if used, unless the dome is perfectly black.

The reflectance estimates were obtained from the measured reflectance spectra according to Equation (6). The equation only takes into account the spectra of the light source and assumes that the characteristics of the camera is irrelevant. The results show that the assumption holds, since the values obtained from the spectra correspond those measured with a camera over all 24 colour patches.

The results also show that the proposed imaging system can be used for measuring the reflectance values. It's RMSE is less than a percent of the full scale and is comparable to the accuracy obtained with an integrating sphere.

Table 3. The root mean square errors of the camera measurements (Cam) compared with the actual reflectances (Act) or spectrometer measurements (Spe), with or without optical feedback compensation (C). The RMSE over all colour patches (A24) or gray level patches only (Gray) is shown as percentages of the full scale.

			RMSE
Description	C	Col	Blue, Green, Red, NIR
Act vs Cam	N	Gray	0.820, 0.892, 1.795, -
Act vs Cam	Y	Gray	0.808, 0.892, 0.815, -
Act vs Spe	N	Gray	2.144, 2.223, 2.922, -
Act vs Spe	Y	Gray	0.626, 0.764, 0.880, -
Spe vs Cam	N	Gray	2.078, 2.676, 1.461, 3.183
Spe vs Cam	Y	Gray	0.850, 0.824, 0.891, 1.223
Act vs Cam	Y	A24	2.932, 3.024, 4.242, -
Act vs Spe	Y	A24	3.764, 3.473, 4.053, -
Spe vs Cam	Y	A24	1.011, 0.710, 0.884, 2.091

4 Discussion

The dome of the camera was almost black, and therefore the optical feedback values given in Table (2) are small for the camera. The calibration of the system couldn't be done properly for NIR channel, since the colour checker board does not cover NIR range. Gray reflectance standards for the NIR range needs to be acquired in the Future, to calibrate the lighting dome in the whole bandwidth. Still it is reasonable to believe, that the accuracy of the reflection measurement is also good in the NIR range, since it complies well with the spectrophotometer measurements. Somewhat higher error value

is probably due to the lower sensitivity of the camera in the NIR range.

The compensation required for the integrating sphere complies with the theoretical values calculated from Equation (10). According to the specifications, the reflectance of the surface of the IS-REF integrating spere should be approximately $\rho = 0.98$, which would lead to the correction factor $r = 0.148$. The observed correction factors for the integrating sphere were $r_{is} \in \{0.12, 0.13, 0.16, 0.16\}$. These values correspond to following surface reflectance values: $\rho \in \{0.972, 0.975, 0.983, 0.983\}$. These values are close to the nominal value.

The spectral resolution of the imaging system could be easily extended, by adding more LEDs of different wavelengths into the lighting system. For example, the wavelengths around 580 nm (yellow), 700 nm and 850 nm could be interesting, since they are easily available, and are not currently covered by the instrument.

5 Conclusion

In this article, several methods were used to overcome the limitations of the digital camera as a reflectance measurement device, for chromophore mapping and other medical imaging purposes. A computer controlled light source and a protecting dome was constructed to gain full control over the lighting conditions. Narrow-band led lights were used to reduce the influence of the camera characteristics. The images were transferred from the camera to the computer in raw data form, to disable the image processing algorithms of the camera in order to retain the full dynamics provided by the sensor. A white standard was used for calibration of the imaging system and the optical feedback from the dome was compensated. The dome compensation is necessary for all reflectance measurements, where optical feedback is involved, including measurements with an integrating sphere. The compensation was made by measuring a set of known grey levels and fitting the reflectance curve using a reflectance coefficient.

When all these means are utilised, the average root mean square error over all colour channels is 0.84% of the whole range. The corresponding error for the integrating sphere is 0.75%. The accuracy for digital imaging system is only slightly weaker than that achieved using an integrating sphere. The camera also complies well with the spectrophotometer in the near infrared range, showing that a digital camera can be also

used in measuring reflectance beyond its normal range.

The results show also, that the prediction of all 24 colour patches of the colour checker target, is not as accurate as the prediction of grey levels only. The error of the imaging system is 3.4% and 3.8% for the integrating sphere. But this was expected, since the illumination spectra of the light source is different from D65 which is required for measuring RGB values of the sRGB colour space. The obtained reflectance values for all colour channels over all 24 colour patches with camera are similar to those measured with spectrophotometer. The RMSE was 0.87% for the colour channels and 2.1% for the NIR channel. These results indicate that the camera characteristics is irrelevant in the proposed imaging system. Therefore the camera can be replaced with another with no effect to the measurement results.

References

Bochko, V., Välisuo, P., Harju, T. & Alander, J. (2010). Lower extremity ulcer image segmentation of visual and near-infrared imagery. *Skin Research and Technology* 16: 2, 190–197.

Bon, F.-X., Briand, E., Guichard, S., Couturaud, B., Revol, M., Servant, J.-M. & Dubertret, L. (2000). Quantitative and kinetic evolution of wound healing through image analysis. *IEEE Transactions on Medical Imaging* 19: 7, 767–772.

CIE (1931). *Commission internationale de l'Eclairage proceedings*. Cambridge, UK: Cambridge University Press.

Claridge, E., Cotton, S., Hall, P. & Moncrieff, M. (2002). From colour to tissue histology: Physics based interpretation of images of pigmented skin lesions. In T. Dohi & R. Kikinis (Eds.), *Medical Image Computing and Computer-Assisted Intervention — MICCAI 2002*, vol. 2488 of *Lecture Notes in Computer Science*. Berlin, Germany: Springer Berlin / Heidelberg, 730–738.

Claridge, E. & Preece, S. (2003). An inverse method for the recovery of tissue parameters from colour images. In *Information Processing in Medical Imaging*, vol. 2732. Ambleside, UK: Springer, 306–317.

Clarys, P., Alewaeters, K., Lambrecht, R. & Barel, A. (2000). Skin color measurements: comparison between three instruments: the Chromameter®, the DermaSpectrometer® and the Mexameter®. *Skin Research and Technology* 6: 4, 230–238.

Hansen, G., Sparrow, E., Kommamuri, N. & Iaizzo PA (1996). Assessing wound severity with color and infrared imaging of reactive hyperemia. *Wound Repair Regen* 4: 3,

386–392.

Jakovels, D. & Spigulis, J. (2010). 2-D mapping of skin chromophores in the spectral range 500-700 nm. *Journal of Biophotonics* 3: 3, 125–129.

Kaartinen, I. S., Välisuo, P. O., Alander, J. T. & Kuokkanen, H. O. (2011). Objective scar assessment–a new method using standardized digital imaging and spectral modelling. *Burns* 37: 1, 74–81.

Kobayashi, M., Ito, Y., Sakauchi, N., Oda, I., Konishi, I. & Tsunazawa, Y. (2001). Analysis of nonlinear relation for skin hemoglobin imaging. *Optics Express* 9: 13, 802–812.

Konishi, I., Ito, Y., Sakauchi, N., Kobayashi, M. & Tsunazawa, Y. (2003). A new optical imager for hemoglobin distribution in human skin. *Optical Review* 10: 6.

Preece, S. J. & Claridge, E. (2004). Spectral filter optimization for the recovery of parameters which describe human skin. *IEEE Transactions on Pattern Analysis and Machine Intelligence* 26: 7.

SphereOptics LLC (2007). Integrating sphere, design and applications. Tech. Rep..

Stokes, M., Anderson, M., Chandrasekar, S. & Motta, R. (1996). A standard default color space for the internet: sRGB. Tech. Rep..

Tuchin, V. (2007). *Tissue Optics: Light Scattering Methods and Instruments for Medical Diagnosis*. Bellingham, WA, USA: SPIE press.

Välisuo, P., Mantere, T. & Alander, J. (2009). Solving optical skin simulation model parameters using genetic algorithm. In *The 2nd International Conference on BioMedical Engineering and Informatics*. 376–380.

Wu, W., Allebach, J. P. & Analoui, M. (2000). Imaging colorimetry using a digital camera. *Journal of Imaging Science and Technology* 44: 4, 267–279.

Yamamoto, T., Takiwaki, H., Arase, S. & Ohshima, H. (2008). Derivation and clinical application of special imaging by means of digital cameras and Image J freeware for quantification of erythema and pigmentation. *Skin Research and Technology* 14: 1, 26–34.

Publication VI

Välisuo, P., Kaartinen, I., Tuchin, V. & Alander, J. (2011). New closed–form approximation for skin chromophore mapping. *Journal of Biomedical Optics*, 16: 4, 046012.

Journal of Biomedical Optics 16(4), 046012 (April 2011)

New closed-form approximation for skin chromophore mapping

Petri Välisuo,[a] Ilkka Kaartinen,[b] Valery Tuchin,[c] and Jarmo Alander[a]
[a]University of Vaasa, Department of Electrical and Energy Engineering, Automation Technology, Wolffintie 34, Vaasa, 65101 Finland
[b]Tampere University Hospital, Department of Plastic Surgery, Tampere, Finland
[c]Saratov State University, Institute of Precise Mechanics and Control of RAS, Saratov, Russia

Abstract. The concentrations of blood and melanin in skin can be estimated based on the reflectance of light. Many models for this estimation have been built, such as Monte Carlo simulation, diffusion models, and the differential modified Beer–Lambert law. The optimization-based methods are too slow for chromophore mapping of high-resolution spectral images, and the differential modified Beer–Lambert is not often accurate enough. Optimal coefficients for the differential Beer–Lambert model are calculated by differentiating the diffusion model, optimized to the normal skin spectrum. The derivatives are then used in predicting the difference in chromophore concentrations from the difference in absorption spectra. The accuracy of the method is tested both computationally and experimentally using a Monte Carlo multilayer simulation model, and the data are measured from the palm of a hand during an Allen's test, which modulates the blood content of skin. The correlations of the given and predicted blood, melanin, and oxygen saturation levels are correspondingly $r = 0.94$, $r = 0.99$, and $r = 0.73$. The prediction of the concentrations for all pixels in a 1-megapixel image would take ~20 min, which is orders of magnitude faster than the methods based on optimization during the prediction. [DOI: 10.1117/1.3562976]

Keywords: diffusion theory; Monte Carlo methods; Beer–Lambert law; integrating sphere biomedical engineering; optics; photonics; biological tissues; multispectral imaging; medical imaging; dermal imaging.

Paper 10651R received Dec. 10, 2010; revised manuscript received Feb. 16, 2011; accepted for publication Feb. 17, 2011; published online Apr. 7, 2011.

1 Introduction

The reflectance spectra of human skin can be used to study its physical structure and chemical contents. The reflectance spectra measurement is a fast and convenient method for obtaining dermal information. The spectra can be measured using a spectrophotometer or with a multiband digital imaging device. In reflectance spectroscopy, the skin is illuminated with a light source and the spectra of the reflected light is measured. Often visible and near-infrared (NIR) light are used for measurements because they penetrate deeper into the skin than the longer or shorter wavelengths. The measured reflectance spectra can be used in estimation of the distributions of the skin chromophores, such as melanin and hemoglobin. These chromophore maps may help in diagnosing and following up on skin disorders. Therefore, chromophore mapping is a common topic in the skin-imaging literature.[1–7] Several commercial technologies have been developed especially for measuring the skin chromophore concentrations, such as DermaSpectrometer®, Mexameter®, Chromameter®,[6] EMM-01,[7] SIAScopy®,[8] and TIVI® imaging.[9] Comparative measurements of erythema and melanin indexes using the EMM-01 and Mexameter MX-16 (Courage + Khazaka electronic GmbH, Cologne, Germany) devices as well as color measurements with the Minolta Chromameter CR-200b (Higashi-Ku, Japan) were performed in Ref. 7.

Because the light interaction in skin is complicated, there is no single method for chromophore concentration estimation that is the best for all purposes. Therefore, many different methods are frequently used in skin analysis. These methods are listed in recently published reviews.[10,11] One of the most versatile methods for this purpose is Monte Carlo simulation, for example, the Monte Carlo multilayer (MCML) software.[12–14] It is relatively easy to include the absorption of all important skin chromophores and scattering factors into the model. Notwithstanding the long simulation times, the model has been used for many purposes, such as in the development of the pulse oximeter,[15] melanoma diagnostics,[16–18] melanin- and blood-concentration measurements,[19,20] skin-treatment planning,[21] and determination of the information depth of the skin reflectance.[22]

Another often-used method for modeling light transport in skin is the diffusion approximation of the light transport equation.[23,24] Diffusion approximation is expressed as a mathematical formula that can be calculated much faster than the MCML model but it is less versatile. However, solving of inverse problems is required by means of an optimization algorithm, such as that of Levenberg–Marquardt (LMA).

Most solutions, aiming at even faster processing, are based on the Beer–Lambert law (BLL), which is the profound theory behind chemometry. The BLL states that the absorption A, of light transmitted through a substance, whose thickness is d is

Address all correspondence to: Petri Välisuo, University of Vaasa, Department of Electrical and Energy Engineering, Automation Technology, Wolffintie 34, Vaasa, L nsi-Suomi 65101 Finland. Tel: 358445804320; Fax: 358-6-324 8677; E-mail: petri.valisuo@uwasa.fi.

1083-3668/2011/16(4)/046012/10/$25.00 © 2011 SPIE

directly proportional to the absorption coefficient, μ_a of the substance.

$$A = \mu_a d. \tag{1}$$

The absorption coefficient is the product of the molar extinction coefficient ε and the concentration c of the chromophore

$$\mu_a = c\,\varepsilon. \tag{2}$$

This law strictly holds only for light transmission when scattering is negligible. However, the scattering in skin is strong; thus, Beer–Lambert as such does not hold. On the other hand, the backscattering makes it possible to use the reflection-measurement setup instead of transmission, which is much more convenient for *in vivo* measurements. The goal for many researchers has been to modify either the BLL or the reflectance-measurement setup so that the BLL could be applied.

In scattering media, the photons do not follow direct path. Therefore, the thickness, *d,* must be replaced with a mean pathlength, *p*, of the photon, which is usually unknown, and depends on the absorption and scattering. Furthermore, photons are scattered in all directions, and only a small amount of them are captured by the detector, resulting in a scattering loss, which is often modeled as an additive term *G*. The modified Beer–Lambert law (MBLL), takes also into account these additional parameters,[25,26]

$$A = \mu_a p + G. \tag{3}$$

Because of the constant, unknown term, *G*, the absolute absorption coefficient values cannot be solved from known absorptions. If it is assumed that the scattering loss is constant, then the term *G* disappears when examining the differences of absorptions. Therefore, the MBLL is often used in a differential form, known as differential modified Beer–Lambert law (dMBLL),

$$\frac{\partial}{\partial \mu_a} A = \frac{\partial}{\partial \mu_a} \mu_a p. \tag{4}$$

The dMBLL, shown in Eq. (4), is described in Ref. 27, as well as the error caused by assuming *G* as constant when it is not. If the pathlength, *p*, is not dependent on μ_a, then the derivative of absorption is just the pathlength and the dMBLL is linear. If either *p* or *G* is dependent on μ_a, both *A* and $\partial A/\partial \mu_a$ are nonlinear. In many papers, $\partial A/\partial \mu_a$ is assumed to be linear.[3,27–29]

Mourant et al. found that in a special measurement setup, where light is illuminated from one optical fiber and collected from another so that the distance between the fibers is between 1.5 and 2.2 mm, the mean pathlength of the photons is only slightly dependent on the changes on the scattering coefficient.[30] In this case, the dMBLL holds well, provided that the $p(\mu_a)$ can be modeled. Mourant et al. used a model $p(\mu_a) = x_0 + x_1^{-x_2\mu_a}$, where x_i are experimental coefficients.

Amelink and Sterenberg[31] made a special measurement device where light is fed using one emitter fiber and detected by two fibers, simultaneously. The first detector fiber (d_e) is the emitter fiber itself, and the second (d) is a separate fiber located close to the emitter. The difference of the two detected signals is said to mostly contain the effect of the single scattered photons. In this case, the average pathlength *p* is constant, the dMBLL is linear, and actually, the Beer–Lambert could be applied as such.[31]

Unfortunately, these special measurement setups cannot be used for chromophore mapping because they lack the spatial dimensions. A method that is fast and accurate enough for chromophore mapping of images with high spatial and modest spectral resolution is needed in a skin-imaging system, such as the Spectrocutometer.[4,32] The new approach taken in this paper is to apply dMBLL to solve chromophore maps from digital images, linearizing the dMBLL model around an operating point deduced from the normal skin spectra of the individual. For the linearized model the partial derivatives of the absorption by the absorption coefficients of each chromophore are needed. These derivatives are obtained by constructing a two-layer skin model using the Beer–Lambert law and diffusion model and by differentiating the model analytically. The constructed model is first fitted to one selected absorption spectrum, using LMA optimization, to find the chromophore concentrations. The derivatives are then used to find the differences of the chromophore concentrations for the other spectra using dMBLL in closed form. The method is tested by comparing it to the MCML simulation model.

2 Materials and Methods

Melanin, oxyhemoglobin, and deoxyhemoglobin are the most important chromophores in skin. In healthy skin, melanin is deposited in epidermis, whereas hemoglobin is dissolved in blood, which is located deeper in the skin, in the dermis. The absorption of the epidermis is $\mu_{a,e}p_e$, where $\mu_{a,e} = c_m\varepsilon_m$ is the absorption coefficient of epidermis, which equals to the concentration of melanin, $c_{m,}$ times the extinction coefficient of melanin, ε_m. The absorption coefficient of blood, μ_b, depends on the absorption coefficients of the chromophores in blood, oxygenated hemoglobin, $\mu_{a,HBo}$, and deoxygenated hemoglobin, $\mu_{a,HBd}$. The absorption of blood is therefore $\mu_{a,b}p_d = (\mu_{a,HBo} + \mu_{a,HBd})p_d$ where p_d is the average pathlength of photons in dermis. Usually, the absorption coefficient of dermis itself, is modeled as skin baseline, $\mu_{a,d}p_d$. Therefore, the equation describing the attenuation of skin, can be written as follows:

$$A = \mu_{a,e}p_e + \mu_{a,b}p_d + \mu_{a,d}p_d + G. \tag{5}$$

The epidermis is weakly absorbing by itself, but the melanin deposited primarily in the bottom of the epidermis, in *stratum basale,* absorb light strongly. Because the epidermis is thin, $d_e \approx 100\ \mu$m, and it is the topmost layer, the mean pathlength of a remitted photon in the epidermis is not affected much by the absorption of dermis or epidermis. Therefore, the derivative of Eq. (5) by the absorption in the epidermis, is approximately

$$\frac{\partial A}{\partial \mu_{a,e}} \approx p_e. \tag{6}$$

On the other hand, the mean pathlength in dermis, p_d, is dependent on the absorption coefficient in blood and in dermis. If $\mu_{a,b}$, is high, then only the photons remitted from the superficial layers in the dermis will survive back and the average pathlength in the dermis will be short. Therefore, the derivative of Eq. (5)

by the absorption in blood, $\mu_{a,b}$, is more complicated,

$$\frac{\partial A}{\partial \mu_{a,b}} = p_d + \mu_{a,b} p'_d + \mu_{a,d} p'_d, \tag{7}$$

where $p'_d = \partial p_d / \partial \mu_{a,b}$. The first term corresponds to the basic Beer–Lambert law. The second term adds a nonlinear component due to the nonconstant pathlength. The third term is cross-talk from absorption of dermis to absorption of blood.

2.1 *Diffusion Model*

Equation (7) cannot be used for calculating concentration changes because p_d is not known. The model based on diffusion theory, introduced by Farrell et al.[24] and Patterson et al.,[23] can be used for obtaining the partial derivatives needed. The diffusion model assumes a pencil-beam-shaped light source. It is further assumed that the light beam can be replaced with a point source located at the depth of the mean free path, $z_0 = 1/(\mu'_s + \mu_a)$, under the skin surface and the corresponding image source at the height of 2 $z_b + z_0$ from the skin surface, where $z_b = (2\ K)D$ is the height of the virtual boundary, where K is the internal reflection, which is assumed to be $K = (1 + r_d)/(1 - r_d)$, where r_d is the reflectance coefficient mismatch in the air-tissue boundary and $D = z_0/3$ is the diffusivity coefficient. The diffusion reflectance can be modeled by means of transport albedo $\mu'_a = \mu'_s/(\mu'_s + \mu_a)$, and internal reflection K. A more accurate model is obtained by assuming that there is a point source in every point along the pencil beam in the tissue, in which intensity along the depth, z, is $I(z) = \mu'_a \mu'_t e^{-\mu'_t z}$, where $\mu'_t = \mu_a + \mu'_s$ is the total interaction coefficient. Therefore, the total reflectance, R_d, of infinite narrow beam is[24]

$$R_d = \frac{\mu'_a}{2} \frac{1 + e^{-4/(3K)T}}{1 + T}, \tag{8}$$

where

$$T = \sqrt{3(1 - \mu'_a)}. \tag{9}$$

The absorption, $A_{d,}$ of radiation in tissue is

$$A_d = \log(1/R_d). \tag{10}$$

The derivative of Eq. (10) by absorption coefficient, μ_a, is

$$\frac{\partial A_d}{\partial \mu_a} = \frac{z_0}{2(T+1)} \left[2(T+1) + \frac{3 z_0 \mu'_s}{T} + \frac{4K z_0 \mu'_s (T+1) e^{-4/(3KT)}}{T(e^{-4/(3KT)} + 1)} \right]. \tag{11}$$

The epidermis and dermis are the two most important layers for optical skin models. The dermis can be further subdivided, but it may not be always necessary. Here, the skin model assumes a thin epidermis layer situated on top of the dermis layer. The absorption in epidermis, A_e, is modeled simply using BLL, so that $A_e = \mu_{a,e} p_e$, where the average pathlength in epidermis, p_e, is slightly longer than the thickness of the epidermis, d_e. The absorption of dermis is modeled using the diffusion model, described in Eq. (10). The specular reflectance is assumed to be wavelength-independent constant.

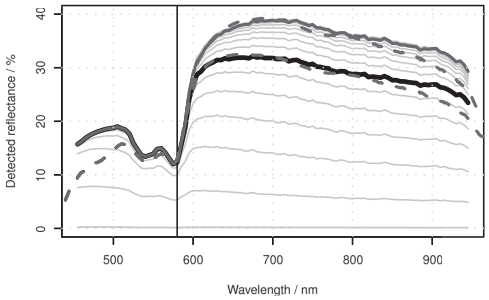

Fig. 1 Edge losses and edge-loss compensation. The gray lines show the detected reflectance as a function of wavelength, from bottom to top, r_a is 0, 0.1, 0.2, 0.3, . . . , 1.5 cm. The lower solid thick line shows the simulated detected reflectance, whereas the lower thick dashed line shows measured spectra. The upper thick and dashed lines show the simulated and measured spectra after edge loss compensation.

2.2 *Edge Losses*

One of the data sets used in this paper is measured using an integrating sphere, which is often used as an optical probe for reflection measurements. However, it introduces some nonideal characteristics that must be taken into account. The integrating sphere illuminates the target at the area of its aperture, which is the radius r_a. It collects the specular and diffuse reflectance only from the area covered by the aperture. However, part of the diffuse reflectance is remitted from the area behind the edge of the aperture and part of the reflectance is therefore lost. To reduce edge losses, some integrating spheres contain a lens system that can be used either in focusing the illumination into a narrow collimated beam or limiting the detection area. To estimate the edge losses of an integrating sphere with a lens system used for illumination, an MCML simulation was performed with a collimated circular light beam of radius $r_b = 0.15$ cm and aperture of radius $r_a = 0.5$ cm, which are the properties of the integrating sphere used in the Allen's test measurements. The result of the MCML simulation is a radial cross section of the reflectance intensity. The intensity of the total collected reflectance can be obtained by integrating the reflectance intensity curve over a circle of radius $r_{a.}$ The detected reflectance and the edge losses should be the same in a symmetrical case, where the integrating sphere is used for providing diffuse light in the circular area, of radius, $r_{a,}$ and the lens system is used for limiting the detection in the circular area of radius, r_b The results of the simulation are shown in Fig. 1.

The detection efficacy of the integrating sphere was calculated by dividing the reflectance obtained using the real aperture radius with the reflectance using very large aperture radius, capturing virtually all reflected signal,

$$\eta(\lambda) = \frac{R(\lambda)_{|r_a = 0.6\ \mathrm{cm}}}{R(\lambda)_{|r_a = 1.5\ \mathrm{cm}}}. \tag{12}$$

According to MCML simulation, the losses are negligible when wavelength, λ, is smaller than $\lambda_t = 580$ nm. When $\lambda > \lambda_t$, $\eta(\lambda)$ can be modeled as an exponent function. Therefore,

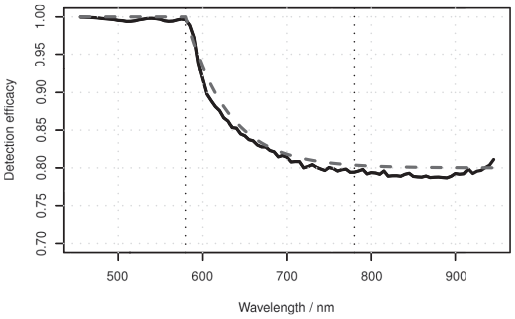

Fig. 2 Detection efficacy due to edge losses. The solid line shows the simulated detection efficacy and dashed line shows the detection efficacy model.

the detection efficacy is

$$\eta(\lambda) = \begin{cases} 1 & \text{if} \quad \lambda \leq \lambda_t \\ E_L + (1 - E_L)e^{k(\lambda_t - \lambda)} & \text{if} \quad \lambda \leq \lambda_t, \end{cases} \tag{13}$$

where E_L is the edge loss coefficient, describing the maximum detection efficacy in the NIR range, and k is an experimental constant. For simulated skin parameters and given integrating sphere geometry, $E_L = 0.8$ and $k = 0.02$. The simulated and modeled $\eta(\lambda)$ are shown in Fig. 2.

The detection efficacy model was further tested by plotting one spectra from the Allen's test data, before and after the edge loss compensation. These measured spectra are also shown in Fig. 1.

2.3 *Total Skin Reflectance Model*

The total absorption of the skin, when the diffusion model of the dermis, the Beer–Lambert model of the epidermis, the edge losses, and the specular reflections are taken into account, is shown in Fig. 3. The reflectance from epidermis to the air is assumed to be independent on the wavelength and is accounted for by increasing the specular reflection coefficient R_s. The scattering from epidermis to dermis is neglected in the model.

The parameters of the model are the specular reflection R_s, the absorption of the epidermis A_e, the absorption of the dermis A_d, and the edge loss coefficient E. From Eqs. (8) and (9), it is apparent that the absorption in Eq. (10) is directly determined by the internal reflectance of because K, and the transport albedo μ_a'. The transport albedo, in turn, is a sum of all absorption and scattering properties of skin because $\mu_a = \mu_s'/(\mu_s' + \mu_a)$. The absorption coefficient is a function of absolute chromophore concentrations, because $\mu_a' = \sum_i \varepsilon_i(\lambda)c_i$, where ε_i is the *a priori* known molar extinction coefficient of chromophore i. Therefore, the transport albedo can be calculated as follows:

$$\mu_a'(\lambda, \mathbf{c}) = \frac{\mu_s'(\lambda)}{\mu_s'(\lambda) + \sum_i \varepsilon_i(\lambda)\mathbf{c}_i}, \tag{14}$$

where $\mathbf{c} = [c_1, c_2, \ldots]^T$ is a vector containing the concentrations of all chromophores included in the model.

Because μ_a' is a function of λ and $\mathbf{c}$, so are $T(\lambda, \mathbf{c})$, $R_d(\lambda, \mathbf{c})$ and $A_d(\lambda, \mathbf{c})$ as well. The BLL model of epidermis is $A_e(\lambda, c_m) = \varepsilon_{m(\lambda)}c_m$. The parameters for the edge-loss model, $E(\lambda)$ are E_L and k. The total skin reflectance model can used in solving the concentrations, by adapting it to the measured reflectance spectrum, by minimizing the following square error over all spectral channels, i:

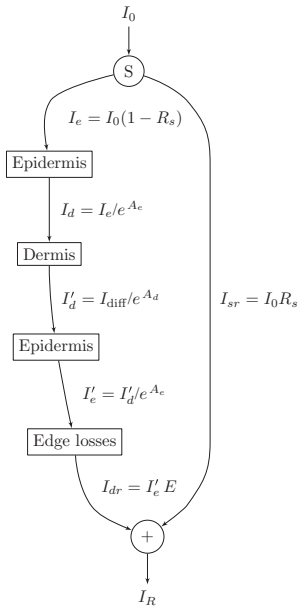

Fig. 3 Photon path model. The incident light beam, I_0, is first divided in two parts, the diffuse reflected part, I_e, and the specularly reflected part, I_{sr}. The diffuse reflected beam, I_e, travels through epidermis and is partly absorbed. The transmitted part, I_d, enters into the dermis and is partly reflected back. The reflected intensity, I'_d, goes through epidermis the second time. The diffuse and specular reflections are collected by a detector, which potentially causes edge losses to the diffuse reflected part of light, I'_e. The absorption of epidermis, A_e, is calculated by the Beer–Lambert law and the absorption of dermis, A_d, is obtained from the diffusion theory.

$$E_{SS}(\mathbf{c}, R_s, E_L, k) = \sum_i \left[R_{\text{measured}}(\lambda_i) - R_{\text{predicted}}(\lambda_i, \mathbf{c}, R_s, E_L, k)\right]^2. \tag{15}$$

The E_{SS} can be minimized by finding optimal values for the parameters with LMA algorithm, for example. When the skin model is optimized, the derivative shown in Eq. (10) can be obtained.

The absorption difference between two locations of skin can now be written using Eqs. (6) and (11) as a Taylor series,

$$\Delta A = \frac{\partial}{\partial \mu_a} A\left(\Delta\mu_{a,b} + \Delta\mu_{a,d}\right) + 2p_e\Delta\mu_{a,e}. \tag{16}$$

The specular reflection is canceled when measuring the difference of two absorption spectra; therefore, it may be ignored. The possible edge loss needs to be compensated before applying Eq. (16). To keep the system linear, the higher order terms of the Taylor series cannot be used. The chromophore concentrations

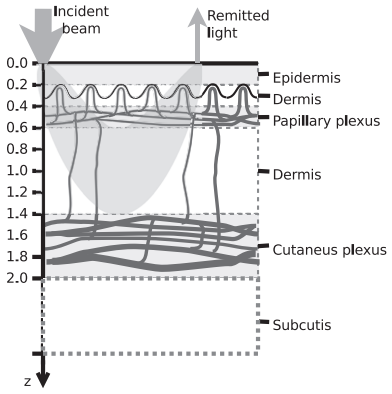

Fig. 4 MCML skin-simulation model structure. The depths of the layers in millimeters are given along *z*-axis, in the left hand side. The layers of the skin model are shown in the right hand side. The incident and remitted light beams are shown in the top. The banana-shaped area is a schematic of the typical path for the photons contributing to the remittance shown by the arrow.

can be solved when the absorption coefficients, μ_a', are replaced by concentrations and extinction coefficients,

$$\Delta A = \frac{\partial}{\partial \mu_a} A\,(\Delta c_{\mathrm{HBo}} \varepsilon_{\mathrm{HBo}} + \Delta c_{\mathrm{HBd}} \varepsilon_{\mathrm{HBd}} + \Delta c_{\mathrm{base}} \varepsilon_{\mathrm{base}}) + 2 p_e \Delta c_m \varepsilon_m. \tag{17}$$

Equation (17) contains four unknown concentrations. They can be solved by measuring the absorption change, ΔA, in at least at four different wavelengths, and finding an least-mean-squares (LMS) solution for each absorption. The wavelengths should be selected so that the equations are linearly independent. This can be arranged by selecting the wavelength sufficiently far away from each other. The absorption coefficients have unique spectra because they depend on the spectra of the extinction coefficients, ε.

2.4 *Reference Data Using Monte Carlo Simulation*

To validate the proposed chromophore mapping technique, it was compared to the MCML simulation model. The MCML model consists of the model structure and the parameters. The structure is assumed to consists of homogeneous layers (shown in Fig. 4). The model was originally developed by Tuchin et al.,[33] adopted by Reuss,[15] and used, among others, by us.[20,22,34]

The parameters of each layer are the thickness, *d,* the absorption coefficient, μ_a, the scattering coefficient, $\mu_{s,}$ and the anisotropy, g. To be able to estimate the absorption coefficients, the skin chromophores and their concentrations are needed. In addition to hemoglobin and melanin, bilirubin and β-carotene may also affect to the concentration prediction. Water is only significant above 800 nm; it does not influence the skin color. The skin model was tuned to match palm skin over a range of different blood concentrations using the Allen's test, as described in Ref. 34. The nominal blood concentration is 150 g/l. The hemoglobin molar concentration in blood can therefore be calculated by dividing the concentration in grams/liter with the molar mass of hemoglobin; therefore,

$$c_{\mathrm{Hb,blood}} = \frac{150\ \mathrm{g/l}}{64500\ \mathrm{g/mol}} = 2.326\ \mathrm{mol/l}. \tag{18}$$

The concentration of hemoglobin in skin is obtained by multiplying the hemoglobin concentration with the amount of blood in skin, the blood fraction, f_b. Therefore,

$$C_{\mathrm{Hb,skin}} = f_b\ C_{\mathrm{Hb,blood}}. \tag{19}$$

The typical value for f_b was 0.05 according to Reuss in Ref. 15. We have observed lower f_b values in our earlier studies, including, Ref. 34 where $f_b \in [0.0016, 0.0045]$.

Often the absorption coefficient of melanin is modeled as follows:

$$\mu_{a,m} = f_m (1.70 \times 10^{12}) \lambda^{-3.48} \quad (1/\mathrm{cm}), \tag{20}$$

where λ is the wavelength in nanometers. The melanin fraction, f_m, is estimated instead of estimating the concentration of melanin molecules.[35] This is because the size, structure, and the absorption efficiency of the melanin molecules may vary. Therefore, the absorption coefficient for given melanin concentration is not well defined.

The scattering of the tissue was modeled as a combination of Mie and Rayleigh scattering, as follows:[36]

$$\mu_s(\lambda) = \mu_{s,\mathrm{Mie}}(\lambda) + \mu_{s,\mathrm{Rayleigh}}(\lambda) = 2 \times 10^5 \times \lambda^{-15} + 2 \times 10^{12} \times \lambda^{-4.0}. \tag{21}$$

The skin without blood, the skin baseline, was simulated using following formula:[37]

$$\mu_{a,d}(\lambda) = 7.84 \times 10^8 \times \lambda^{-3.255} \tag{22}$$

The variations in bilirubin concentration can potentially disturb the prediction of hemoglobin concentration or oxygen saturation. Therefore, the bilirubin concentration was varied in MCML simulation even though the prediction of the bilirubin content was not tried. The nominal bilirubin concentration in blood is $C_{\mathrm{Br}} = 10\ \mu$M/1. The bilirubin concentration was kept constant during "Blood" and "Melanin" data set simulation, and random values between the range, shown in Table 1 were selected in the simulation of the "Random" data set.

The above skin model is used to generate four data sets, described in Table 1. The first two data sets are used for obtaining the numerical derivative of absorption by the melanin or blood concentrations for reference. The melanin set, contains 32 simulated skin spectra where all variables, except melanin concentration were kept constant. The melanin concentration was linearly distributed within a given range. In the blood data set, which also contains 32 simulated spectra, all variables except blood volume fraction, f_b, were kept constant. The blood fraction, f_b, was a linearly distributed within a given range. The random data set contains 104 simulated spectra, where independent random values were selected for melanin and blood concentrations from the given ranges.

Table 1 Simulated data sets and the range of the parameters during the simulation.

Data-set name	Number of samples	Range
Melanin	32	$f_m \in [0.01, 0.04]$
		$f_b = 0.005$
		Os = 0.8
		$C_{Br} = 10\ \mu M/l$
Blood	32	$f_m = 0.02$
		$f_b \in [0.0, 0.010]$
		Os = 0.8
		$C_{Br} = 10\ \mu M/l$
Random	104	$f_m \in [0.0, 0.05]$
		$f_b \in [0.0, 0.025]$
		Os ∈ [0.6, 1]
		$C_{Br} \in [2.5, 25]\ \mu M/l$

Each simulated spectra, in each data set, contains 78 wavelengths in the range $\lambda \in [380, 1050]$ nm. The simulations were made by tracking 10^6 photons for each simulated wavelength. The plain MCML simulation estimates the reflectance of an infinite thin pencil beam.

2.5 *Allen's Test Data*

In addition to the simulated data, the proposed algorithm was also validated using a measured data set. The measured data set consists of the reflectance spectra of the human skin from the palm of the hand from 20 persons, 5 locations each. From each location, a series of 10 consequent samples were measured at the rate of ∼1.8 samples per second. The measurements were carried out using an HR4000 spectrometer (Ocean Optics, Dunedin, Florida) and an ISP-REF integrating sphere (Ocean Optics). The measurement of the reflectance of the palm was acquired so that the test person placed his or her hand very lightly on the integrating sphere. The skin was illuminated with a diffuse light field over the whole aperture of the sphere, in which radius $r_a = 0.5$ cm, using a light source, built in the sphere. The reflectance was collected in the middle of the aperture, from the circular area, in which the radius is $r_b = 0.15$ cm. The experiment is further described in Ref. 34.

3 Results

3.1 *Numerical Versus Analytical Derivatives*

To validate the analytical derivatives shown in Eqs. (6) and (11), they were compared to corresponding numerical derivatives obtained from the MCML data sets, melanin and blood, shown in Table 1. These data sets contain the absorption spectra when a single-chromophore concentration, either melanin or blood, is perturbed within a range, and all other parameters are kept unchanged. A third-order polynomial was fitted to the simulated $A(c)$ curves, using statistical software package, R, and functional data analysis toolbox.[38] The derivatives of $A(c)$ were now easily obtained by differentiating the corresponding polynomials. To study these polynomials and the first-order derivative over full reflectance spectra, the absorptions were differentiated by the concentrations instead of the absorption coefficients, and the procedure was repeated over the spectral range of $\lambda \in [380, 1050]$ nm. The derivative of the absorption, A, by the absorption coefficient μ, and the derivative by the concentration are directly related because

$$\frac{\partial}{\partial \mu} A(\lambda, \mu) = \frac{1}{\varepsilon(\lambda)} \frac{\partial}{\partial c} A(\lambda, c). \tag{23}$$

The simulation results for Eq. (5) as a function of varying melanin concentrations are shown in Fig. 5(a). The polynomial was fitted to the measured values of absorption as a function of melanin concentration, $A(c_m)$, at each wavelength. Figure 5(b) displays the coefficients of the $A(c_m)$ polynomial over all wavelengths.

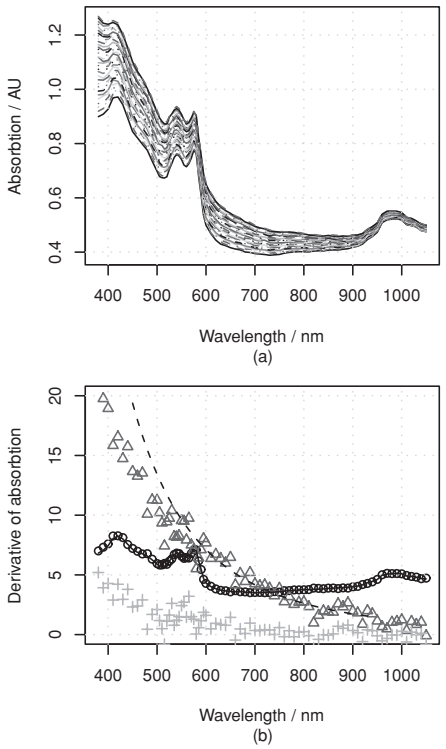

Fig. 5 Absorption of skin by varying melanin fraction, f_m. (a) Absorption when the melanin fraction is increased from 1 to 4% in even steps of 0.095%. (b) Zeroth- (O), first- (Δ), and second- (+) order coefficients (not in scale) of the fitted polynomial $A(c_m)$. The solid line shows the absorption when $c_m = 0$, and the dashed line shows the analytical derivative $\partial A/\partial \mu_{a,m}$.

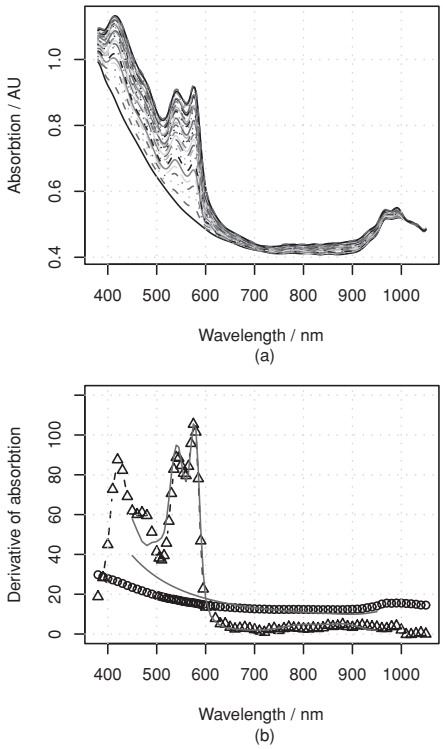

Fig. 6 Absorption of skin with varying blood concentration. (a) Absorption when the skin blood fraction is increased from 0 to 1% in even steps of 0.031%. (b) Zeroth- (O) and first-(Δ) order coefficients of the fitted polynomial $A(c_m)$ (zeroth-order polyno mials is multiplied by 30), the coefficients of the absorption polynomial, A, by blood concentration c_b. The solid line shows the corresponding analytical derivative.

The zeroth-order coefficient of the polynomial and the skin absorption without melanin are, as expected, very close to each other. Correspondingly, the first-order coefficient and the analytical derivative are similar when the wavelength, $\lambda > 550$ nm. The numerical estimate if noisy, making the root-mean-square error-percentage (RMSEP) difference as large as 14%. For wavelengths at <550 nm, the behavior deviates from the Beer–Lambert law. The assumption of constant pathlength does not hold any longer because the absorption of melanin becomes very strong. The values of the second-order coefficient also seem to deviate from zero at wavelengths shorter than 550 or even 600 nm. The simple model shown in Eq. (6) seems work better at longer wavelengths.

3.2 *Absorption Versus Blood Concentration*

The simulation results for Eq. (5) and the comparison to Eq. (11) are shown in Fig. 6. The constant term and the skin absorption without blood are significantly different at short wavelengths. This is because in addition to the linear term p_d, the derivative also contains the nonlinear blood effect, $\mu_{a,b}p'_d$, and the cross-talk between skin baseline, $\mu_{a,d}p'_d$. The numerical and analytical first-order derivatives are again similar (<550 nm). The explanation for larger differences in the range 450–500 nm is the absorption of bilirubin. Bilirubin was assumed to be solved in blood in MCML simulation but not in the diffusion model. Therefore, the derivative of MCML data contains also the absorption of bilirubin, but the diffusion model does not. This difference did not seem to significantly disturb the prediction of blood and melanin concentrations.

3.3 *Comparison to Monte Carlo Simulation*

The accuracy of the prediction of the chromophore concentrations is assessed by means of the random MCML simulation data set, shown in Table 1. The results are displayed in Fig. 7. The accuracy of the prediction is measured as the RMSEP

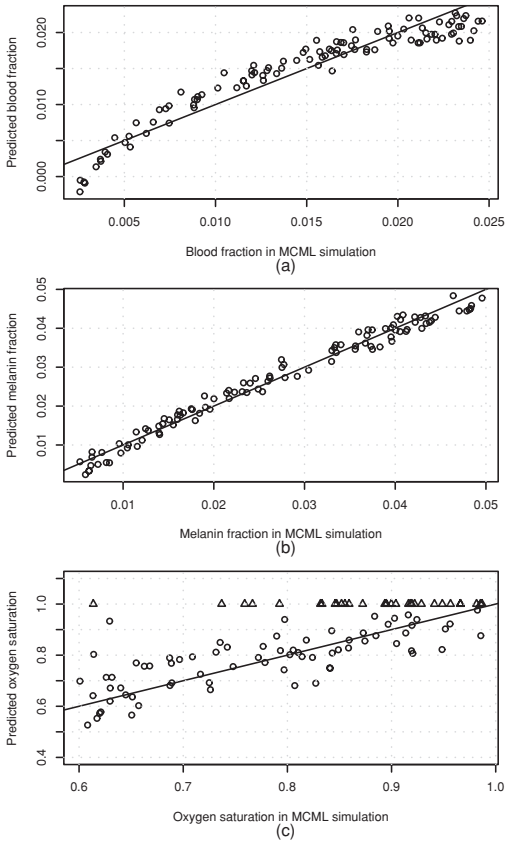

Fig. 7 Prediction of the chromophore concentrations of the MCML simulation using dMBLL and following wavelengths: $\lambda \in \{505, 530, 595, 625, 850\}$ nm. (a) Predicted blood fraction against blood fraction used in the MCML simulation. The prediction error is RMSEP=15% and the correlation between predicted and given values, r=0.94. (b) Predicted fraction of melanin against the melanin fraction used in MCML simulation. The prediction error RMSEP=7% and correlation r=0.99. (c) Predicted oxygen-saturation levels against saturation levels in the MCML simulation. RMSEP=10%, r=0.73.

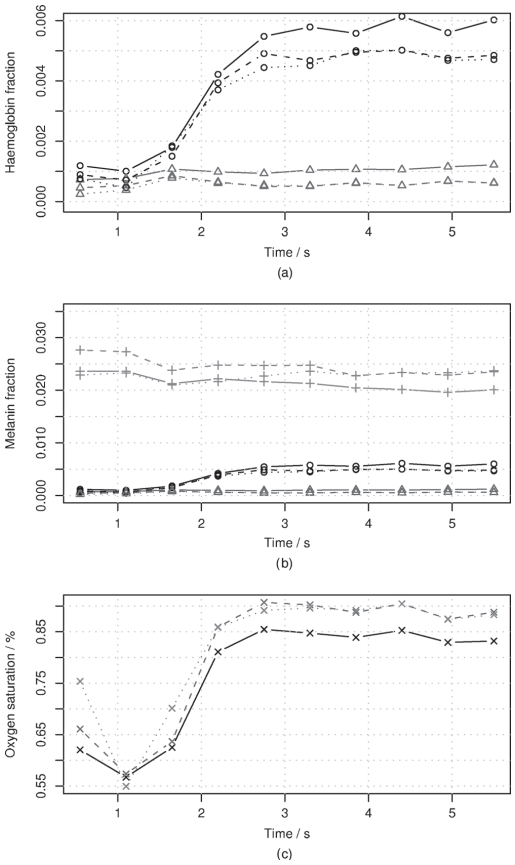

Fig. 8 Predictions of the chromophore concentrations of the Allen's test data set. Solid lines are predictions made by fitting the diffusion model to the full spectra. Dashed lines are obtained by fitting the diffusion model to selected five wavelengths, $\lambda \in \{505, 530, 595, 625, 850\}$ nm. The predictions shown in the dotted lines are obtained by fitting the dMBLL model to the dif ference of the spectra. The reference spectrum is the one measured at time $T = 4.4$ s. (a) Fraction of oxyhemoglobin (o) in upper curve and the fraction of deoxyhemoglobin (Δ) in lower curve, (b) Predicted fraction of melanin ($+$) in skin, and (c) Predicted oxygen saturation levels.

error and Pearson correlation coefficient between the predicted and given values. The prediction of the melanin content is the most accurate. Blood-prediction performance is slightly weaker than prediction for melanin because the relationship between the blood concentration and absorption is curved. The prediction of oxygen saturation is the weakest. Often the concentration of deoxyhemoglobin is very low, and even small absolute errors cause large relative errors. Sometimes even slightly negative values were observed. If negative concentration was observed, then it was saturated to zero. The samples shown as triangles are these kinds of fixed predictions.

Table 2 The Speeds of different implementations.

Method	Number of wavelengths	Execution time/spectrum	Time for 1 megapixel
MCML	285	25 min	NA
MCML	5	26 s	NA
Diffusion	285	1.1 s	12 days
Diffusion	5	0.53 s	6 days
dMBLL	5	1.2 ms	20 min

3.4 *Allen's Test Data*

The algorithm was applied to the experimental Allen's test data to study its performance for measured data. The results are shown in Fig. 8. The prediction of each chromophore was done with three different methods. First by fitting the skin model to the spectra by optimizing the chromophore concentrations with LMA (solid line). Then the same method was repeated, but now only five selected wavelengths were used (dashed lines). The third method is to use the analytical derivative and Eq. (17) to solve the linearized skin model around and operating point. The spectrum measured at time $T = 4.4$ s was used as an operating point.

3.5 *Execution Speed*

To evaluate the speed benefit gained by using a closed-form dMBLL solution, the predictions done above were benchmarked. The diffusion model and the dMBLL implementations were programmed with a statistical software package, called R. The MCML program was programmed with C. The predictions were run in a normal desktop PC. The processor of the PC was Intel®Core 2 CPU 6600 using a 2.40-GHz clock frequency. We also estimated how long it would take to process every pixel in a 1-megapixel image. The results of the benchmarks are shown in Table 2.

4 Discussion

The absolute blood concentration in dermis is perhaps not a clinically significant parameter because it varies all the time. The local and global blood circulation regulation change the blood perfusion in skin due to body and ambient temperature changes, due to physical exercise and the activity of metabolism, and for many other reasons not directly related to skin. Therefore, we have used the difference of the absorption between the normal skin and a skin disorder in measuring the severity of the disorder. The method developed here, represented by Eq. (17) can be used for finding the corresponding difference in chromophore concentrations behind the change of absorption. However, the absolute concentrations in the reference area are also needed because the derivative of absorption of dermis [shown in Eq. (10)] depends on the absolute concentration.

The fitting of the diffusion model to the average spectra of normal skin using LMA is a suitable method for determining

the normal operating point, around which the skin absorption can be linearized. The proposed method forms a simple relationship between the chromophore concentrations and the absorption. Many similar methods are based on heuristics of the shape of the spectral curves. Our method is based on solving a simple matrix equation where the transformation matrix is calculated from the analytical derivatives of the diffusion model. The method can be easily adapted to any set of chromophores and arbitrary wavelengths. The transformation matrix is optimized case by case. The numerical derivative of the MCML model could be used as well, but it is much slower to compute. The proposed model is accurate near the operating point, but the error increases when the difference in chromophore concentration becomes larger. The accuracy of the measurement may be further increased by using several reference points, in case the difference of concentrations is abnormally high.

The method can adapt to different wavelengths, but the accuracy is different in different wavelengths. The five wavelengths used in this paper form one good subset of wavelengths, because the accuracy is sufficient and they can all be produced using commonly available light-emitting diodes. Therefore, a spectral imaging system for chromophore mapping can be easily constructed. The accuracy may be still improved by optimizing the wavelengths. The proposed model should not be used for wavelengths of <550 nm because the model of epidermis differs significantly from MCML simulation. More research is needed to correct this problem in the future.

Here, the model also takes into account the specular reflections from the surface of the skin. In practice, the specular reflection can vary between skin locations, causing additional error. These reflections can be removed from the image by placing a polarizing filter in front of the light source and placing the second filter orthogonally in front of the camera lens, as described in Ref. 25 (Chap. 7). In this way, specular reflections and single scattered photons are filtered away. The polarization of the multiple scattered photons is lost, and therefore, part of them will pass through a second filter into the camera. When using these cross-polarizing filters, special attention must be paid to calibration, because the typical white references may reflect light mainly retaining the polarization. Therefore, the camera may measure even higher reflectance for red and NIR from skin than from the white reference.

The execution speeds of the optimization methods are unsuitably slow to the chromophore mapping purposes at the resolutions of contemporary cameras. The LMS algorithm is fast enough, but then the system needs to be linearized. When the system is linearized around a proper operating point, case by case, the linearizion does not cause too much error.

The proposed method for compensating the edge losses of the integrating sphere works for the optical properties used in the MCML simulation. However, the method is not validated for optical scattering and absorption coefficients, which differ significantly from those of normal skin. The simulations cover only one probe geometry, where light is illuminated through a collimated beam, which radius $r_b = 0.15$ cm, and the aperture radius of the integrating sphere was $r_a = 0.5$ cm. More studies are needed to find out if it is enough to only optimize the model parameters E_L and k or change the whole model, when the probe geometry changes.

5 Conclusion

In this research, a method is proposed to build a linear model, based on the differential Beer–Lambert law to efficiently map the chromophore concentrations in the spectral image of human skin. The proposed algorithm calculates an optimal linear model around an operating point, taking into account the spectra of the selected wavelengths, the concentrations of these chromophores in the selected operating point, and the available wavelengths. The system is validated against a data set created with a MCML simulation and a spectrometer measurement during the Allen's test, which modulates the blood fraction in skin.

The accuracy of the measurement is good enough for many purposes. The RMSEP in predicting the blood and melanin fraction was correspondingly 15 and 7%, and the Pearson correlation coefficients were $r = 0.94$ and $r = 0.99$. The prediction of the oxygen saturation is more error prone because the concentration of the deoxygenated hemoglobin is small. Therefore, the prediction of the oxygen-saturation levels is more difficult and the Pearson correlation between given and predicted values is $r = 0.73$. The error percentage is still low: RMSEP = 10% because the oxygen saturation levels were only predicted in the range of Os $\in$ [0.6, 1.0], and therefore, the errors are small compared to the actual value.

The proposed method is orders of magnitude faster than the methods based on optimization during prediction. Therefore the rendering of high-resolution spectral images is also possible.

Acknowledgments

The authors wish to thank an anonymous proofreaders of Journal of Biomedical optics. The received comments were very constructed and helped to further improve the article.

References

1. I. Konishi, Y. Ito, N. Sakauchi, M. Kobayashi, and Y. Tsunazawa, "A new optical imager for hemoglobin distribution in human skin," *Opt. Rev.* **10**, 592–595 (2003).
2. D. Jakovels and J. Spigulis, "2-D mapping of skin chromophores in the spectral range 500–700 nm," *J. Biophoton.* **3**, 125–129 (2010).
3. T. Yamamoto, H. Takiwaki, S. Arase, and H. Ohshima, "Derivation and clinical application of special imaging by means of digital cameras and ImageJ freeware for quantification of erythema and pigmentation," *Skin Res. Technol.* **14**, 26–34 (2008).
4. I. S. Kaartinen, P. O. Valisuo, J. T. Alander, and H. O. Kuokka-nen, "Objective scar assessment-a new method using standardized digital imaging and spectral modelling," *Burns* **37**(1), 74–81 February 2011.
5. M. Kobayashi, Y. Ito, N. Sakauchi, I. Oda, I. Konishi, and Y. Tsunazawa, "Analysis of nonlinear relation for skin hemoglobin imaging," *Opt. Express* **9**, 802–812 (2001).
6. P. Clarys, K. Alewaeters, R. Lambrecht, and A. O. Barel, "Skin color measurements: comparison between three instruments: the Chromameter®, the DermaSpectrometer® and the Mexameter®," *Skin Res. Technol.* **6**, 230–238 (2000).
7. L. E. Dolotov, Y. P. Sinichkin, V. V. Tuchin, S. R. Utz, G. B. Altshuler, and I. V. Yaroslavsky, "Design and evaluation of a novel portable erythema-melanin-meter," *Lasers Surg. Med.* **34**, 127–135 (2004).
8. M. Moncrieff, S. Cotton, E. Claridge, and P. Hall, "Spectrophotometric intracutaneous analysis: a new technique for imaging pigmented skin lesions," *Br. J. Dermatol.* **146**, 448–457 (2002).
9. G. E. Nilsson, H. Zhai, H. P. Chan, S. Farahmand, and H. I. Maibach, "Cutaneous bioengineering instrumentation standardization: the tissue viability imager," *Skin Res. Technol.* **15**, 6–13 (2009).

10. G. V. G. Baranoski and A. Krishnaswamy, "Light interaction with human skin: from believable images to predictable models," in *Siggraph Asia 08*, ACM, New York, pp. 1–80 (2008).
11. T. Igarashi, K. Nishino, and S. Nayar, "The appearance of human skin: A survey," *Found. Trends Comput. Graphics Vis.* **3**, 1–95 (2007).
12. S. A. Prahl, M. Keijzer, S. L. Jacques, and A. J. Welch, "A Monte Carlo model of light propagation in tissue," *Dosim. Laser Radiat. Med. Biol.* **IS 5**, 102–111 (1989).
13. L. Wang, S. L. Jacques, and L. Zheng, "MCML—Monte Carlo modeling of light transport in multi-layered tissues," *Comput. Methods Prog. Biomed.* **47**, 131–146 (1995).
14. L. H. Wang, S. L. Jacques, and L. Q. Zheng, "CONV—Convolution for responses to a finite diameter photon beam incident on multi-layered tissues," *Comput. Methods Prog. Biomed.* **54**, 141–150 (1997).
15. J. L. Reuss, "Multilayer modeling of reflectance pulse oximetry," *IEEE Trans. Biomed. Eng.* **52**, 153–159 (February 2005).
16. E. Claridge, S. Cotton, P. Hall, and M. Moncrieff, "From colour to tissue histology: physics based interpretation of images of pigmented skin lesions," in *Medical Image Computing and Computer-Assisted Intervention—MICCAI 2002*, Lecture Notes in Computer Science, Vol. 2488, Takeyoshi Dohi and Ron Kikinis, Eds., pp. 730–738, Springer Berlin (2002).
17. E. Claridge and S. Preece, "An inverse method for the recovery of tissue parameters from colour images," in *Processing in Medical Imaging*, Vol. 2732, pp. 306–317, Springer, Ambleside, UK (2003).
18. S. J. Preece and E. Claridge, "Spectral filter optimization for the recovery of parameters which describe human skin," *IEEE Trans. Pattern Anal. Mach. Intell.* **26**, 913–922 (July 2004).
19. M. Shimada, Y. Yamada, M. Itoh, and T. Yatagai, "Melanin and blood concentration in human skin studied by multiple regression analysis: experiments," *Phy. Med. Biol.* **46**, 2385–2395 (2001).
20. P. Valisuo, T. Mantere, and J. Alander, "Solving optical skin simulation model parameters using genetic algorithm," in *Proc. of 2nd Int. Conf. on BioMedical Engineering and Informatics*, pp. 376–380 (2009).
21. M. J. C. van Gemert, S. L. Jacques, H. J. C. M. Sterenborg, and W. M. Star, "Skin optics," *IEEE Trans. Biomed. Eng.* **36**, 1146–1154 (December 1989).
22. P. Välisuo and J. Alander, "The effect of the shape and location of the light source in diffuse reflectance measurements," in *Proc. of 21st IEEE Int. Symp. on Computer-Based Medical Systems*, IEEE Computer Society, pp. 81–86 (2008).
23. M. S. Patterson, B. Chance, and B. C. Wilson, "Time resolved reflectance and transmittance for the noninvasive measurement of tissue optical properties," *Appl. Opt.* **28**, 2331–2336 (1989).
24. T. J. Farrell, M. S. Patterson, and B. Wilson, "A diffusion theory model of spatially resolved, steady-state diffuse reflectance for the noninvasive determination of tissue optical properties *in vivo*," *Med. Phy.* **19**, 879–888 (1992).
25. V. V. Tuchin, *Tissue Optics: Light Scattering Methods and Instruments for Medical Diagnosis*, SPIE Press, Bellingham, WA (2007).
26. M. Shimada, Y. Masuda, Y. Yamada, M. Itoh, M. Takahashi, and T. Yatagai, "Explanation of human skin color by multiple linear regression analysis based on the modified Lambert–Beer law," *Opt. Rev.* **7**, 348–352 (2000).
27. L. Kocsis, P. Herman, and A. Eke, "The modified Beer–Lambert law revisited," *Phy. Med. Biol.* **51**, N91–N98 (2006).
28. M. G. Sowa, A. Matas, B. J. Schattka, and H. H. Mantsch, "Spectroscopic assessment of cutaneous hemodynamics in the presence of high epidermal melanin concentration," *Clin. Chim. Acta* **317**, 203–212 (2002).
29. G. N. Stamatas, B. Z. Zmudzka, N. Kollias, and J. Z. Beer, "*In vivo* measurement of skin erythema and pigmentation: new means of implementation of diffuse reflectance spec-troscopy with a commercial instrument," *Br. J. Dermatol.* **159**, 683–690 (2008).
30. J. R. Mourant, T. M. Johnson, G. Los, and I. J. Bigio, "Non-invasive measurement of chemotherapy drug concentrations in tissue: preliminary demonstrations of *in vivo* measurements," *Phys. Med. Biol.* **44**, 1397–1418 (1999).
31. A. Amelink and H. J. C. M. Sterenborg, "Measurement of the local optical properties of turbid media by differential path-length spectroscopy," *Appl. Opt.* **43**, 3048–3054 (2004).
32. I. S. Kaartinen, P. O. Valisuo, V. Bochko, J. T. Alander, and H. O. Kuokkanen, "How to assess scar hypertrophy? A comparison of subjective scales and spectrocutometry — a new objective method," *Wound Repair Regen.* (in press).
33. V. V. Tuchin, S. R. Utz, and I. V. Yaroslavsky, "Tissue optics, light distribution, and spectroscopy," *Opt. Eng.* **33**, 3178–3188 (October 1994).
34. P. Valisuo, I. Kaartinen, H. Kuokkanen, and J. Alander, "The colour of blood in skin: a comparison of Allen's test and photonics simulations," *Skin Res. Technol.* **16**, 390–396 (November 2010).
35. S. L. Jacques and D. J. McAuliffe, "The melanosome: threshold temperature for explosive vaporization and internal absorption coefficient during pulsed laser irradiation," *Photochem. Photobiol.* **53**, 769–775 (1991).
36. S. L. Jacques, "Origins of tissue optical properties in the UVA, visible, and NIR regions," *Adv. Opt. Imaging Photon Migrat.* **2**, 364–369 (1996).
37. I. S. Saidi, "Transcutaneous optical measurement of hyperbilirubinemia in neonates," PhD Thesis, Rice University, Houston (1992).
38. J. O. Ramsay and B. W. Silverman, "Functional data analysis," *Stat. Comput.* **8**, 401–403 (1998).